ERCOFTAC

Bulletin

September 2021

128

ERCOFTAC is a leading European association of research, education and industry groups in the technology of flow, turbulence and combustion. The main objectives of *ERCOFTAC* are: To promote joint efforts of European research institutes and industries with the aim of **exchanging technical and scientific information**; to promote **Pilot Centres** for collaboration, stimulation and application of research across Europe; to stimulate, through the creation of **Special Interest Groups**, wellcoordinated European-wide research efforts on specific topics; to stimulate the creation of advanced training activities; and to be influential on funding agencies, governments, the European Commission and the European Parliament.

www.ercoftac.org

Table Of Contents

Respiratory Airflows and Aerosol Deposition 4
S. C. Kassinos and J. Sznitman

Analysis of Drug Particle Deposition in Swirl-Type Dry Powder Inhalers 5
M. Sommerfeld

How Flow Rate, Head Position, and Inhaler Orientation Affect the Drug Deposition in the Mouth-Throat 14
F.S. Stylianou, P.G. Koullapis, B. Olsson and S.C. Kassinos

The Fate of Inhaled Hygroscopic Particles Inside the Human Airways 28
F.S. Stylianou, P.G. Koullapis, and S.C. Kassinos

Experimental and Computational Modelling of Aerosol Transport Using the BUT Benchmark Human Lung Model 36
F. Lizal, J. Elcner, M. Belka, J. Jedelsky, and M. Jicha

Variations of Flow Patterns in the Upper Bronchial Tree During the Breathing Cycle 44
K. Bauer, R. Schwarze and T. Janke

Submissions

ERCOFTAC Bulletin
Department of Thermal Machinery
Częstochowa University of Technology
Al. Armii Krajowej 21
42-201 Częstochowa
Poland
Tel: +48 343 250 507
Fax: +48 343 250 507
Email:ercoftac@imc.pcz.czest.pl

Hosted, Printed & Distributed By

Częstochowa University of Technology

ISSN: 2518-0991

Next *ERCOFTAC* Events

ERCOFTAC Autumn Festival
7^{th} of October, 2021
Rome, Italy

ERCOFTAC Committee Meetings
8^{th} of October, 2021
Rome, Italy

The ERCOFTAC Best Practice Guidelines for Industrial Computational Fluid Dynamics

The Best Practice Guidelines (BPG) were commissioned by ERCOFTAC following an extensive consultation with European industry which revealed an urgent demand for such a document. The first edition was completed in January 2000 and constitutes generic advice on how to carry out quality CFD calculations. The BPG therefore address mesh design; construction of numerical boundary conditions where problem data is uncertain; mesh and model sensitivity checks; distinction between numerical and turbulence model inadequacy; preliminary information regarding the limitations of turbulence models etc. The aim is to encourage a common best practice by virtue of which separate analyses of the same problem, using the same model physics, should produce consistent results. Input and advice was sought from a wide cross-section of CFD specialists, eminent academics, end-users and, (particularly important) the leading commercial code vendors established in Europe. Thus, the final document can be considered to represent the consensus view of the European CFD community.

Inevitably, the Guidelines cannot cover every aspect of CFD in detail. They are intended to offer roughly those 20% of the most important general rules of advice that cover roughly 80% of the problems likely to be encountered. As such, they constitute essential information for the novice user and provide a basis for quality management and regulation of safety submissions which rely on CFD. Experience has also shown that they can often provide useful advice for the more experienced user. The technical content is limited to single-phase, compressible and incompressible, steady and unsteady, turbulent and laminar flow with and without heat transfer. Versions which are customised to other aspects of CFD (the remaining 20% of problems) are planned for the future.

The seven principle chapters of the document address numerical, convergence and round-off errors; turbulence modelling; application uncertainties; user errors; code errors; validation and sensitivity tests for CFD models and finally examples of the BPG applied in practice. In the first six of these, each of the different sources of error and uncertainty are examined and discussed, including references to important books, articles and reviews. Following the discussion sections, short simple bullet-point statements of advice are listed which provide clear guidance and are easily understandable without elaborate mathematics. As an illustrative example, an extract dealing with the use of turbulent wall functions is given below:

- Check that the correct form of the wall function is being used to take into account the wall roughness. An equivalent roughness height and a modified multiplier in the law of the wall must be used.
- Check the upper limit on $y+$. In the case of moderate Reynolds number, where the boundary layer only extends to $y+$ of 300 to 500, there is no chance of accurately resolving the boundary layer if the first integration point is placed at a location with the value of $y+$ of 100.
- Check the lower limit of $y+$. In the commonly used applications of wall functions, the meshing should be arranged so that the values of $y+$ at all the wall-adjacent integration points is only slightly above the recommended lower limit given by the code developers, typically between 20 and 30 (the form usually assumed for the wall functions is not valid much below these values). This procedure offers the best chances to resolve the turbulent portion of the boundary layer. It should be noted that this criterion is impossible to satisfy close to separation or reattachment zones unless $y+$ is based upon $y*$.
- Exercise care when calculating the flow using different schemes or different codes with wall functions on the same mesh. Cell centred schemes have their integration points at different locations in a mesh cell than cell vertex schemes. Thus the $y+$ value associated with a wall-adjacent cell differs according to which scheme is being used on the mesh.
- Check the resolution of the boundary layer. If boundary layer effects are important, it is recommended that the resolution of the boundary layer is checked after the computation. This can be achieved by a plot of the ratio between the turbulent to the molecular viscosity, which is high inside the boundary layer. Adequate boundary layer resolution requires at least 8-10 points in the layer.

All such statements of advice are gathered together at the end of the document to provide a 'Best Practice Checklist'. The examples chapter provides detailed expositions of eight test cases each one calculated by a code vendor (viz FLUENT, AEA Technology, Computational Dynamics, NUMECA) or code developer (viz Electricité de France, CEA, British Energy) and each of which highlights one or more specific points of advice arising in the BPG. These test cases range from natural convection in a cavity through to flow in a low speed centrifugal compressor and in an internal combustion engine valve.

Copies of the Best Practice Guidelines can be acquired from:

ERCOFTAC (CADO)
PO Box 1212
Bushey, WD23 9HT
United Kingdom
Tel: +44 208 117 6170
Email: admin@cado-ercoftac.org

The price per copy (not including postage) is:

ERCOFTAC members	
First copy	*Free*
Subsequent copies	75 Euros
Students	75 Euros
Non-ERCOFTAC academics	140 Euros
Non-ERCOFTAC industrial	230 Euros
EU/Non EU postage fee	10/17 Euros

BPG for CFD in Turbulent Combustion

ERCOFTAC
Best Practice Guidelines for CFD of Turbulent Combustion

Editors: Profs. Luc Vervisch, & Dirk Roekaerts

The aim of this Best Practice Guide (BPG) is to provide guidelines to CFD users in a wide range of application areas where combustion is an essential process. Since the first edition published in 2015, the interest in numerical modeling of the emission of particulate material formed in flames is continuously growing. For this reason, this second edition includes an new Chapter on the modeling of sooting flames.

The overall structure of the BPG is as follows:
Chapters 1-3 summarize key issues in turbulent combustion model formulation. Chapter 4 is addressing the validation of modelling using available experimental databases. In the new Chapter 5 the fundamentals driving the formation and the evolution (nucleation, growth, agglomeration, oxidation) of flowing non-inertial particles are discussed, before presenting best practices for major soot modeling approaches in CFD of turbulent flames. Then, two application areas are elaborated in separate chapters: Chapter 6 on Internal Combustion Engines, and Chapter 7 on Gas Turbines. Best practice guidelines by the nature of technology development are always temporary. New insights and approaches will take over after some time. Therefore this BPG ends with a Chapter 8 on Emerging Methods, providing a preview of approaches so far only useful for simulating canonical configurations or requiring further developments.

A comprehensive CFD approach to turbulent combustion modelling relies on appropriate submodels for flow turbulence, chemistry and radiation, and their interactions. In the framework of this BPG, knowledge of turbulent flow modeling is a pre-requisite and only briefly explained. Instead the discussion on models is divided in three parts: turbulence-chemistry interaction (Chapter 1), chemistry (Chapter 2) and radiative heat transfer (Chapter 3). Many of the models introduced in the first three chapters will reappear in the discussion in Chapters 4 to 6 and comments on challenges, advantages and disadvantages are formulated in all chapters. Those looking for immediate advices to tackle a specific application may want to proceed immediately to the application chapters (IC engines in Chapter 5 and Gas Turbines in Chapter 6) and return to the basic chapters when necessary. But everyone not finding in these chapters an immediate answer to the basic question: What is the best model for my specific application? should certainly spend some time on Chapter 4, because it addresses the mandatory preliminary steps that have to be considered to validate a simulation involving any sort of turbulent flames.

Table of Content
1-Introduction to turbulent combustion modelling
2-Combustion Chemistry
3-Thermal Radiation
4-RANS and LES validation
5-Sooting flames
6-Internal Combustion Engine
7-Gas-Turbines
8-Emerging Methods

To order please visit:

`https://www.ercoftac.org/publications/ercoftac_best_practice_guidelines/cfd_of_turbulent_combustion/`

Or from:
ERCOFTAC (CADO)
PO Box 1212
Bushey, WD23 9HT
United Kingdom
Tel: +44 208 117 6170

Email: `admin@cado-ercoftac.org`

The price per copy (not including postage) is:
ERCOFTAC members
First copy Free
Subsequent copies 75 Euros
Students 75 Euros
Non-ERCOFTAC academics, 140 Euros
Non-ERCOFTAC industrial, 230 Euros
EU / Non EU postage fee 10/ 17 Euros

Respiratory Airflows and Aerosol Deposition

S. C. Kassinos[1], J. Sznitman[2]

[1] *Computational Sciences Laboratory, Department of Mechanical and Manufacturing Engineering, University of Cyprus*
[2] *Department of Biomedical Engineering, Technion-Israel Institute of Technology, Haifa 3200003, Israel*

Chronic lung disease causes significant human suffering and ranks among the leading causes of premature death worldwide. Modern inhalation therapy was first put on a solid scientific foothold in the middle of the last century and has since evolved to a mainstay of modern respiratory medicine. Despite significant progress, targeted delivery of inhaled drugs, where specific lung areas can be reached with precision, remains largely an unattained goal. In this regard, two important obstacles are the sheer complexity of the respiratory system and the fact that the bulk of the lungs remains largely inaccessible to high-resolution imaging that would allow quantification of regional deposition *in vivo*.

Over the last decade, Computational Fluid Particle Dynamics (CPFD) of respiratory airflows and aerosol deposition have evolved into a mature filed in biomedical engineering, propelled by improvements in computational methods and increases in computational power. CFPD has the potential to fill the gap left by *in vivo* methods for quantifying drug delivery in the lungs. The tremendous potential of the application of CFPD in the area of respiratory biomechanics and medicine is reflected in an exponential growth in the number research articles that are published annually on the topic. As is the case with other areas of science and engineering experiencing rapid proliferation of publications, scrutiny of recent literature reveals significant variability in the rigor and quality of published articles presenting CPFD applications to respiratory biomechanics and drug delivery. This realization has prompted a number of research teams across Europe to join efforts, under the auspices of COST Action 1404 (*SimInhale*), towards establishing a series of benchmark cases and best practice guidelines, that are now hosted by ERCOFTAC under the Knowledge Base Wiki. These cases consist of combined experimental and computational investigations of respiratory flow and aerosol deposition, designed to elucidate potential pitfalls in the application CPFD and to quantify variability in computational results. Much of this effort is now continued by the Special Interest Group on *Respiratory Aerosols: Therapeutic Interventions and Environmental Exposure* (SIG48).

The current thematic issue of the ERCOFTAC Bulletin provides examples of the application of CFPD methods to different aspects of inhaled drug delivery. The articles of the issue are organized in a sequence that reflects the typical path of a drug bolus. Thus, in the opening article, M. Sommefeld considers the aerolization of the drug in a Dry Powder Inhaler (DPI) and uses a RANS-based Eulerian/Lagrangian approach and several different deposition models to examine the adhesion of fine drug particles (API) on the device walls.

A significant fraction of the dose released by a DPI is typically deposited in the extrathoracic airways (oral and larygnpoharengeal cavities, trachea) where it is wasted and can even have undesirable effects. In a sequence of two papers, Stylianou et al. use Large Eddy Simulations in an Eulerian/Lagrangian formulation to examine factors that control extrathoracic deposition. In the first paper, they examine the effect of head position and of inhaler inclination on the amount of aerosol deposited in the extrathoracic airways. In the second paper, they use Large Eddy Simulations (LES) of turbulent airflow with particle transport including heat transfer, water vapor transfer, and aerosol hygroscopic growth effects to investigate the proposed use of hygroscopic excipients as a strategy for minimizing extrathoracic drug losses and achieving targeted delivery.

While most numerical/experimental works to date have considered deposition during only the inhalation phase, there is currently increasing emphasis on understanding deposition over the entire respiratory cycle, using realistic respiratory profiles. In this regard, Lizal et al. provide an overview of recent recent experimental and numerical results obtained using the Brno University of Technology (BUT) realistic human lung model, i.e. the same anatomical model that was used in the SimInhale Benchmark cases published on the ERCOFTAC Knowledge Base Wiki. They report results for both the flowfield and regional aerosol deposition. In the same direction, Bauer et al. immerse essentially the same anatomical geometry in a tank filled with a mixture of water and glycerin and perform Particle Image Velocimetry (PIV) flow measurements for complete respiratory cycles at different inhalation rates.

The Special Interest Group on *Respiratory Aerosols: Therapeutic Interventions and Environmental Exposure* (SIG48) was formed in 2019, shortly before the onset of the covid-19 pandemic. While the emergence of the pandemic has been challenging for the development of the newly-formed special interest group, it has also served to bring to focus, and perhaps to wider realization, the need to deepen our understanding of respiratory aerosol generation, transport, and deposition and to improve our computational modeling tools. This thematic issue of the Bulletin provides a glimpse into the current activities of SIG48, which we hope will be further expanded in the coming years in an effort to contribute to the worldwide drive towards establishing CFPD methods as the third major pillar for quantifying respiratory drug delivery, along with *in vivo* and *in vitro* methods.

Analysis of Drug Particle Deposition in Swirl-Type Dry Powder Inhalers

M. Sommerfeld

Multiphase Flow Systems, Institute of Process Engineering, Otto-von-Guericke-University Magdeburg, Hoher Weg 7b, D-06130 Halle (Saale) Germany

martin.sommerfeld@ovgu.de

Abstract

Based on numerical simulations by the Euler/Lagrange approach in combination with the RNG-k-ϵturbulence model flow field and particle transport through inhaler devices are studied. Since one major problem in inhaler performance and drug powder release is the deposition on the inhaler walls this issue is analysed in more detail. For computing fine particle motion through the stationary flow field all relevant particle forces and turbulent dispersion are considered. The possible deposition of fine particles on the inhaler walls is determined through a critical impact velocity approach which accounts for the elastic-plastic properties of wall and particle materials with adhesion. The performance of different deposition models was first analysed. The overall deposition of particles in the entire inhaler is determined in dependence of particle size, (stationary) flow rate, particle release location and type of inhaler. Additionally, the spatial distribution of the deposits is determined for allowing inhaler optimisation.

1 Introduction

Dry powder inhalers (DPI) are increasingly used to administer drugs in the form of fine powders through the airways. These drugs are also called API (active pharmaceutical ingredient). Since such fine powders need to be smaller than about 5 μm for lung inhalation, they are expectedly very cohesive and difficult to handle and disperse in an inhaler device. Therefore, two kinds of formulations are commonly in use. Most widespread is the blending of larger carrier particles with the fine drugs (called cluster), however, also agglomerated drug powder may be delivered to the inhaler using blisters. The main task of the inhaler is the detachment of the drug from the carrier or the destruction (aerosolization) of the agglomerates. Due to the strong adhesion forces between such small powders, both formulations require remarkable stresses for destruction. These may be realised by flow stresses produced through the breathing-induced air flow within the inhaler (Telko and Hickey 2005) or by frequent wall impacts (Sommerfeld et al. 2019). Unfortunately, the efficiency of dry powder inhalers is very low and only 20 to 40 % of the fine particle dose (API) loaded into the inhaler is delivered to the lung.

The reason for such a low efficiency is until today not fully clarified. Because of these open issues in DPI performance, the complex and highly turbulent, mostly swirling flow field within inhalers and the difficult real-scale experimental analysis, computational fluid dynamics (CFD) is applied for more than one decade in order to analyse DPI related specific phenomena. Some of this work has been reviewed by Wong et al. (2012), Ruzycki et al. (2013) and Cui and Sommerfeld (2018). A detailed review, specifically related to particle phase modelling, was recently provided by Sommerfeld et al. (2019). The need for multiscale modelling approaches for capturing all particle-scale transport processes was clearly emphasised by Tong et al. (2015) and van Wachem et al. (2017).

Although LES (Large eddy simulations) is increasingly applied to complex inhaler flows, most of the simulations are still done on the basis of RANS (Reynold-averaged Navier-Stokes) equations in connection with an appropriate turbulence closure (e.g. RNG-k-ϵor k-ω-SST). Conceptually, LES requires fully unsteady simulations whereas RANS is mostly conducted in a steady-state mode for certain fixed flow rates through the inhaler. Therefore, LES requires much longer computational times.

Until now quite a number of studies were related to Lagrangian point-particle calculations of the motion of different kinds of particles through inhaler devices, such as: fine drug particle motion behaviour and the influence of mouthpiece length as well as grid structure (Coates et al. 2004); fine particle tracking and analysis of deposition in a Turbuhaler device (Milenkovic et al. 2013) and analysis of coarse carrier particle motion in a Lagrangian way analysing wall collision frequencies and the relevance of different forces, especially those originating from particle rotation (see Donovan et al. 2012, Sommerfeld and Schmalfuß 2016).

One unsolved issue in the operation of DPIs is the deposition of fine drug particles on the walls of the inhaler. This may happen during carrier particle wall collisions (Ariane et al. 2018; Cui and Sommerfeld 2019) but also during the transport of aerosolised API inside the inhaler. Such a deposition study for fine particles below 10 μm was conducted by Milenkovic et al. (2013) for a Turbuhaler using numerical simulations based on an Euler/Lagrange approach. Besides RANS (Reynolds-averaged Navier-Stokes) with the k-ω-SST and the RNG-k-ϵalso LES (large eddy simulations) were used to calculate the flow field (see Sommerfeld et al. 2019).

The present study concerns a detailed analysis of API deposition in two different inhaler devices. For that purpose, several deposition models are applied considering also the influence of wall and particle material in the adhesion models. The considered deposition models are based on the critical velocity approach resulting from an energy balance.

2 Numerical approach

In this study the Euler/Lagrange approach in combination with the RNG-k-ϵturbulence model is primarily applied for analysing fine particle transport and deposition locations in two types of dry powder inhalers, the well-known Cyclohaler (or Aerolizer) and the modular swirl-type inhaler developed at the University Kiel (Friebel 2010). A comparison of both inhalers regarding carrier particle motion was already presented previously (Sommerfeld et al. 2019).

In the present study only fine individual and spherical drug particles are considered. The motion of such fine drug particles (here below 10 μm) was performed on the basis of the Lagrangian point-particle approach considering drag and gravity, as well as the Brownian random force. The drag force was extended by applying the Cunningham correction in order to model the slip effect, which becomes relevant for very fine particles. Due to the small size of the particles, transverse lift forces due to shear and particle rotation may be neglected since they are of minor importance. Naturally, also the effect of turbulence on particle motion was accounted for using a single-step Langevin model (Sommerfeld et al. 2008). Collisions between particles as well as any modifications of the flow field by the particle phase (two-way coupling) or any wall deposits are not considered in the present study. All new implementations performed are realised in the open-source code OpenFOAM.

3 Deposition Model

In order to obtain particle deposition on rigid walls of confined flows, two criteria must be fulfilled. First the particle needs to be transported towards the wall through inertial effects, fluid dynamic forces as well as turbulence and Brownian motion. Second the particle needs to stick to the wall by the involved adhesion forces depending on particle and wall material. In the present study dry systems are considered so that only the van der Waals adhesion is relevant. Although particle charging may occur during the transport through the inhaler, the resulting adhesion force is neglected since the degree of particle charging is completely unknown.

Mostly Lagrangian models for deposition are relaying on a critical particle impact velocity below which deposition may occur. In the present case an elastic-plastic-adhesive oblique wall collision is considered. The required critical velocity is derived based on either an energy balance or a force or impulse balance (i.e. Newton‘s second law). The relevant energies in the particle-wall impact process are the kinetic energy of impact and rebound, a dissipated energy, mainly due to plastic deformation, a surface energy due to interface deformation and adhesion energy caused in dry systems by the van der Waals interaction for the impact and rebound phase. Deposition will of course only take place if the rebound energy becomes zero. For deriving the different energy contributions, the size of the contact area (i.e. radius and depth) is required, which may be derived by the Hertzian theory (Hertz 1882) or the JKR-model (Johnson et al. 1971). This deformation area of course depends on the material properties of particle and wall, such as Poisson ratio ν_i and Young's modulus E_i. Other relevant material properties are the Hamaker constant, the yield pressure and the interface energy. Consequently, a reliable modelling of drug particle deposition in inhaler devices requires actually all these parameters which are however mostly not available.

In literature a number of deposition models are presented based on different derivation concepts and considering also different processes during particle impact on a plane wall. In the present study three deposition models are considered delivering a critical impact velocity for deposition to occur.

First the energy-based model proposed by Hiller (1980) for fine particle deposition on single fibres (i.e. related to gas filtration) is considered. Here the impact kinetic energy of the particle, $E_{K1} = 1/2 m_P V_{Pn1}^2$ is compared with the adhesion energy (van der Waals energy), ΔE_A and the dissipated energy E_D which is determined with the maximum deformation depth.

$$E_{K1} \leq E_D + \Delta E_A \tag{1}$$

Note that for an oblique particle-wall impact V_{Pn1} is the wall normal velocity component. This yields finally the critical normal impact velocity for deposition on a plane wall as:

$$V_{crit} = \frac{\sqrt{1-k^2}}{\pi k^2 d_P z_0^2} \frac{H}{\sqrt{6 \rho_P p_y}} \tag{2}$$

The minimum contact distance is normally set to 0.4 nm (0.4×10^{-9} m) and k is the energetic restitution ratio $k^2 = (1 - E_D/E_{K1})$, H the Hamaker constant and p_y the yield pressure, all depending on the softest wall or particle material considered.

The deposition model of Brach and Dunn (1992) was developed for an oblique elastic-plastic wall impact of small particles. The maximum contact area radius is determined on the basis of the Hertzian contact theory. Setting the kinetic energy of the impact (normal component for oblique impact angles) equal to the adhesion energy including the stored elastic energy and the interface adhesion energy one obtains eventually:

$$V_{crit} = 0.835 \left(\frac{1+\eta^2}{k^2} \right)^{\frac{10}{7}} \left(\frac{1}{E^\star} \right)^{\frac{4}{7}} \left(\frac{1}{\rho_p} \right)^{\frac{6}{7}} \left(\frac{1}{R_p} \right)^{\frac{10}{7}} \tag{3}$$

In this equation is a kind of friction coefficient and termed as impulse ratio and is the energetic restitution ratio, is the particle material density and the particle radius. The material property parameter is defined in the most common way as:

$$E^\star = \left(\frac{1-\nu_S^2}{E_S} + \frac{1-\nu_P^2}{E_P} \right)^{-1} \tag{4}$$

where the properties of surface $i = S$ and particle $i = P$ are considered hrough the Young‘s modulus E_i and the Poisson ratio ν_i

Another deposition model frequently used in the literature (see e.g. Venturini 2010) is that of Thornton and Ning (1998) where the normal wall impact of elastic-plastic adhesive spheres was considered. Again, based on an energy balance, the critical velocity for deposition was derived considering the JKR-theory for obtaining the ra- dius of deformation (Johnson et al. 1971). For this situa- tion one obtains:

$$V_{crit} = 1.84 \left\{ \left(\frac{1}{E^\star} \right)^{1/3} \left(\frac{1}{\rho_P} \right)^{1/2} \left(\frac{\gamma^\star}{R_P} \right)^{5/6} \right\} \tag{5}$$

where $\gamma^\star = \sqrt{\gamma_P \gamma_S}$ is the interface energy composed of both the particle and surface energy.

Beyond the critical normal impact velocity, i.e. when particle rebound occurs, the fully three-dimensional

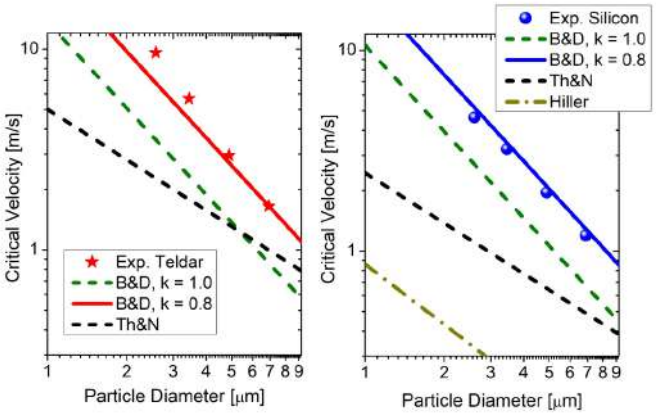

Figure 1: Critical velocity in dependence of particle diameter (ammonium fluorescein) for different wall materials (left: Teldar (polyvinyl-fluoride), right: Silicon), comparison of model predictions (B&D: Brach and Dunn (1992) k = 1.0, $\eta = 0$ and k = 0.8, $\eta = 0.1$; Th&N: Thornton and Ning (1998); Hiller (1980)) with experiments (Wall et al. 1990); for the Hiller (1980) model (only silicon) the following parameters were used: $H = 2.35 \cdot 10^{-19} J$; $p_y = 3.20 \cdot 10^7 Pa$; $k = 0.8$

hard-sphere wall collision model is solved without particle rotation (Sommerfeld and Huber 1999). Since the walls of an inhaler are supposed to be a very smooth plastic material and the particles are assumed to be perfect spheres, any wall roughness effects are neglected. Moreover, since the particles are small and have very low inertia, particle rotation and the change of rotation due to wall collisions may be neglected without large errors.

The dependence of the critical velocity on the material properties opens the possibility to study the influence of materials on the overall and local particle deposition.

For validating the different deposition models the experimental data of Wall et al. (1990) were considered, where mono-size ammonium fluorescein (NH_4 Cl) spheres (diameter between 2.6 and 6.9 μm) impinge on different surface materials. These materials were Silicon, molybdenum and Tedlar, all carefully prepared to yield smooth surfaces. The material properties used for the present model calculation for the particles and the wall materials Teldar and Silicon are summarised in Table 1. The model of Brach and Dunn (1992), in the following called B7&D, with k = 1.0 and $\eta = 0$ under-predicts the measured critical velocity (Figure 1). However, when including a restitution coefficient of k = 0.8 and a friction of $\eta = 0.1$ the agreement is almost perfect for different wall materials, both with respect to slope and magnitude. The model of Th&N (Thornton and Ning 1998) remarkably under-predicts the critical velocity in dependence of particle size and also the slope of the curve is different (Figure 1). Even when selecting a restitution ratio k = 0.8, the critical velocity obtained by the Hiller (1981) model is more than one order of magnitude smaller as the experimental values. Also, this model shows no strong sensitivity on the wall material, which is probably caused by the selection of the Hamaker constants.

4 Inhaler Geometry and Flow Field

The geometries of the two considered inhalers are shown in Figure 2 a) and b) consisting both of a capsule and

Table 1: Summary of particle and wall mechanical properties for the calculation of the critical velocity according to the measurements of Wall et al. (1990)

Material of Particles and Walls	Density [kg/m^3]	Young [GPa]	Poisson ratio [-]
NH_4 Cl Particles	1350	1.2	0.33
Teldar Wall	1460	2.1	0.33
Silicon Wall	2330	182.0	0.30

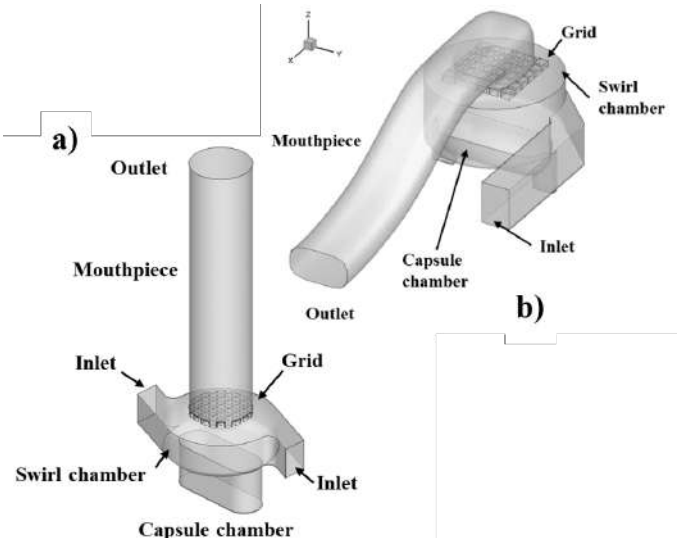

Figure 2: Geometry of Cyclohaler (a) and Unihaler (b) with capsule chamber, swirl chamber, grid and mouthpiece

a swirl chamber, a grid as a kind of flow straightener and a mouth piece. A remarkable difference between the inhalers is not only the general shape, but also the Cyclo- haler has two inlets whereas the Unihaler has only a sin- gle inlet channel which of course yields for the same flow rate higher velocities and induces a strongly asymmetric flow in the swirl chamber and through the grid. This real- scale geometry was discretised by an unstructured mesh with 1.44 million computational cells for both inhalers. For inducing the flow through the inhalers the considered flow rate is specified at the outlet of the mouthpiece and zero-gradient conditions are applied at the inlet. In phar- macy a comparison of different inhaler types is usually done for a pressure drop of about 4 kPa. The Unihaler has expectedly much higher pressure drop wherefore a com- parison of both devices was done considering different flow rates; i.e. 90 l/min for the Cyclohaler and 60 l/min for the Unihaler, yielding roughly the same pressure drop.

In both inhaler types a very strong high-velocity swirling flow develops (Figure 3 a) and b)). Due to the single inlet of the Unihaler the swirl velocity is higher, even the flow rate is lower. The one-sided inlet also causes a quite uneven flow through the grid. Within the cap- sule chamber a strong flow recirculation develops for both inhalers. Note that the capsule chamber is much smaller for the Unihaler. The flow inside the capsule chamber would be of course affected by the presence of a capsule, which is however not considered here. Naturally, the strongly swirling flow will result in a centrifuging of the particles, strongly depending on their size.

The turbulent kinetic energy for both inhalers within the same planes is shown in Figure 3 are presented in

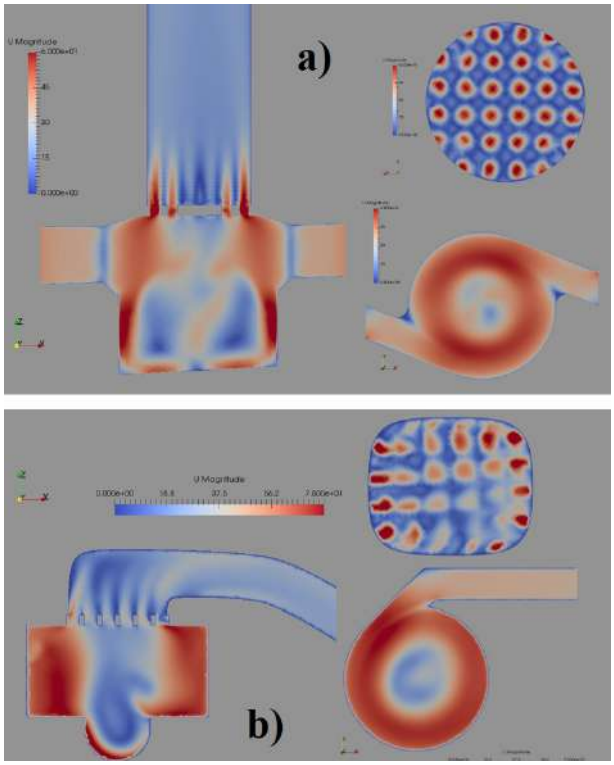

Figure 3: Numerically obtained velocity magnitudes within different planes of the inhaler, left parts: vertical middle-plane, lower-right: planes through the middle of the swirl chamber, top-right: plane just downstream of the grid; **a)** Cyclohaler at 90 l/min, scale 60 m/s and **b)** Unihaler at 60 l/min, scale until 75 m/s, corresponding roughly to the peak inspiration flow rate

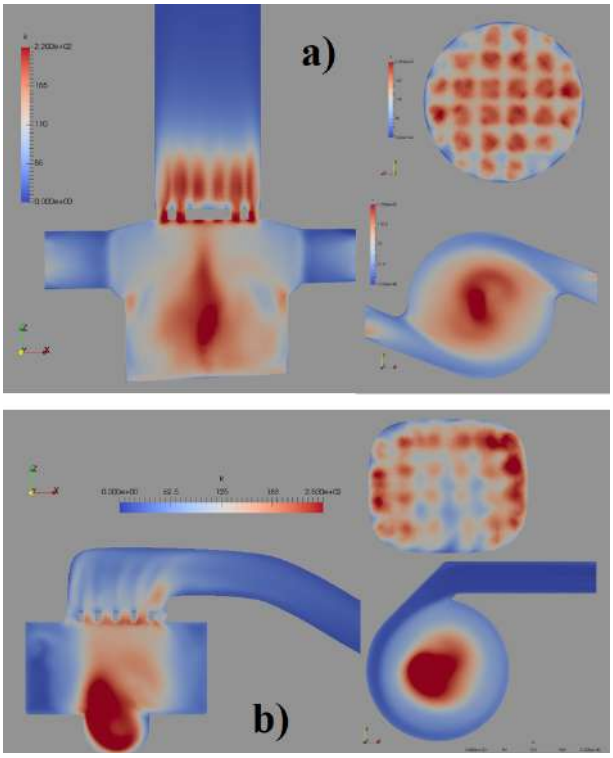

Figure 4: Numerically obtained turbulent kinetic energy within different planes of the inhaler, left part: vertical middle-plane, lower-right: plane through the middle of the swirl chamber, top-right: plane just downstream of the grid; **a**) Cyclohaler at 90 l/min, scale 220 m^2/s^2 and **b**) Unihaler at 60 l/min, scale until 250 m^2/s^2 , corresponding roughly to the peak inspiration flow rate

Figure 4. Expectedly, the highest turbulence is found in the core of the vortex established in the swirl chamber, however slightly shifted downwards into the capsule chamber. Moreover, just downstream of the rigid grid installed at the entrance of the mouthpiece turbulence is very high. In the case of the Unihaler the asymmetric flow entrance cases also an inhomogeneous distribution of turbulence downstream of the grid.

The two considered inhalers rely on a capsule-based delivery of the drug particles, either in form of agglomerated drug powder or as blended carrier particles (Sommerfeld et al. 2019). For being respirable such drug powder should be smaller than 5 μm. The capsule size to be used in both inhalers is SIZE3 having a diameter of about 5.83 mm and a length of 15.9 mm. At the beginning of the inhalation process, the capsule, placed in the capsule chamber, is pierced by needles from both face sides, yielding hole diameters of about 0.6 mm in this case. Hence, thereafter the drug particles may be drawn out of the capsule and are transported through the inhaler. This situation and the presence of a capsule initially located in the capsule chamber were not considered in the present simulations. In a later stage the capsule is lifted upwards by the breathing airstream (Shur et al. 2012) and begins to rotate within the swirl chamber continuously releasing drug particles (Benque and Khinast 2019). For considering this capsule behaviour, fully unsteady numerical simulations would be required which was beyond the scope of the present studies.

In order to circumvent such a complicated and generally unknown drug particle release three possible drug powder release or injection procedures were considered. In any case the starting point of the Lagrangian computations was the converged steady-state flow field as illustrated in Figure 3.

In the first two cases about 2500 stationary particles were released with zero initial velocity from a cuboidal arrangement, once placed in the capsule chamber and secondly positioned within the swirl chamber, as illustrated in Figure 5 for the Cyclohaler. These two injection modes were also realised for the Unihaler with a similar initial arrangement of the drug particles. For the third particle injection mode (only used for the Cyclohaler), the particles were continuously released from the face sides of a fictitious capsule over a time period of 0.02 s (Figure 5 c)). During this period in total 5025 mono-sized drug particles were injected.

The particle mean diameter was varied between 0.05 μm and 10 μm and particle motion was initiated by the considered fluid forces. The particle tracking simulations were conducted as long as all particles have left the inhaler or were deposited on the walls. This simulation time was of course adapted according to the considered inhaler type and the flow rates.

5 Analysis of Deposition

The drug particle deposition studies were conducted for both inhaler types, different flow rates (stationary fluid flow), a particle size range between 0.05 μm and 10 μm, a number of particle release positions (see Figure 5), as well as various deposition criteria in the B&D deposition model. It should be noted that for lung deposition only particles below 5 μm are relevant (Sommerfeld et al. 2021).

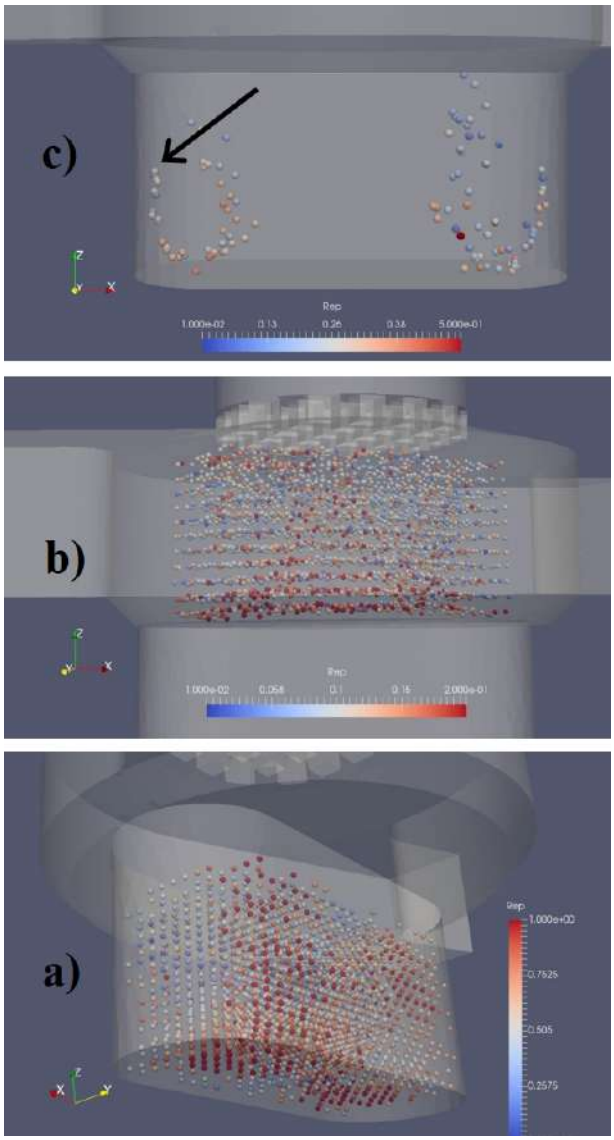

Figure 5: Illustration of the drug particle injection modes considered in this study; **a)** injection mode 1 with about 2500 particles released from the capsule chamber; **b)** injection mode 2 with 2500 particles released from the swirl chamber underneath the grid; **c)** mode 3 with con- tinuous injection of 5025 drug particles from the cap faces of a fictitious capsule, location indicated by the arrow (local release)

The particle material density was selected as 1.5 g/cm^3 representing Lactose and Mannitol powder. As a standard case for the wall material Polystyrene is considered and also compared to cases with glass walls which is a hard and brittle material. All properties for the deposition model, particle density, Young's modulus and Poisson ratio are summarised in Table 2.

The general expectation is that inertial particle deposition increases with particle diameter due to growing particle inertia (Guha 2008). Naturally, also Brownian motion and turbulence intensity could affect local deposition fractions. Brownian effects may be neglected since they are only relevant for particle below 0.05 μm. For getting an idea about particle response, the Stokes numbers based on a system or swirl time-scale ($St_{Sw} = \tau_P/\tau_{Sw}$) and the integral time scale of turbulence ($St_T = \tau_P/T_L$) are calculated. The particle response time scale is calculated as $\tau_P = (\rho_P D_P^2)/(18/\mu)$, the system time scale of the flow is calculated as the radius of the swirl chamber over the tangential inlet velocity $\tau_{Sw} = R_{Sw}/U_t$ and the integral time scales of turbulence is evaluated as the mean value obtained over the entire computed stationary flow field within the inhaler $T_L = 0.16k/\epsilon$. Both, the system time scale as well as the turbulent time scale are expected to decreasing with growing flow rate.

Table 2: Summary of particle and wall mechanical properties in the considered deposition studies for inhalers

Material of Particles and walls	Density [kg/m^3]	Young [GPa]	Poisson ratio [-]
Lactose Particles	1500	1.0	0.4
Mannitol Particles	1500	0.1	0.3
PMMA Particles	1190	5.9	0.4
Polystyrene Wall	1050	4.1	0.35
Glass Wall	2500	80	0.22

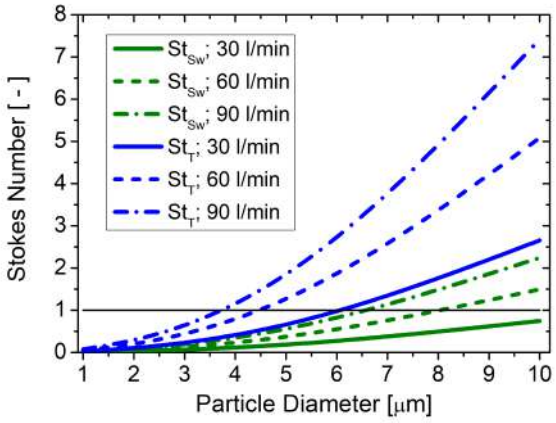

Figure 6: Particle Stokes numbers versus particle size; system or swirl Stokes number St_{Sw} (lower three lines, green) and turbulent Stokes number St_T (upper 3 line, blue) for the three flow rates 30, 60 and 90 l/min with $\tau_{Sw} = 0.562$, 0.281 and 0.187 ms and $T_L = 0.158$, 0.083 and 0.057 ms (Cyclohaler)

The Stokes numbers for the Cyclohaler are depicted in Figure 6. Below St = 1 the particles should respond to the flow field yielding low deposition rates, whereas inertia becomes more dominating above St = 1 associated with a growth of wall collisions and deposition. Only particles below about 4 - 6 μm (with decreasing flow rate) are able to fairly well response to turbulence. On the other hand, particles below 6 - 10 μm are able to follow flow the strongly swirling mean flow field.

Already the values for the Stokes numbers in dependence of particle size indicate that the deposition caused by inertia and turbulence for the 1 μm-particles is relatively small but will continuously grow with particle size.

Hence, such small particles shall follow the mean flow as well as the turbulence structures reasonably well. For the 10 μm-particles the Stokes number related to both effects is well above unity. This behaviour is of course expected from standard deposition curves (Guha 2008).

The particle deposition counts per area of wall surface for three particles sizes (i.e. 1, 2 and 5 μm) are illustrated in Figure 7, magnifying the region of capsule and swirl chamber as well as the grid for the Cyclohaler. In all cases the deposition in the mouth piece is very low anyway. It is clear that the region of remarkable deposition strongly depends on particle size and hence on their

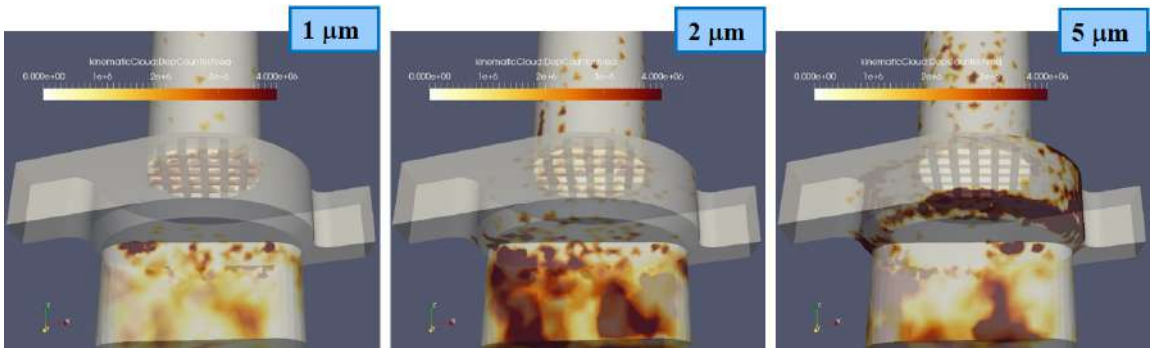

Figure 7: Illustration of the drug particle deposition in the different regions of the Cyclohaler device in dependence of particle size for a flow rate of 90 l/min, B&D deposition model for Lactose particles and Polystyrene wall with k = 0.8 and $\eta = 0.1$, with about 2500 particles released from a cuboidal arrangement in the capsule chamber; **left**: 1 μm, **middle**: 2 μm particles and **right**: 5 μm

inertia. For the 1 μm-particles (Figure 7, left) no deposition is visible in the swirl chamber, as they seem to completely follow the rotating flow (see Figure 6). Some deposition occurs in the capsule chamber, however the majority of particles deposit on the grid. When looking to the 2 μm-particles it is clear that deposition on the grid is reduced as many of the impinging particles are rebound due to inertia (Figure 7, middle). Instead, most of the particles deposit in the capsule chamber and only a few are sticking on the walls of the swirl chamber. When the particles further increase in size (5 μm, Figure 7 right) inertia is further growing and the particles cannot follow the rotating flow and hit the swirl chamber wall where they deposit. However, gravity seems to bring the particles more to the bottom region of the swirl chamber (Figure 7 right). On the grid these larger particles are rarely deposing, but some more deposited particles are seen on the mouth piece wall.

The total deposition in dependence of particle size for different drug particle release locations is illustrated in Figure 8. As mentioned above for all injection modes the deposition fraction continuously increases with particle diameter. Already between 40 to 50% of 1 μm particles may be deposited within the inhaler under the present conditions. The capsule release of 5 μm-particles results yet in a deposition fraction of 85%. When the particles are released in the swirl chamber, just underneath the grid, the deposition of 1 μm particles is about 10% higher than for the capsule release. However, then for the larger particles the deposition from a swirl chamber release is remarkably lower than for capsule release (Figure 8).

The local particle injection from the cap faces of the capsule placed in the capsule chamber interestingly yields the highest deposition fraction for all particle sizes. When assuming for the mode 1 of a capsule release, that all particles impinging on the wall are deposited the deposition fraction is of course quite large and remains for particles larger than 3 μm close to 100% (Figure 8). This result allows concluding that for particle smaller than 1 μm, where deposition is anyway low; there is no strong effect of drug particle release location. Whereas the deposition of larger particles is strongly affected by the release location. The lowest deposition rates are achieved when the particles are released in the swirl chamber.

As already indicated and discussed in Figure 7 the location of particle deposition depends strongly on particle size and response characteristics (see Figure 6) in addition to the release location. In Figure 9 the local deposition fractions are shown for the capsule and swirl chamber as well as the grid and the mouthpiece. This

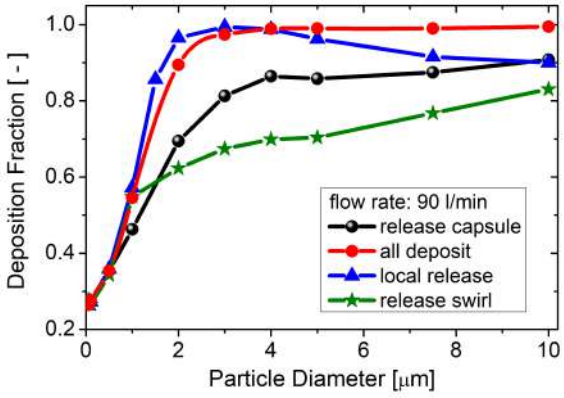

Figure 8: Total drug particle deposition fraction in dependence of their size considering different release or injection modes as summarised in Figure 4 for Lactose particles and a polystyrene wall as listed in Table 1 (Cyclohaler at flow rate 90 l/min)

again quantifies the fact that small particles are most likely to deposit on the grid (see also Figure 7) for both release locations (mode 1 and mode 2). The grid deposition maximum is found for the 1 μm-particles and beyond 4 μm the deposition on the grid can be neglected. Particles between 2 and 4 μm are preferably deposited in the capsule chamber mainly for the capsule chamber release of the particles. Then for particle diameters larger than 2 μm a continuous increase of the deposition in the swirl chamber is observed for further growing particle size due to the increasing particle inertia and associated centrifuging (Figure 9). This is the case for both release locations capsule and swirl chamber. The deposition in the mouthpiece is comparatively low and shows a maximum for 5 μm particles in both release modes.

In the following the total deposition fraction in dependence of particle size will be analysed for different flow rates of the Cyclohaler and also compared with the Unihaler at a flow rate of 60 l/min producing about the same pressure drop as for the Cyclohaler at 90 l/min (Figure 10). It is obvious, that the deposition fraction for particles below 5 μm is remarkably lower for the Cyclohaler with a low flow rate of 30 l/min compared to 90 l/min. This is a result of the reduced particle-wall collision probability whereby deposition may occur less often. The Unihaler at a comparable flow rate shows slightly higher deposition fractions as the Cyclohaler at

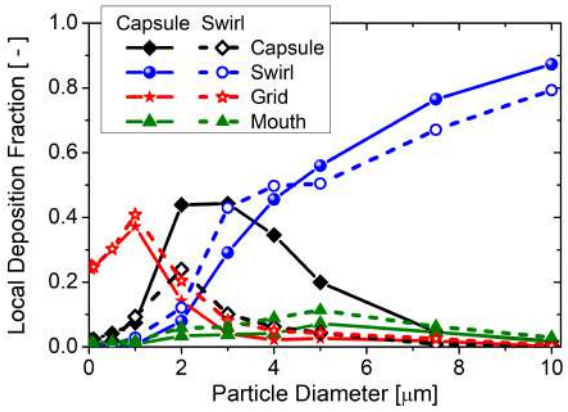

Figure 9: Particle deposition fraction in the different regions of the Cyclohaler (capsule and swirl chamber, grid and mouthpiece) in dependence of particle diameter for particle release in the capsule (mode 1) and swirl chamber (mode 2) at a flow rate of 90 l/min

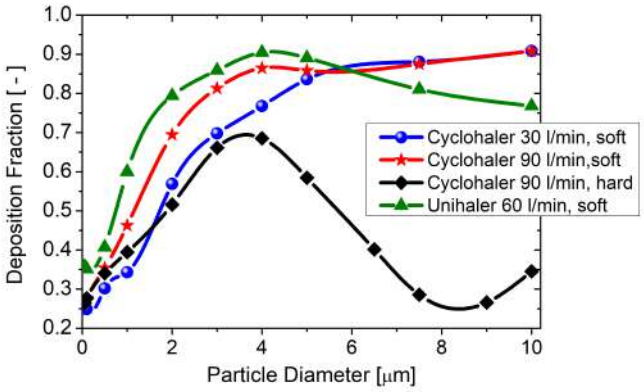

Figure 10: Total drug particle deposition fraction in dependence of their size considering different flow rates for the Cyclohaler (30 and 90 l/min) and a comparable flow rate for the Unihaler (60 l/min) using Lactose particles and a Polystyrene wall (these wall interactions are characterised as soft) as well as a case for the Cyclohaler at flow rate 90 l/min using PMMA particles and a glass wall (this is called hard), for both inhalers particle release from the capsule chamber

90 l/min which is mainly associated with the single, one-sided inlet (see Figure 2) and the associated higher gas velocities inside the inhaler.

The deposition locations in the Unihaler for the three particle sizes are slightly different as observed in the Cyclohaler (compare Figure 7 and Figure 11). In the Unihaler 1 μm particles are not so strongly deposited on the grid, rather particles are also found in the capsule and swirl chamber, but also in the mouth piece. Note that in the Cyclohaler particles of 1 and 2 μm are not at all deposited in the swirl chamber. This is most likely associated with the one-sided inlet and the high tangential velocities (see Figure 3). The 2 μm particles are preferably de- posited in the capsule chamber; some particles are found on the swirl chamber walls and very little is seen on the grid (Figure 11). The largest considered particles (5 μm) are preferably deposited in the swirl chamber and show, due to the one-sided inlet, a nice spiral pattern of deposition. Almost no large particles are deposited on the grid.

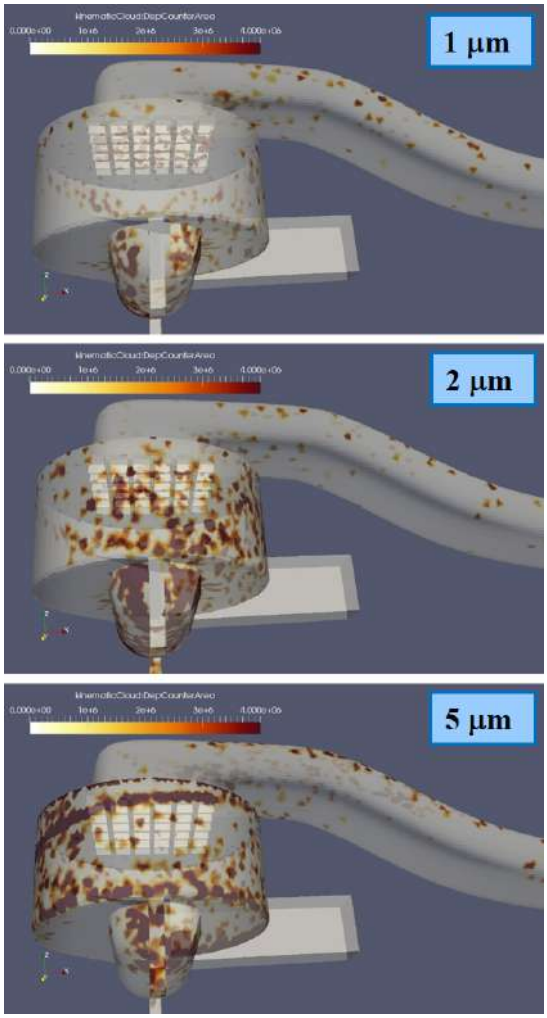

Figure 11: Illustration of the drug particle deposition in the different regions of the Unihaler device in dependence of particle size for a flow rate of 60 l/min, B&D deposition model for Lactose particles and Polystyrene wall with k = 0.8 and η = 0.1, with about 2200 particles released from a cuboidal arrangement in the capsule chamber; top: 1 μm, middle: 2 μm particles and bottom: 5 μm

When considering hard particle and wall materials, the deposition fraction is remarkably reduced since the critical velocity is much lower comparted to the Lactose/Polystyrene combination (see Table 1). Hence, most collisions result in particle rebound which is especially seen for particles larger than about 3.5 μm. It is however not clear in as much such a hard material combination may be realisable with real drug particles and commer- cially available inhaler devices.

Since for an inhaler design the fraction of emitted particles in each size fraction is more interesting these results are summarised in Figure 12 for both inhalers with increasing flow rate. In general, the flow rate dependence is stronger for the Unihaler. For the smallest particles considered, i.e. below about 2 μm, the Unihaler yields remarkably lower emissions than for the higher flow rates as a result of stronger deposition. For particles below 0.5 μm the emission of the Cyclohaler is independent of flow rate and for the lager particles the difference is only 10%. At higher flow rates the Cyclohaler is somewhat better as the Unihaler in terms of the emitted particle fractions. Since during a breathing process the flow rate is strongly varying the Cyclohaler shows the better performance.

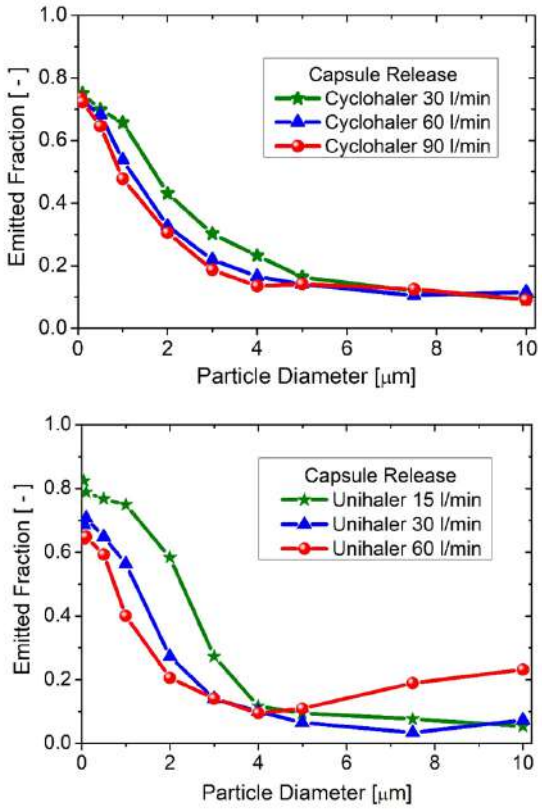

Figure 12: Total drug particle emitted fraction in dependence of their size considering different flow rates for Lactose particles and a polystyrene wall as listed in Table 1, comparison of Cyclohaler and Unihaler with particle release in the capsule chamber

6 Conclusions

Dry powder Inhaler devices are known to have a quite low efficiency regarding the delivery of fine drug particles below 5 μm to the human pulmonary airways. One reason for that may be the drug particle deposition on the inhaler walls for both formulations; carrier based or powder delivery, where the dose is mostly administered through capsules. Therefore, the deposition of fine drug particles in two inhaler devices was analysed through numerical simulations with an Euler/Lagrange approach. The occurrence of deposition was described by an energy-based approach (Brach and Dunn 1992) yielding a critical velocity below which deposition happens. This critical velocity is depending on the properties of particle and wall materials and model calculations by this model gave excellent agreement with measurements.

With regard to deposition in inhaler devices it was shown that the deposition fraction is first of all strongly depending on the particle release location. Only a full simulation with rotating capsule and proper particle release from the openings of the capsule could solve this problem (Benque and Khinast 2019). It could be shown that for the considered swirl type inhalers with a grid at the mouthpiece entrance very fine particles (≈ 1 μm) deposit preferably on the grid, intermediate sizes (≈ 2 - 3 μm) are captured in the capsule chamber and larger particles (> 5 μm) preferably deposit in the swirl chamber due to inertia. A variation of flow rate as occurring for a realistic inhalation process does not drastically change of deposition fraction for the Cyclohaler. A possibility for reducing deposition is the use of harder particle and wall materials which reduces the critical velocity. With respect to the drug powder emission the original Cyclohaler still seems to be the best choice when only looking at the emitted fraction.

Acknowledgements

The presented research was initiated through cooperation within the COST Action MP 1404 “SimInhale” (European Cooperation in Science and Technology; `www.cost.eu`). The author thanks Mr. Manuel Taborda for creating the numerical grid and supporting the numerical simulations with his advice.

References

[1] Ariane, M., Sommerfeld, M., Alexiadis, A. (2018) Wall collision and drug-carrier detachment in dry powder inhalers: Using DEM to devise a sub-scale model for CFD calculations. Powder Technology, Vol. 334, 65 - 75.

[2] Benque, B. and Khinast, J.G.: Understanding the motion of hard-shell capsules in dry powder inhalers. Int. J. of Pharmaceutics, Vol. 567, 118481 (2019)

[3] Brach, R.M. and Dunn, P.F.: A mathematical model of the impact and adhesion of microspheres. Aerosol Science and Technology, Vol. 16, 51 - 64 (1992)

[4] Coates, M.S., Fletcher, D.F., Chan, H.-K., Raper, J.A.: Effect of design on the performance of a dry powder inhaler using computational fluid dynamics. Part 1: Grid structure and mouthpiece length. Journal of Pharmaceutical Sciences, Vol. 93, 2863 - 2876 (2004)

[5] Cui, Y., Sommerfeld, M.: Application of Lattice-Boltzmann Method for Analysing Detachment of Micron-Sized Particles from Carrier Particles in Turbulent Flows. Flow Turbulence and Combustion, Vol. 100, 271 - 297 (2018)

[6] Cui, Y., Sommerfeld, M.: The modelling of carrier-wall collision with drug particle detachment for dry powder inhaler applications. Powder Technology, Vol. 344, 741 - 755 (2019)

[7] Donovan, M.J., Kim, S.H., Raman, V. & Smyth, H.D.: Dry powder inhaler device influence on carrier particle performance. Journal of Pharmaceutical Sciences, Vol. 101, 1097 - 1107 (2012)

[8] Friebel, Ch.: Rationale Entwicklung eines Inhalationssystems. Dissertation, Mathematisch-Naturwissen-schaftliche Fakultät der Christian-Albrechts-Universität Kiel (2010)

[9] Guha, A: Transport and Deposition of Particles in Turbulent and Laminar Flow. Annu. Rev. Fluid Mech. Vol. 40, 311-341 (2008)

[10] Hertz, H.: Über die Berührung fester elastischer Körper. J. Reine Angew. Math. Vol. 92, 156 - 171 (1882)

[11] Hiller, R.B.: Der Einfluss von Partikelstoßund Partikelhaftung auf die Abscheidung in Faserfiltern, Dissertation, Universität Karlsruhe, VDI-Verlag GmbH Düsseldorf (1981)

[12] Johnson, K.L., Kendall, K., and Roberts, A.D.: Surface energy and the contact of elastic solids. Proc. R. Soc. Lond. Vol. A324, 301-313 (1971)

[13] Milenkovic, J., Alexopoulos, A.H., Kiparissides, C.: Flow and particle deposition in the Turbohaler: A CFD simulation. International Journal of Pharmaceutics Vol. 448, 205 - 213 (2013)

[14] Ruzycki, C.A., Javaheri, E., Finlay, W.H.: The use of computational fluid dynamics in inhaler design. Expert Opinion Drug Delivery, Vol. 10, 307 - 323 (2013)

[15] Sommerfeld, M. and Huber, N.: Experimental analysis and modelling of particle-wall collisions. International Journal of Multiphase Flow, Vol. 25, 1457-1489 (1999)

[16] Sommerfeld, M., van Wachem, B. and Oliemans, R.: Best Practice Guidelines for Computational Fluid Dynamics of Dispersed Multiphase Flows. ERCOFTAC (European Research Community on Flow, Turbulence and Combustion), ISBN 978-91-633-3564-8 (2008)

[17] Sommerfeld, M., Schmalfuß, S.: Numerical analysis of carrier particle motion in dry powder inhaler. ASME Journal of Fluid Engineering, Vol. 138, Paper 041308 (2016).

[18] Sommerfeld, M., Cui, Y. and Schmalfuß, S.: Potentials and Constraints for the Application of CFD Combined with Lagrangian Particle Tracking to Dry Powder Inhalers. European Journal of Pharmaceutical Sciences, Vol. 128, 299 - 324 (2019)

[19] Sommerfeld, M., Sgrott Jr. O.L., Taborda, M.A., Koullapis, P., Bauer, K. and Kassinos, S.: Analysis of flow field and turbulence predictions in a lung model applying RANS and implications for particle deposition. European Journal of Pharmaceutical Sciences, Vol. 166, 105959 (2021)

[20] Shur, J., Lee, S., Adam, W., Lionberger, R., Tibbats, J. and Price, R.: Effect of device design on the In Vitro performance and compatibility for capsule-based dry powder inhalers. The AAPS Journal, Vol. 14, 667 - 676 (2012)

[21] Telko, M.J. and Hickey, A.J.: Dry powder inhaler formulation. Respiratory Care, Vol. 50, 1209 - 1227 (2005)

[22] Thornton, C. and Ning, Z.: A theoretical model for the stick/bounce behaviour of adhesive, elastic-plastic spheres. Powder Technology, Vol. 99, 154 - 162 (1998)

[23] Tong, Z., Kamiya, H., Yu, A., Chan, H.-K. and Yang, R.: Multi-scale modelling of powder dispersion in a carrier-based inhalation system. Pharm. Res. Vol. 32, 2086 - 2096 (2015)

[24] van Wachem, B., Thalberg, K., Remmelgas, J., Niklasson-Björn, I.: Simulation of dry powder inhalers: Combining micro-scale, meso-scale and macro-scale modeling. AIChE Journal, Vol. 63, 501 - 516 (2017)

[25] Venturini, P.: Modelling of particle-wall deposition in two phase gas-solid. Ph.D. Thesis, Sapienza Universitá di Roma, Italy (2010) flows Ph.D. Thesis. Sapienza Universitá di Roma, Italy, 2010

[26] Wall, S., John, W. and Wang, H.C.: Measurements of kinetic energy loss for particles impacting surfaces. Aerosol Science and Technology, Vol. 12, 926 - 946 (1990)

[27] Wong, W., Fletcher, D.F., Traini, D., Chan, H.-K., Yong, P.M.: The use of computational approaches in inhaler development. Advanced Drug Delivery Reviews, Vol. 64, 312 - 322 (2012)

How Flow Rate, Head Position, and Inhaler Orientation Affect the Drug Deposition in the Mouth-Throat

F.S. Stylianou[1], P.G. Koullapis[1], B. Olsson[2], and S.C. Kassinos[1,3]

[1] *Computational Sciences Laboratory (UCY-CompSci), Nireas-International Water Research Centre, University of Cyprus*
[2] *Emmace Consulting AB, Lund, Sweden*
[3] *Department of Mechanical & Manufacturing Engineering, University of Cyprus*

Abstract

The mouth-throat plays a key role in the administration of inhaled medicines. It is an area of intense filtration, where an unacceptably high fraction of the released drug dose is deposited and thus wasted. Due to the relatively high flow rate associated with Dry Powder Inhalers (DPIs), drug particles are released at a high velocity, which causes substantial deposition in the oral cavity and the throat region by inertial impaction. Hence, reducing the mouth-throat deposition is of utmost importance and this can only be achieved by designing more efficient inhaler devices (functioning at lower flow rates) and by obtaining a better understanding of the mechanisms that cause the oropharyngeal losses.

This study is designed to identify the main factors that determine aerosol deposition (unwanted filtering) in the mouth-throat region, with the aim of controlling the leading effects that contribute to the oropharyngeal deposition losses for drugs delivered via DPIs. For this reason micron-sized particles are released and tracked in a patient-specific MRI-based mouth-throat geometry under three inhalation flow rates (15L/min, 30L/min, 60L/min), three head positions (straight, up, left), and three inhaler mouthpiece orientations (0^o, 15^o, 30^o). Direct Numerical Simulations (DNS) are performed for the low flow rate using prescribed laminar inlet conditions, while Large Eddy Simulations (LES) are performed for the intermediate and high flow rates using fully-developed turbulent inlet conditions.

Interestingly, our results reveal that the deposition fraction is insensitive to the head position, whilst the inhalation flow rate and the inhaler mouthpiece orientation have a strong influence on the aerosol deposition in the mouth-throat region. The flow rate dependence agreed very well with the results of a semi-empirical algebraic 1D mouth-throat deposition model. Furthermore, we illustrate the mean flow structures and examine their effect on the particle deposition of various micron sizes.

1 Introduction

Pulmonary delivery is a regular drug administration method for medicines. In the case of respiratory ailments, inhalation provides the shortest and most direct route to the target site, thus minimising side effects and maximising effectiveness. In the case of systemic diseases, pulmonary delivery often offers a fast administration mode (second only to injection) and other significant benefits, such as a large surface area for deposition and absorption, and limited enzymatic activity as compared to the gastrointestinal route [1]. Despite these significant advantages and the promise held, a number of problems hinder wider adoption of inhalation as a primary administration route. One of these problems, which forms the subject of the present study, is the unacceptably high fraction of the released drug dose that never reaches its target site.

The mouth-throat plays a key role during pulmonary drug delivery. It is an area of intense filtration, where a sizeable portion of the released drug is deposited and thus never reaches the conducting and respiratory airways. In fact, drug deposition in the targeted area of the lung (typically the lower respiratory tract) from currently marketed DPIs is roughly between 7.5% and 40% of the label claim, depending on the inhaler design and type of formulation used [2, 3, 4, 5].

For low dose drugs, mostly adhesive mixtures are used, in which the micronised drug particles are attached by simple mixing to the surface of much larger carrier particles, primarily by van der Waals forces. This is done to dilute the powder and improve its flow properties. Liberation of the drug particles during inhalation is done through separation forces derived from the kinetic energy of the inhaled airflow. Liberation is only partial, however, and depending on the inhaler design and its resistance to airflow, often requires a relatively high flow rate.

For example, no more than 15% to 60% of the label claim is released from the DPI as Fine Particle Dose (FPD) having the appropriate aerodynamic size range ($1 - 5\mu m$) for lung deposition. Furthermore, due to the relatively high flow rate needed, the drug particles are released from DPIs at a high velocity, which causes substantial deposition in the oral cavity and the throat region by inertial impaction, often more than 50% of the delivered FPD. This leaves between 7.5% to 30% of the label claim for deposition in the target area.

It is only for some carrier-free drug formulations that higher lung deposition fractions (up to 40% of the label claim) have been reported [6]. It is evident that, drug losses in the mouth-throat region remain at unacceptably high levels (often more than 50%), especially for DPIs.

2 Previous Studies on Intra- and Inter-Subject Variability

There is a rich scientific literature in the field of pulmonary drug delivery, which is impossible to fit in a small section. Here we review a handful of in silico and in vitro studies, that are in the same spirit with the current work due to intra- and/or inter-subject geometrical variation in the area of mouth-throat-trachea.

Xi et al. (2016) [7] performed an impressive parametric in silico study to evaluate the relative importance of mouth-throat geometrical factors (i.e. oral cavity vol-

ume, glottis area, airway curvature, airway volume) on the deposition of orally inhaled aerosols. Their results showed that the realism of airway models significantly affected the mouth-throat deposition, and the USP induction port underestimated realistic models by up to 55%. The glottis area and total airway volume were found to be the two most predominant factors.

Xi et al. (2018) [8] numerically investigated the influences of the glottis motion on airflow features and energy expenditure in an image-based human upper airway model. Both static and dynamic glottal apertures were considered using Large Eddy Simulation under either constant or sinusoidal breathing profiles. A widening glottis during inhalation was observed to significantly postpone the development of vortices, flow oscillation, and intra-glottal pressure drop, which might have key biological implications in alleviating the diaphragm muscle effort and reducing the risk of pharyngeal wall collapse. Although particle deposition was not studied, large differences are expected between constant and cyclic flows.

Xi and Yang (2019) [9] in an attempt to evaluate the effects of tongue position on the delivery efficiency of orally inhaled pharmaceuticals, they developed a computational oropharyngeal model with varying tongue shapes, representative of the positions a subject takes during pulmonary drug delivery. Their results show that tongue position can significantly alter the airflow pattern and particle behaviours in the oral cavity and the subsequent pharyngeal airway. The variability in the total oropharyngeal filtering rate was 6%-25% and varied with particles sizes and breathing conditions. The effects from tongue positioning were also observed in the particle distributions that entered the lungs, which might further cause differences in the pulmonary deposition distributions.

Koullapis et al. (2018) [10] used three mouth-throat geometries, with significantly different geometric and filtering characteristics, to assess the role of the extrathoracic airways in determining regional deposition in the upper bronchial airways. Using Large Eddy Simulations, they where able to show that large flow field differences in the extrathoracic airways across the three geometries largely die out below the main bifurcation. Importantly, localised deposition fractions are found to remain practically identical for particles with aerodynamic diameters of up to $d_p = 4\mu m$ and $d_p = 2.5\mu m$ at 30 and 60 L/min, respectively. For larger particles, differences in the localised deposition fractions are shown to be mainly due to variations in the mouth-throat filtering rather than upstream flow effects or differences in the local flow field.

Feng et al. (2018) [11] created a virtual population group of seven distinct and widely used human upper-airway configurations with the same tracheobronchial tree. Their inter-subject variability analysis indicate that the glottis constriction is the morphological parameter that significantly impacts the inhaled particle dynamics in the respiratory tract. They concluded that the anatomical features of the upper airways should be maintained to capture the personalised airflow and particle transport dynamics for particles smaller than $500nm$ or larger than $2\mu m$. For particles in the range $500nm < d_p < 2\mu m$, a single upper airway model representing a basic subpopulation group, can be employed to evaluate the total deposition.

Golshahi et al. (2012) [12] used in vitro methods to quantify the deposition of micrometer-sized aerosols in CT based oropharyngeal airway replicas of children. Using geometry dimensions, they establish a non-dimensional correlation for children, consisting of Stokes and Reynolds numbers, to reduce the scatter in deposition.

Choi et al. (2009) [13] investigated the effects of intra- and inter-subject variabilities in airway geometry on airflow in the human airways using Large Eddy Simulation. For inter-subject study, two morphological factors are found to significantly affect the flows between subjects. These are the constriction ratio of the glottis with respect to the trachea and the curvature and shape of the airways.

Heenan et al. (2004) [14] performed measurements of airflow and particle deposition in two realistic extrathoracic airway geometries of the same subject. They revealed a strong connection between local deposition and local fluid mean velocity field, indicating inertial impaction as the dominant deposition mechanism. Their results serve to illustrate the major effect intra-subject geometric variability can have on the extrathoracic flow field and resulting regional deposition.

DeHaan and Finlay (2001) [15] performed experiments to determine the effect of six different inhalation devices on the aerosol deposition in an idealised mouth-throat geometry under various steady inhalation flow rates. The amount of deposition in the mouth-throat region was found to depend on the type of device that the aerosol entered through. Deposition with the DPIs was found to be up to 14 times greater than that with a simple straight tube of $1.7cm$ diameter. Thus, the inhaler geometry that the aerosol passes through prior to entering the mouth and throat region can greatly affect the deposition in the mouth-throat.

DeHaan and Finlay (2004) [5] extended their previous work by using a variety of mouth inlets ranged in diameter from 3 to 17 mm and included contraction nozzles, straight tubes, and a turbulence generator. From their measurements they derived a model for predicting the oral cavity deposition based on the particle Stokes number near the primary impaction location modified to incorporate the turbulent kinetic energy at the inlet.

Grgic et al. (2004) [16] performed measurements of the flow field and aerosol deposition in an idealised average human mouth-throat replica. They showed that both flow rate and particle size have a significant effect on deposition efficiency, indicating that inertial impaction is the dominant deposition mechanism. Nasopharyngeal and glottal constrictions are the key morphological factors affecting downstream flow patterns and thus deposition in the laryngeal area and upper trachea.

Grgic et al. (2004) [17] extended their previous work to several realistic mouth-throat geometries in order to demonstrate the effects of intra-subject and inter-subject variations in geometry on deposition efficiency. They found that both total and regional deposition exhibit large inter-subject differences, as well as intra-subject variability to a lesser extent. Deposition was found to occur primarily via impaction, and the mouth area was identified as the largest obstacle for inhaled aerosols. An empirical Reynolds number correction, $Re^{0.37}$, was applied to the Stokes number St, which reduced scatter in the reported deposition efficiencies, and provided better collapse of their data onto a single curve.

Nicolaou and Zaki (2013) [18] examined the airflow in a subset of four mouth-throat geometries used in [17]. By using Direct Numerical Simulations, they were able to related the predicted airflow to the variations in deposition observed in [17]. It was found that geometric variation, even within the same subject, has a large impact on both the mean velocity profiles and the turbulence intensities. Their analysis revealed that the empirical cor-

relation $StRe^{0.37}$ arises due to the fact that deposition in the airways occurs via both impaction and turbulent dispersion.

Zhang et al. (2007) [19] investigated the polydisperse aerosol deposition, emitted from two commercial inhalers, in three mouthâĂŞthroat models (i.e. USP induction port, idealised mouthâĂŞthroat, and highly idealised mouthâĂŞthroat). The USP induction port gave the lowest deposition among the three mouthâĂŞthroat models studied, while the results from the idealised geometries were in good agreement with available in vivo data from the literature.

Lin et al. (2001) [20] examined the effect of mouthpiece diameter (with sizes 1.5, 2.0, and 2.7 cm) on the deposition efficiency of inertial size particles (with sizes 2, 4, and 8 μm) in adult human oral-pharyngeal-laryngeal airway cast models at various inspiratory flow rates. Their results show that the effect of mouthpiece diameter varies with particle size, with 2 and 8 μm particles least affected.

Zhou et al. (2011) [21] studied experimentally the aerosol deposition in three different mouthâĂŞthroat models (i.e. USP induction port, idealised Alberta, and subject specific LRRI). The deposition results between the Alberta and LRRI models agreed well and were within the range of other in vivo data of the literature.

McRobbie et al. (2003); Pritchard and McRobbie (2004); McRobbie and Pritchard (2005); Burnell et al. (2007) [22, 23, 24, 25] performed a series of studies on human oropharyngeal airspaces. They examined the anatomical geometry of the upper airways of 20 volunteers (based on 3D inhalation-gated MRI) when using four dummy inhalation devices with varying mouthpiece diameters and airflow resistances. From the 80 data sets they selected 12 scans to produce models with varying dimensions that span the adult population. In an in vitro analysis, the models were used to determine the retention effect of the oropharyngeal airspaces when drug aerosols were administered from four inhalation delivery systems. Characterising the throat models by measuring 51 different dimensional variables enabled determination of the most influential variables for dose retention for each inhalation delivery system. Throat model retention was found to be dependent on the delivery system. The most influential variable was the total throat model volume.

Delvadia et al. (2012, 2013, 2013, 2016); Wei et al. (2017, 2018) [26, 27, 28, 29, 30, 31] performed an impressive series of in vitro tests for aerosol deposition which correlated well with in vivo data. Among the parameters they have studied were: the size of upper airways, the inhaler insertion angle, the inhalation profile, different inhalers, and different mouth-throat models.

3 Methodology and Implementation

To generate physiologically realistic mouth-throat geometries under three head positions (head-straight, head-up, head-left), MRI scanning was performed on the first author (Sex: male, Age: 32y, Height: 1.76m, Weight: 74kg, at the time of scan) at the Prognosis Advanced Diagnostic Center located in Larnaca, Cyprus. During the three MRI scans, a DPI mouthpiece was held between the lips of the subject, emulating the proper opening of the mouth-throat during inhalation from an inhaler. Great care was taken during the MRI scan of the head-straight position, in order to produce clear images of sufficient quality. The same was not achieved for the head-up and head-left positions, due to the inconvenient head posture inside the head-neck MRI coil, which prompted frequent swallowing, leading to blurry images.

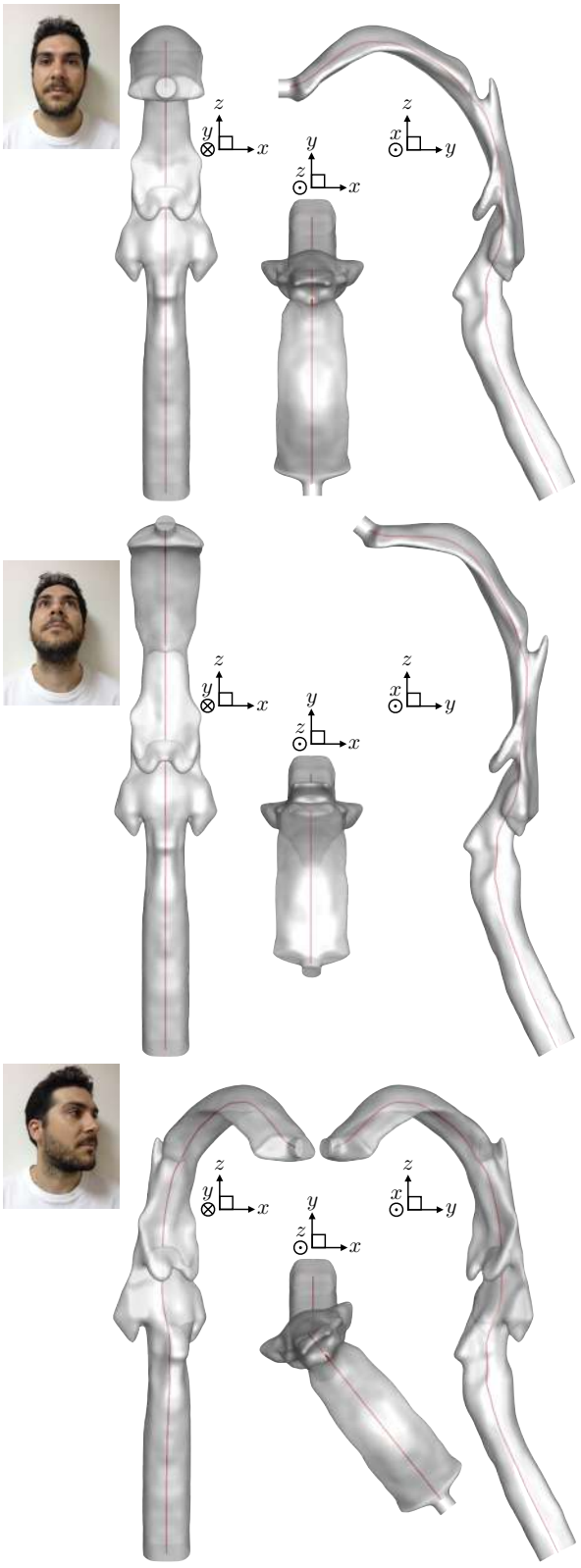

Figure 1: Front, top, and side viewpoints for each of the three distinct head positions: head-straight, head-up, head-left

The three MRI data sets were processed with the Simpleware ScanIP software and 3D mouth-throat models

were generated. Great effort was put during the 3D reconstruction of the mouth-throat model with head-straight position (Figure (1), first row), while for the head-up and head-left positions only crude models were constructed as a result of the aforementioned blurriness in the MRI images. Note that left-right symmetry was applied to the MRI data of the head-straight position in order to increase the quality of the data and to produce a symmetric model.

The final mouth-throat models with head-up (Figure (1), second row) and head-left (Figure (1), third row) positions were obtained from geometric transformations of the head-straight model. In this process the aforementioned crude models were used as guidance. Prior to the geometric transformations, a skeletonization process was applied on the head-straight model, which resulted into a representative centreline for the 3D model (see Figure (1)). Rotational transformations, spread across specific regions of the skeleton centreline, were used to convert the head-straight model into head-up (x-axis rotations, with cumulative rotation angle -39.10°) and head-left (z-axis rotations, with cumulative rotation angle $+38.55^{\circ}$) models.

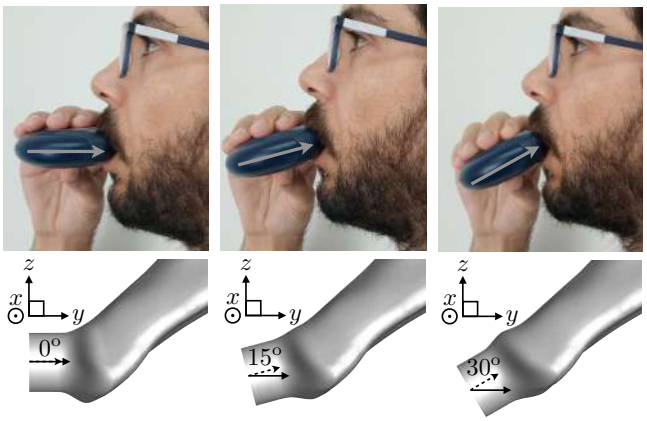

Figure 2: Three inlet orientations emulating three different angle positions of an inhaler mouthpiece between the lips

To assess the effect of the inhaler orientation on the mouth-throat airflow and particle deposition, three distinct inlet parts were designed and merged with the head-straight mouth-throat model. Figure (2) illustrates the three inlet orientations adopted (i.e. 0°, 15°, 30°). For the head-up and head-left mouth-throat models the three inlet parts are subjected to the rotational transformations described in the previous paragraph. Thus the relative orientation of an inlet part with the lips is the same in all three head positions.

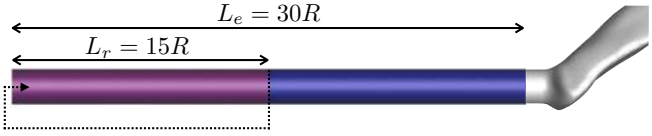

Figure 3: For the intermediate and high flow rates, the imposition of the recycling boundary condition scheme requires an extruded inlet section

In addition to the three head positions and the three inhaler orientations, three inhalation flow rates are also adopted (i.e. Q=15/30/60L/min). Based on the airflow properties (kinematic viscosity ν_f=1.6601×10^{-5}m^2/s and density ρ_f=1.1422kg/m^3 at body temperature T=36°C), the inlet dimensions (circular cross sectional area $A=\pi R^2$ with radius R=4mm), and the three inhalation flow rates Q, the corresponding bulk Reynolds numbers $Re_b=\frac{2Q}{\nu\sqrt{\pi A}}$ are $Re_b\approx$2397/4794/9587. The associated bulk velocities $u_b=\frac{\nu Re_b}{2R}$ are $u_b\approx$4.97/9.95/19.89m/s.

For the low inhalation rate, the associated bulk Reynolds number falls into the laminar regime and thus we use fully developed laminar inlet conditions. On the contrary, for the intermediate and high flow rates the associated bulk Reynolds numbers fall into the turbulent regime. For these cases, we use fully developed turbulent inlet profiles based on a recycling boundary condition scheme. The implementation of this scheme demands the extrusion of the inlet section for a total length of L_e=30R, with the recycling length set to L_r=15R (see Figure (3)). More details about the recycling boundary condition can be found in our previous work [32]. In all cases the convective outlet boundary condition is employed. Although the selected inlet profiles may not be fully representative of those generated from commercial inhalers, they still should be sufficient to highlight the relative differences between the mouth-throat deposition induced from the various combinations of flow rate, head position, and inhaler orientation.

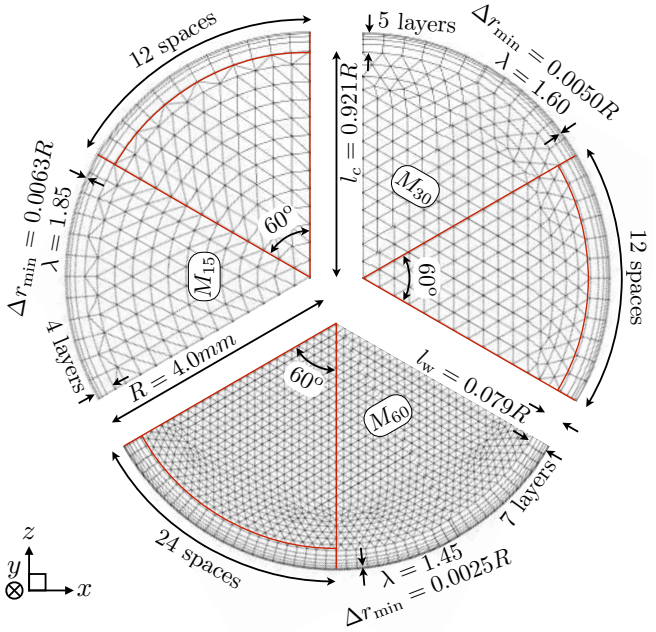

Figure 4: Grid details at the inlet for the 3 mesh densities considered (i.e. M_{15}, M_{30}, M_{60}). Note that $\Delta r_{\min}$ is the first grid node from the wall, and λ is the average expansion ratio of the wall layers

To simulate the low, intermediate, and high flow rates we have generated grids with three mesh densities, namely: M_{15}, M_{30}, and M_{60}. Figure (4) delineates the grid details of these meshes at the inlet, while Figure (5) displays a comparative mesh resolution at various cross sectional areas of the domain for $M_{15}-M_{30}$ and $M_{30}-M_{60}$.

The near wall region is resolved with prismatic elements, while the core of the domain is meshed with tetrahedral elements. The number of grid cells involved in $M_{15}/M_{30}/M_{60}$ is 8.7/10.5/44.4 millions. The M_{30} is obtained via local refinement of M_{15}, with a relative

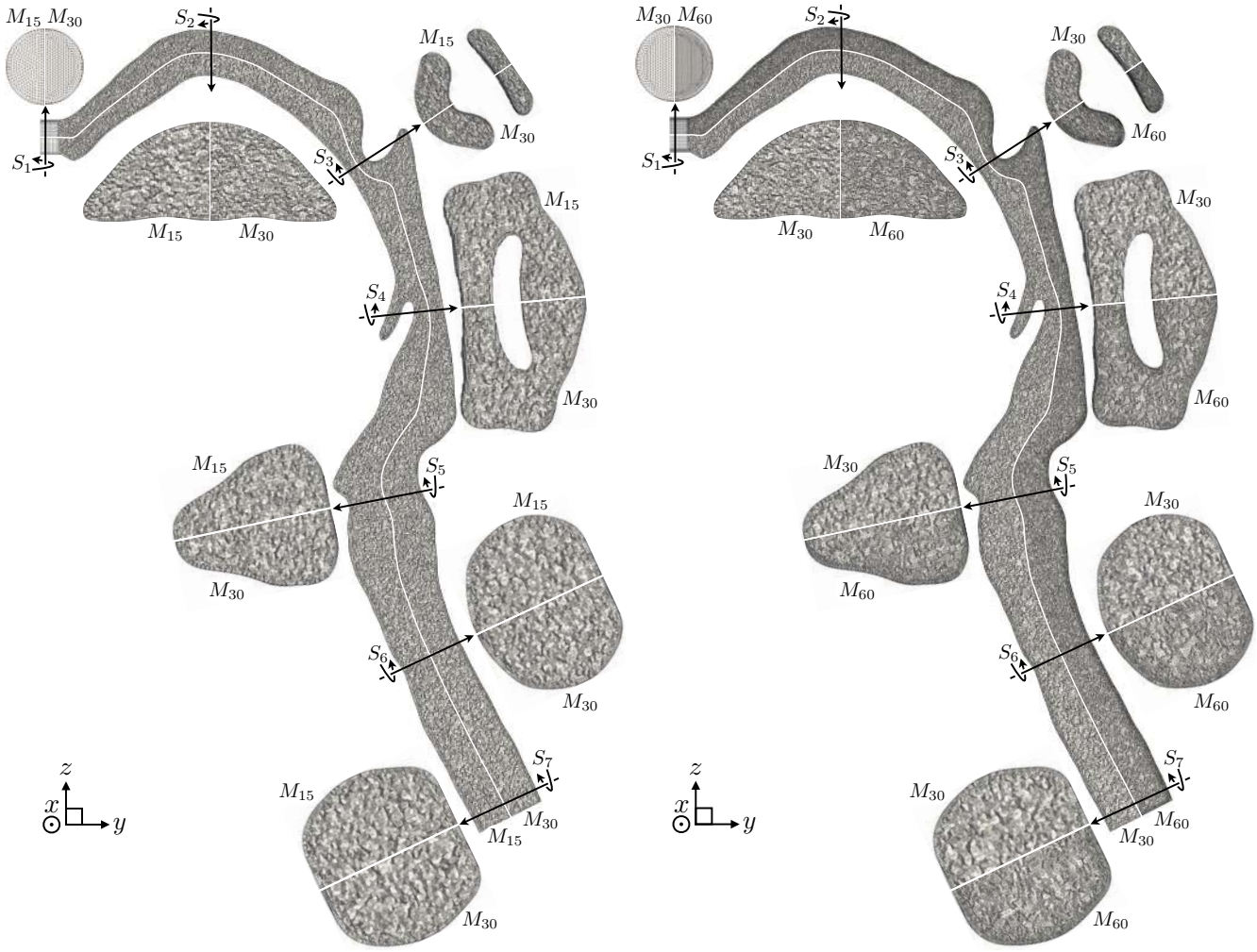

Figure 5: Mesh resolution comparison for $M_{15} - M_{30}$ (left) and $M_{30} - M_{60}$ (right) at eight cross sections (i.e. one at the symmetry plane and seven normal to this plane). The S_1-S_7 cross sections are slightly scaled with respect to the symmetry plane section

increase of grid cells in the volume between stations: $S_1 - S_3$ of 33.5%, $S_3 - S_5$ of 16.3%, and $S_5 - S_7$ of 9.8%. Note that the number of prism layers increases from 4 to 5. The M_{60} is obtained via pure refinement of M_{30}, with the exception of the near wall region where the number of prism layers increases from 5 to 7. Noteworthy of mention is that M_{30} has been constructed *a posteriori* of the low and intermediate flow rate simulations that used M_{15}, while the M_{60} has been constructed *a posteriori* of the high flow rate simulation that used M_{30}. To assess the grid-independence of our results, the low and intermediate flow rates have been simulated with the M_{15} and M_{30}, while the high flow rate has been simulated with the M_{30} and M_{60}. The grid-independence analysis indicated that for all cases the low resolution meshes were adequate. To get a sense of the quality of our meshes we compare with the grids used in the SimInhale benchmark case of the Cost Action MP1404 [33]. For this benchmark case, three meshes have been used, namely LES3/LES2/LES1, of 7/10/50 million grid cells with 3/3/5 near wall prism layers. The simulated airway includes not only the mouth-throat-trachea, but also the main, lobar, and segmental bronchi.

The turbulent inlet conditions, for the intermediate and high flow rates, are accommodated via the extrusion length L_e=30R in which the inlet mesh of $M_{15}/M_{30}/M_{60}$ is repeated for 10/15/20 layers for every streamwise distance of length 1R. Based on the friction velocity u_τ at the inlet pipe section, the friction Reynolds numbers $Re_\tau = \frac{u_\tau R}{\nu}$ for the three flow rates are approximately $Re_\tau \approx 70/165/300$. These values are computed based on a correlation that relates the Re_b with the Re_τ for a fully developed turbulent pipe flow [34]. For the intermediate flow rate, the viscous length unit $\delta = \nu_f/u_\tau$ at the inlet is $\delta \approx 0.00606R$ and thus the near wall radial, circumferential, and streamwise spacings for M_{15} are $(\Delta r)^+_{\min} \approx 1.0$, $(R\Delta\phi)^+_{\max} \approx 14.5$, and $(\Delta s)^+ \approx 16.5$ (where the superscript "+" symbolises normalisation with viscous scales). From the previous analysis, as well as from similar analysis for the remaining combinations of flow rates and mesh densities under consideration, it can be inferred that the $M_{15}/M_{30}/M_{60}$ grids are of high quality and adequate resolution for DNS/LES/LES of the low/intermediate/high flow rates. Note that the Dynamic Smagorinsky model is used in our LES simulations.

The following time steps dt_f=10(10)/10(10)/5(2.8)μs are used for the low/intermediate/high flow rates, leading to maximum CFL values that fluctuate around 0.75(0.74)/1.02(1.10)/1.06(1.08). The numbers in parenthesis correspond to simulations with higher mesh densities (i.e. the following meshes $M_{15}(M_{30})/M_{15}(M_{30})/M_{30}(M_{60})$ are used for the simulation of low/intermediate/high flow rates). Using the volume of the mouth-throat domain $V \approx 0.06L$ and the skeleton line length $L_{sk} \approx 26.4$cm, we can extract

a mean cross sectional area A^m=V/L_{sk} with a value of $A^m \approx 2.27\text{cm}^2$. The associated mean bulk velocities u_b^m=Q/A^m for the three flow rates are estimated to be $u_b^m \approx 1.1/2.2/4.4\text{m/s}$. These are 4.5 times lower than the respective bulk velocities u_b at the inlet. For each case, the effective simulation time (in which statistics are collected and particles are being tracked) is T_{sim}=2.4(2.4)/2.4(2.4)/1.2(0.84)s such that a hypothetical fluid particle traveling with u_b^m velocity, covers 10(10)/20(20)/20(14) times the L_{sk} length.

The dispersed phase is simulated by the Lagrangian approach where particles are continuously released and tracked throughout the domain. One-way coupling is assumed between carrier fluid and dispersed aerosol phase. Spherical rigid particles with diameters d_p=0.5/1/2/4/6/8/10/15μm and density ρ_p=1000kg/m^3 are released uniformly from the inlet. The particles experience drag, gravity (g_z=-9.81m/s^2), and buoyancy forces, while the interception mechanism is employed for the deposition. For each particle species a total number of 250000 particles are released uniformly across the first half of the simulation time, while they are being tracked for the full simulation time. Details on the numerics of the code employed in the current study can be found in our previous work [32].

The semi-empirical algebraic 1D model in the Mimetikos Preludium$^{\text{TM}}$ software (Emmace Consulting AB, Lund, Sweden) was used as comparison to the DNS and LES computations. The model is a two-stage filter-in series model where fractional mouth deposition (DF_M) is calculated by the semi-mechanistic confined-jet algorithm of DeHaan and Finlay (2004) [5] and fractional throat deposition (DF_T) of the remaining aerosol is calculated by the empirical ICRP model [35]. The total mouth-throat deposition fraction (DF_{MT}) at inhalation is given by:

$$DF_{MT} = DF_M + (1 - DF_M)DF_T. \tag{1}$$

The breath pause and exhalation does not contribute to DF_{MT}. The fractional mouth deposition is computed from the correlation:

$$DF_M = 1 - \frac{1}{1 + 44.5St_U^{1.91}} \tag{2}$$

with the Stokes number

$$St_U = U_{St}\left(\frac{d_{ae}}{10000}\right)^2 \frac{Q}{R^2\pi 18\mu}, \tag{3}$$

where d_{ae} is the aerodynamic particle diameter (μm), Q is the volumetric flow rate (cm^3/s), R is the inner radius of the mouthpiece tube (cm), and μ is the dynamic air viscosity ($dyn.s/cm^2$). The Stokes velocity is computed from the correlation: $U_{St} = 11.8R/(6S_F - R)$ in the range $0.1 < U_{st} < 1$, where S_F is a scale factor $S_F = (50/V_M)^{0.31}$ equal to 1 for a mouth cavity volume (V_M) of $50cm^3$. The fractional throat deposition is computed from the correlation:

$$DF_T = \sqrt{DF_{Tae}^2 + DF_{Tth}^2}, \tag{4}$$

where

$$DF_{Tae} = 1 - \frac{1}{0.00011\left(d_{ae}^2 Q^{0.6} S_F^2 V_T^{-0.2}\right)^{1.4} + 1}, \tag{5}$$

and

$$DF_{Tth} = 1 - e^{-9\sqrt{D(Q\,S_F)^{-1/4}}}, \tag{6}$$

for given tidal volume V_T (cm^3) and particle diffusion coefficient D (cm^2/s).

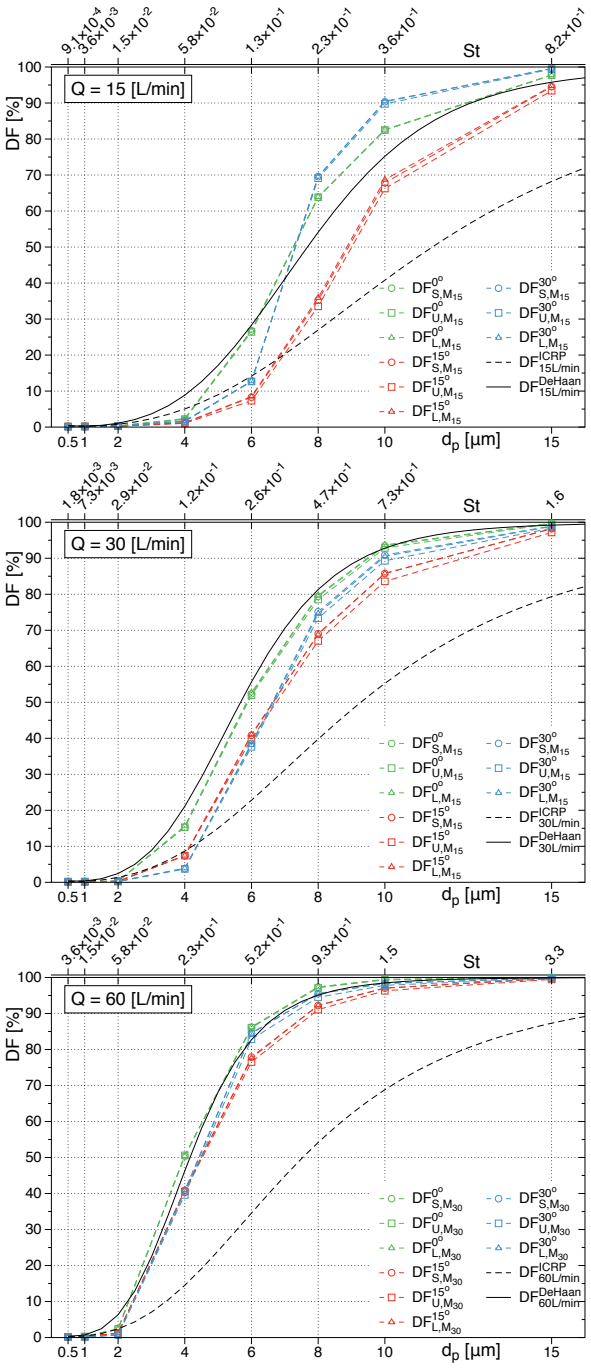

Figure 6: Deposition Fraction (DF) with respect to particle diameter d_p (or Stokes number St=$\frac{\rho_p}{\rho_f}\frac{d_p^2}{R^2}\frac{Re_b}{36}$) for the three flow rates considered: low (top figure), intermediate (middle figure), high (bottom figure). The low and intermediate flow rates are simulated with the M_{15} mesh, while the high flow rate is simulated with the M_{30} mesh. For each flow rate, nine data sets are illustrated corresponding to the different combinations of head position (circles for head-straight, squares for head-up, triangles for head-left) and inhaler orientation (green for 0°-orientation, red for 15°-orientation, blue for 30°-orientation). Each figure involves two additional data sets (in black lines) representing 1D model predictions calculated with the Mimetikos Preludium$^{\text{TM}}$ software. The DeHaan model (continuous line) includes mouth and throat deposition. The ICRP model (dashed line) is throat deposition only

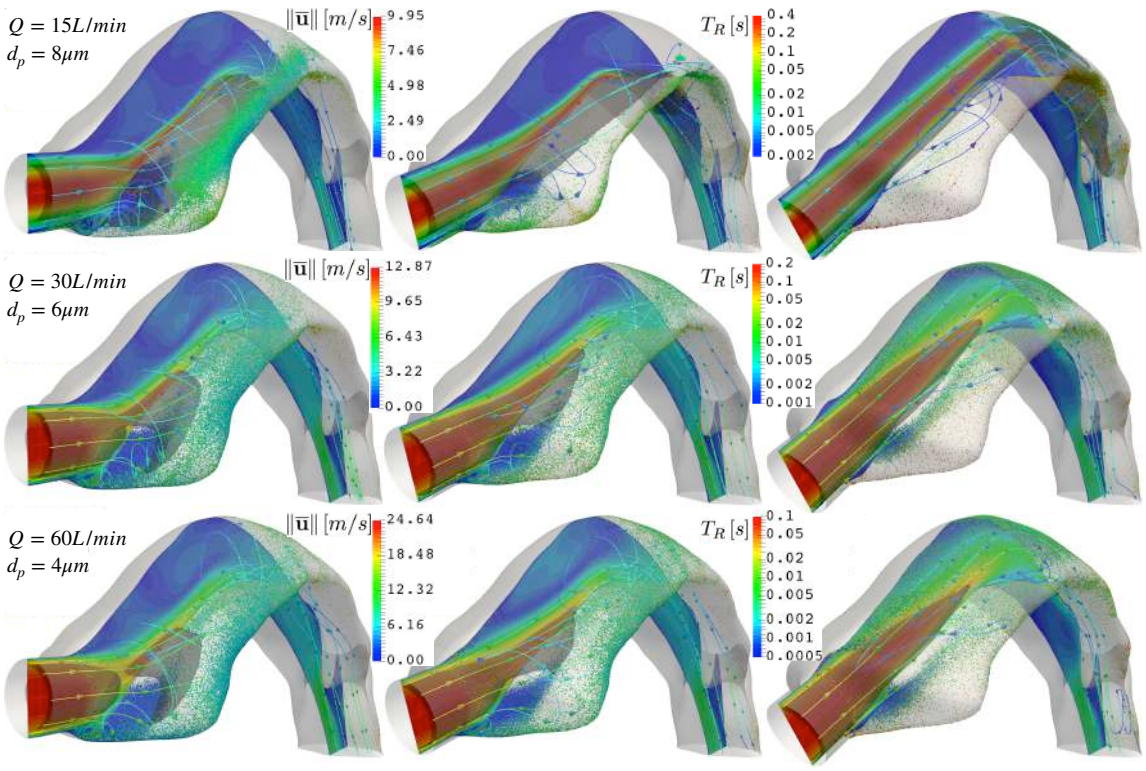

Figure 7: Particle deposition sites in the mouth region induced solely by the head-straight position. Each row of figures represents one of the three inhalation flow rates (low, intermediate, high), while each column of figures represents one of the three inhaler orientations (0°, 15°, 30°). For the low/intermediate/high flow rate only particles with diameter d_p=8/6/4μm are shown, respectively. The particles are coloured by their individual residence time T_R (time interval between release and deposition). The contour plot at the symmetry plane of the geometry is based on the averaged airflow velocity magnitude $\|\overline{\mathbf{u}}\|$. The streamlines are extracted from the averaged air velocity vector field $\overline{\mathbf{u}}$, and coloured by its magnitude $\|\overline{\mathbf{u}}\|$. An iso-surface of $\|\overline{\mathbf{u}}\|$=$u_b$ is illustrated with transparent light black colour. The boundaries of the geometry are visible with transparent grey colour

4 Results

4.1 Deposition Fractions

Figure (6) unveils the dependency of particle Deposition Fraction (DF) on the flow rate, head position, and inhaler orientation. It is evident that the DF is minimally affected by the head position, with the head-up having slightly lower deposition values at all flow rates and inhaler orientations (at least for the larger particles).

Regarding the flow rate, clearly the DF increases with increasing inhalation rate; a direct consequence of the increase of the inertia of particles (i.e. the Stokes number increases analogously with the flow rate). Concerning the inhaler orientation, at the low flow rate the 15°-orientation reduces significantly the DF with respect to the other orientations. For the intermediate and high flow rates, the 30°-orientation is slightly more effective than the 15°-orientation for the smaller particles, but the opposite holds for the larger particles.

It is also noteworthy that the 1D model predictions calculated with the Mimetikos Preludium^{TM} software [36], are in very good agreement with the DF obtained from the 3D simulations of the head-straight 0°-orientation (Figure (6), black continuous line). It was important to include mouth deposition using the confined jet model. DFs using the ICRP model alone were much lower (Figure (6), black dashed line).

4.2 Deposition Sites

Since the head position does not have a profound impact on DF, we proceed with results related exclusively to the head-straight position. For all three inlet orientations, Figure (7) highlights the average flow field patterns in the mouth region and depicts the deposition sites for particles with diameters: d_p=8μm induced by the low flow rate, d_p=6μm induced by the intermediate flow rate, and d_p=4μm induced by the high flow rate. Note that the deposition sites of the high and intermediate flow rates are more dispersed with respect to the ones of the low flow rate, due to turbulent diffusion.

Clearly the orientation of the inlet determines the flow field structures in the mouth region, which in turn affect the particle deposition sites. Flow field patterns closer to the symmetry plane of the domain have a prominent jetal character, generating particle deposition sites at the apex of the *tongue* and/or at the centre of the *soft palate* (i.e. posterior part of the roof of the mouth) via direct inertial impaction. On the contrary, flow field patterns further away from the symmetry plane of the domain have a strong vortical character, leading to particle deposition sites at the *sidewalls* via centrifugal inertial impaction. Evidently, by increasing the orientation angle of the inhaler, the deposition in the area of tongue and sidewalls is reduced while the deposition in the area of palate is increased. Clearly, there is an optimum inhaler orientation angle associated with minimal overall deposition in the mouth area.

4.3 Deposition Regions

To further quantify drug deposition, the mouth-throat geometry is decomposed into smaller segments as shown in Figure (8). The decomposition is carefully selected based on visual inspection of particle deposition sites. Note that the area of the segments is not the same. To increase the sample of particles in each segment, the symmetry of the geometry is exploited. In addition, the regional deposition is expressed as head averaged, justified by the seemingly insignificant effect of head position on the particle deposition.

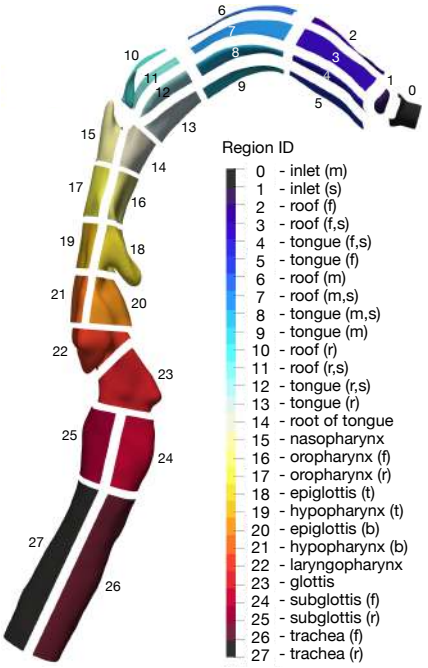

Figure 8: Decomposition of geometry for the assessment of regional deposition. Notation: m = middle, s = side, f = front, r = rear, t = top, b = bottom

Figure (9) highlights the Regional Deposition Fraction (RDF) for one specific particle size for each inhalation flow rate (same with the ones shown in Figure (7)). These are the particle sizes that produce nearly 50% deposition in the whole geometry. Plainly, the first part of Figure (9) (i.e. regions 0-15) quantify the deposition shown in Figure (7). Overall, the regional deposition for the intermediate and high flow rates are similar, while for the low flow rate is slightly different. This is a direct consequence of the different inlet conditions (turbulent vs laminar). Concerning the inhaler orientation, the three main deposition sites for the 0°-orientation are in the regions with IDs: 5,3,4 (front tongue, front-side roof, front-side tongue). This is true for all flow rates. For the 15°-orientation the main deposition sites are the same with the 0°-orientation but only for the intermediate and high flow rates. For the low flow rate the main deposition sites are in the regions with IDs: 5,8,4,13 (front tongue, middle-side tongue, front-side tongue, rear tongue). For the 30°-orientation the three main deposition sites for the intermediate and high flow rate are in the regions with IDs: 6,5,2 (middle roof, front tongue, front roof), while for the low flow rate are in the regions with IDs: 6,8,10 (middle roof, middle-side tongue, rear roof).

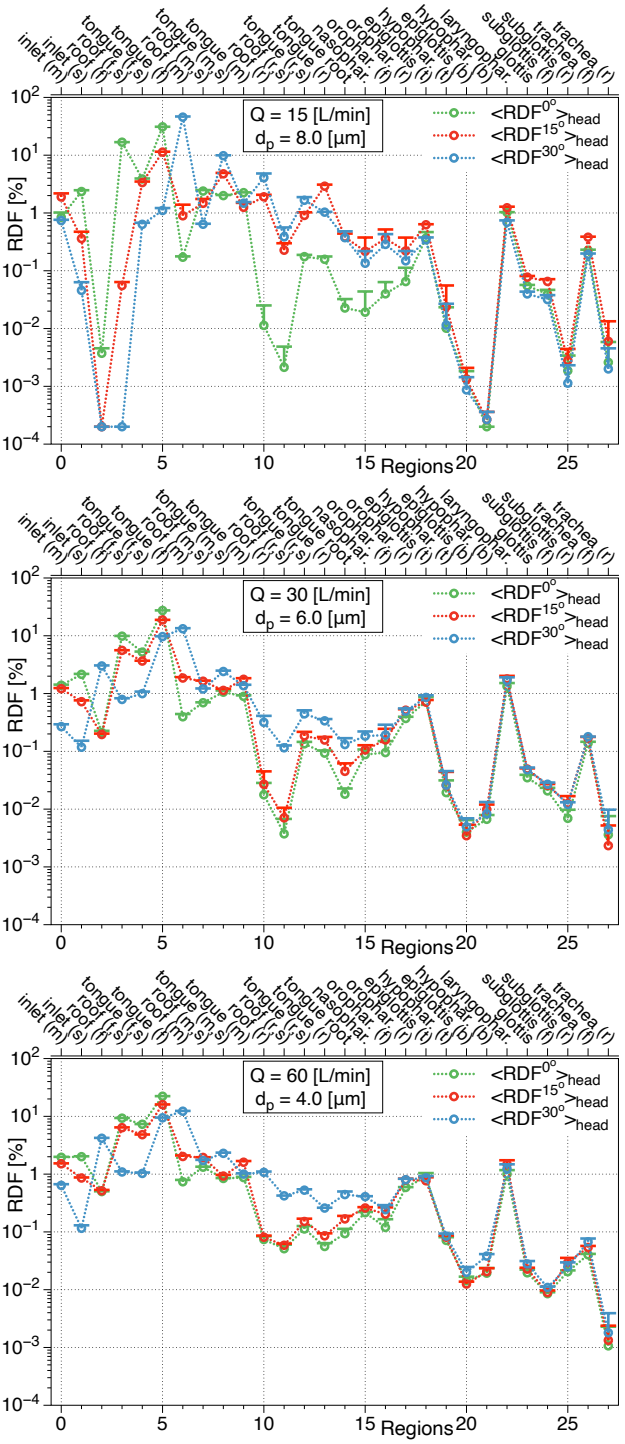

Figure 9: Regional Deposition Fraction (RDF) based on the geometry decomposition of Figure (8). Since the head position does not have a significant impact on the deposition, the average of the three head positions is shown with circles, while the error bars as based on the standard deviation. Since the vertical axis is in log scale, only the positive error bar is shown. Dotted lines are used for visual clarity (they do not have a physical meaning). Each row of figures represents one of the three inhalation flow rates (low, intermediate, high). For the low/intermediate/high flow rate only the results for particles with diameter d_p=8/6/4μm are shown, respectively. The different colours correspond to the different inhaler orientations (green for 0°-orientation, red for 15°-orientation, blue for 30°-orientation)

Interestingly, from region ID 18 and below the regional deposition is similar for all inhaler orientations. This is probably due to the shielding of the flow from upstream effects as a result of passing through two prior successive constrictions (uvula and epiglottis). In this downstream region the most significant deposition ($\sim 1\%$) is in regions with ID 18 and 22 (epiglottis and laryngopharynx).

5 Discussion

The apparent lack of dependence of DF on the head position is a surprising result. To rule out the possibility that this could be linked to the rigid transformation of the mouth area between the three head positions, the simulations should be repeated using actual MRI-based geometries at the corresponding three head positions. For this purpose the MRI scans can be performed in upright body position, thus avoiding the difficulties associated with the supine body position.

In our simulations we have assumed steady inhalation. Typical inhalation profiles from DPIs involve an initial ramp up until the peak inhalation flow rate is reached. Therefore, our results are more representative for DPIs that release the bulk of the dose during the peak flow rate phase rather than in the ramp up phase (capsule vs. blister type DPIs). Furthermore, due to the one-way coupling assumption adopted in our simulations, our results are more relevant to DPIs that release the drug dose under larger inhalation volumes.

6 Conclusions

The current study highlights the effect of flow rate, head position, and inhaler orientation on the particle deposition of various micronised aerosols. Our results indicate that the deposition fraction is practically insensitive of the head position, while the flow rate and the inhaler orientation can significantly affect the deposition in the mouth-throat. For the specific geometry under consideration there is an optimum inhaler orientation angle that minimises the unwanted deposition in the mouth-throat. For the smaller particles the 15^{o}-orientation seems to be slightly more optimum while for the larger particles the 30^{o}-orientation performs better. One can envision inhalers with integrated features that force the users to hold the inhaler at the right orientation angle. This could contribute to a reduction of the side-effects and costs associated with DPI-delivered drugs.

Appendix: Extended Results

In the appendix we collect some additional results for the interested reader. In Figure (10) we highlight the particle deposition sites in the full mouth-throat-trachea geometry (details are the same with Figure (7)). At the symmetry plane of the oral cavity we display the normalised average velocity magnitude in Figure (11), the normalised turbulent kinetic energy in Figure (12), and the normalised "dissipation" of turbulent kinetic energy in Figure (13). In addition, representative turbulent vortical structures are identified by the Q-criterion and illustrated in Figure (14). The results in the appendix are based on the fine meshes.

Acknowledgments

The Prognosis Advanced Diagnostic Center is acknowledged for the MRI scans.

References

[1] J. S. Patton, C. S. Fishburn, and J. G. Weers, "The lungs as a portal of entry for systemic drug delivery," *Proceedings of the American Thoracic Society*, vol. 1, no. 4, pp. 338–344, 2004.

[2] O. S. Usmani, M. F. Biddiscombe, and P. J. Barnes, "Regional lung deposition and bronchodilator response as a function of β2-agonist particle size," *American Journal of Respiratory and Critical Care Medicine*, vol. 172, no. 12, pp. 1497–1504, 2005.

[3] P. Demoly, P. Hagedoorn, A. H. de Boer, and H. W. Frijlink, "The clinical relevance of dry powder inhaler performance for drug delivery," *Respiratory Medicine*, vol. 108, no. 8, pp. 1195–1203, 2014.

[4] A. H. de Boer, D. Gjaltema, and P. Hagedoorn, "Inhalation characteristics and their effects on in vitro drug delivery from dry powder inhalers (Part 2)," *International Journal of Pharmaceutics*, vol. 138, no. 1, pp. 45–56, 1996.

[5] W. H. DeHaan and W. H. Finlay, "Predicting extrathoracic deposition from dry powder inhalers," *Journal of aerosol science*, vol. 35, no. 3, pp. 309–331, 2004.

[6] S. R. B. Behara, P. Longest, D. R. Farkas, and M. Hindle, "Development and comparison of new high-efficiency dry powder inhalers for carrier-free formulations," *Journal of Pharmaceutical Sciences*, vol. 103, no. 2, pp. 465–477, 2014.

[7] J. Xi, J. E. Yuan, M. Yang, X. Si, Y. Zhou, and Y.-S. Cheng, "Parametric study on mouth–throat geometrical factors on deposition of orally inhaled aerosols," *Journal of Aerosol Science*, vol. 99, pp. 94–106, 2016.

[8] J. Xi, X. A. Si, H. Dong, and H. Zhong, "Effects of glottis motion on airflow and energy expenditure in a human upper airway model," *European Journal of Mechanics-B/Fluids*, vol. 72, pp. 23–37, 2018.

[9] J. Xi and T. Yang, "Variability in oropharyngeal airflow and aerosol deposition due to changing tongue positions," *Journal of Drug Delivery Science and Technology*, vol. 49, pp. 674–682, 2019.

[10] P. G. Koullapis, L. Nicolaou, and S. C. Kassinos, "In silico assessment of mouth-throat effects on regional deposition in the upper tracheobronchial airways," *Journal of Aerosol Science*, vol. 117, pp. 164–188, 2018.

[11] Y. Feng, J. Zhao, C. Kleinstreuer, Q. Wang, J. Wang, D. H. Wu, and J. Lin, "An in silico inter-subject variability study of extra-thoracic morphology effects on inhaled particle transport and deposition," *Journal of Aerosol Science*, vol. 123, pp. 185–207, 2018.

[12] L. Golshahi, M. L. Noga, and W. H. Finlay, "Deposition of inhaled micrometer-sized particles in oropharyngeal airway replicas of children at constant flow

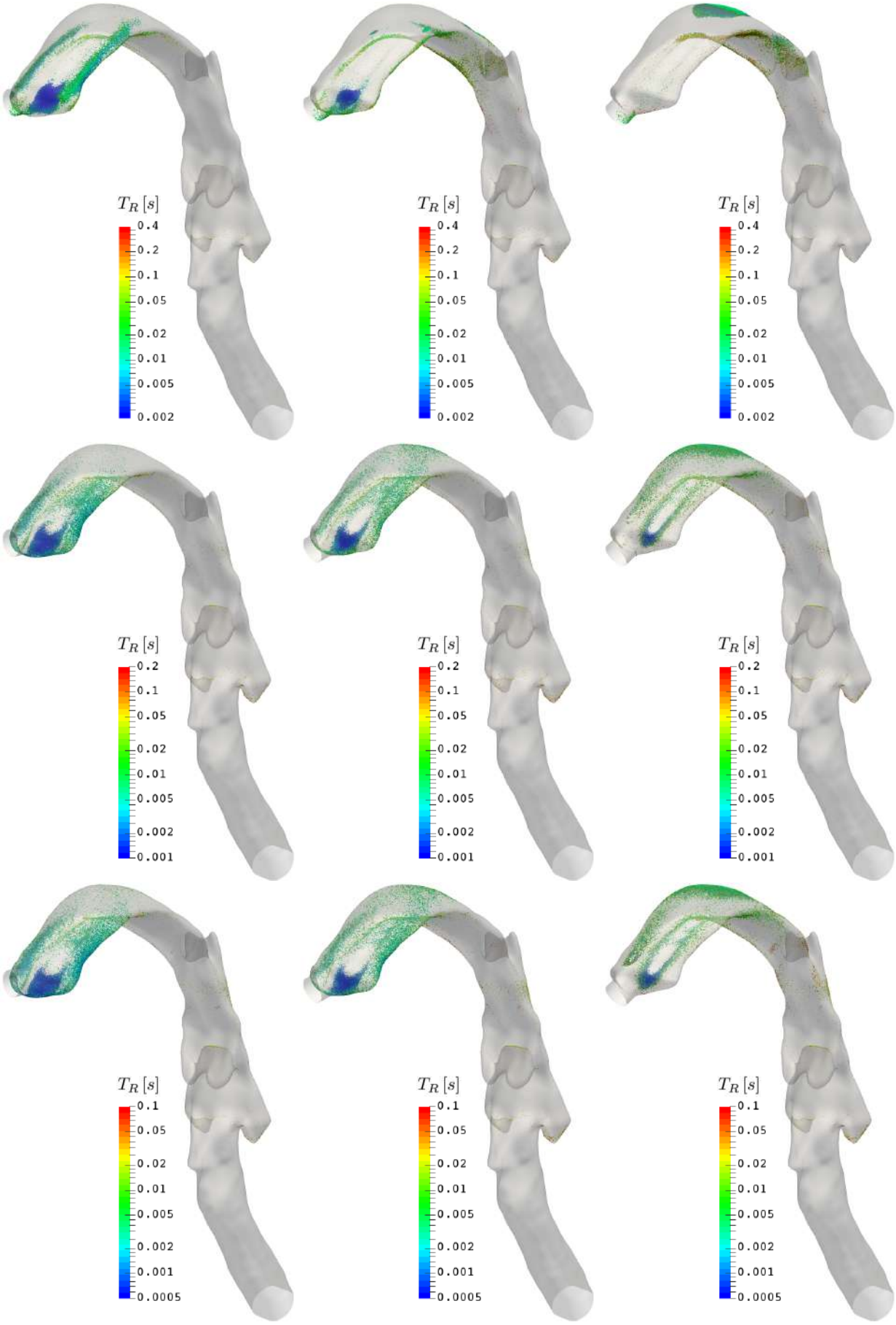

Figure 10: Particle deposition sites in the mouth-throat region. For details see Figure (7)

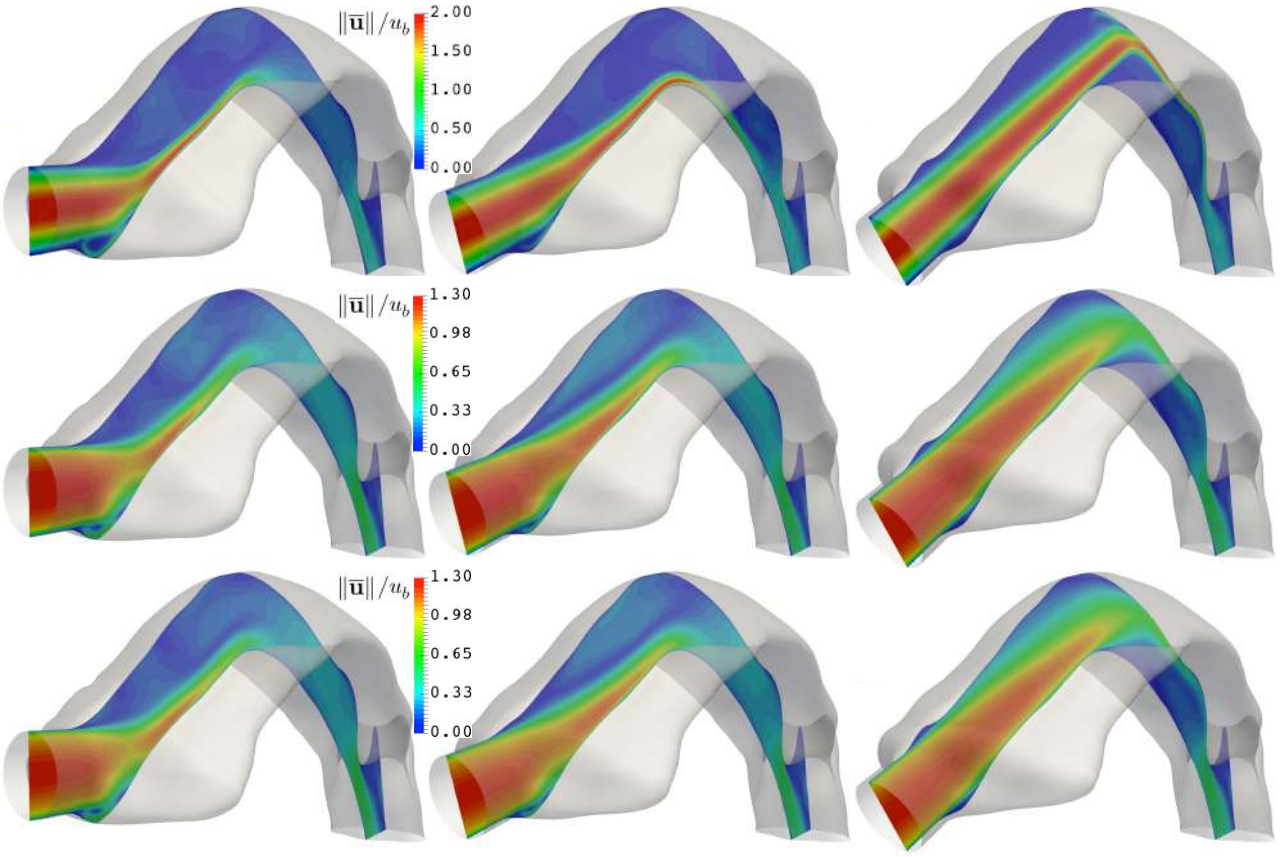

Figure 11: Contour plot of the normalised averaged velocity magnitude $\|\overline{\mathbf{u}}\|/u_b$ at the symmetry plane of the geometry (solely for the head-straight position). Each row of figures represents one of the three inhalation flow rates (low, intermediate, high), while each column of figures represents one of the three inhaler orientations (0°, 15°, 30°). The boundaries of the geometry are visible with transparent grey colour

rates," *Journal of Aerosol Science*, vol. 49, pp. 21–31, 2012.

[13] J. Choi, M. H. Tawhai, E. A. Hoffman, and C.-L. Lin, "On intra-and intersubject variabilities of airflow in the human lungs," *Physics of Fluids*, vol. 21, no. 10, p. 101901, 2009.

[14] A. F. Heenan, W. H. Finlay, B. Grgic, A. Pollard, and P. K. P. Burnell, "An investigation of the relationship between the flow field and regional deposition in realistic extra-thoracic airways," *Journal of aerosol science*, vol. 35, no. 8, pp. 1013–1023, 2004.

[15] W. H. DeHaan and W. H. Finlay, "In vitro monodisperse aerosol deposition in a mouth and throat with six different inhalation devices," *Journal of Aerosol Medicine*, vol. 14, no. 3, pp. 361–367, 2001.

[16] B. Grgic, W. H. Finlay, and A. F. Heenan, "Regional aerosol deposition and flow measurements in an idealized mouth and throat," *Journal of Aerosol Science*, vol. 35, no. 1, pp. 21–32, 2004.

[17] B. Grgic, W. H. Finlay, P. K. P. Burnell, and A. F. Heenan, "In vitro intersubject and intrasubject deposition measurements in realistic mouth–throat geometries," *Journal of Aerosol Science*, vol. 35, no. 8, pp. 1025–1040, 2004.

[18] L. Nicolaou and T. A. Zaki, "Direct numerical simulations of flow in realistic mouth–throat geometries," *Journal of Aerosol Science*, vol. 57, pp. 71–87, 2013.

[19] Y. Zhang, K. Gilbertson, and W. H. Finlay, "In vivo–in vitro comparison of deposition in three mouth–throat models with Qvar® and Turbuhaler® inhalers," *Journal of aerosol medicine*, vol. 20, no. 3, pp. 227–235, 2007.

[20] T.-C. Lin, P. N. Breysse, B. L. Laube, and D. L. Swift, "Mouthpiece diameter affects deposition efficiency in cast models of the human oral airways," *Journal of Aerosol Medicine*, vol. 14, no. 3, pp. 335–341, 2001.

[21] Y. Zhou, J. Sun, and Y.-S. Cheng, "Comparison of deposition in the USP and physical mouth–throat models with solid and liquid particles," *Journal of aerosol medicine and pulmonary drug delivery*, vol. 24, no. 6, pp. 277–284, 2011.

[22] D. W. McRobbie, S. Pritchard, and R. A. Quest, "Studies of the human oropharyngeal airspaces using magnetic resonance imaging. I. Validation of a three-dimensional MRI method for producing ex vivo virtual and physical casts of the oropharyngeal airways during inspiration," *Journal of aerosol medicine*, vol. 16, no. 4, pp. 401–415, 2003.

[23] S. E. Pritchard and D. W. McRobbie, "Studies of the human oropharyngeal airspaces using magnetic resonance imaging. II. The use of three-dimensional gated MRI to determine the influence of mouthpiece diameter and resistance of inhalation devices on the oropharyngeal airspace geometry," *Journal of Aerosol Medicine*, vol. 17, no. 4, pp. 310–324, 2004.

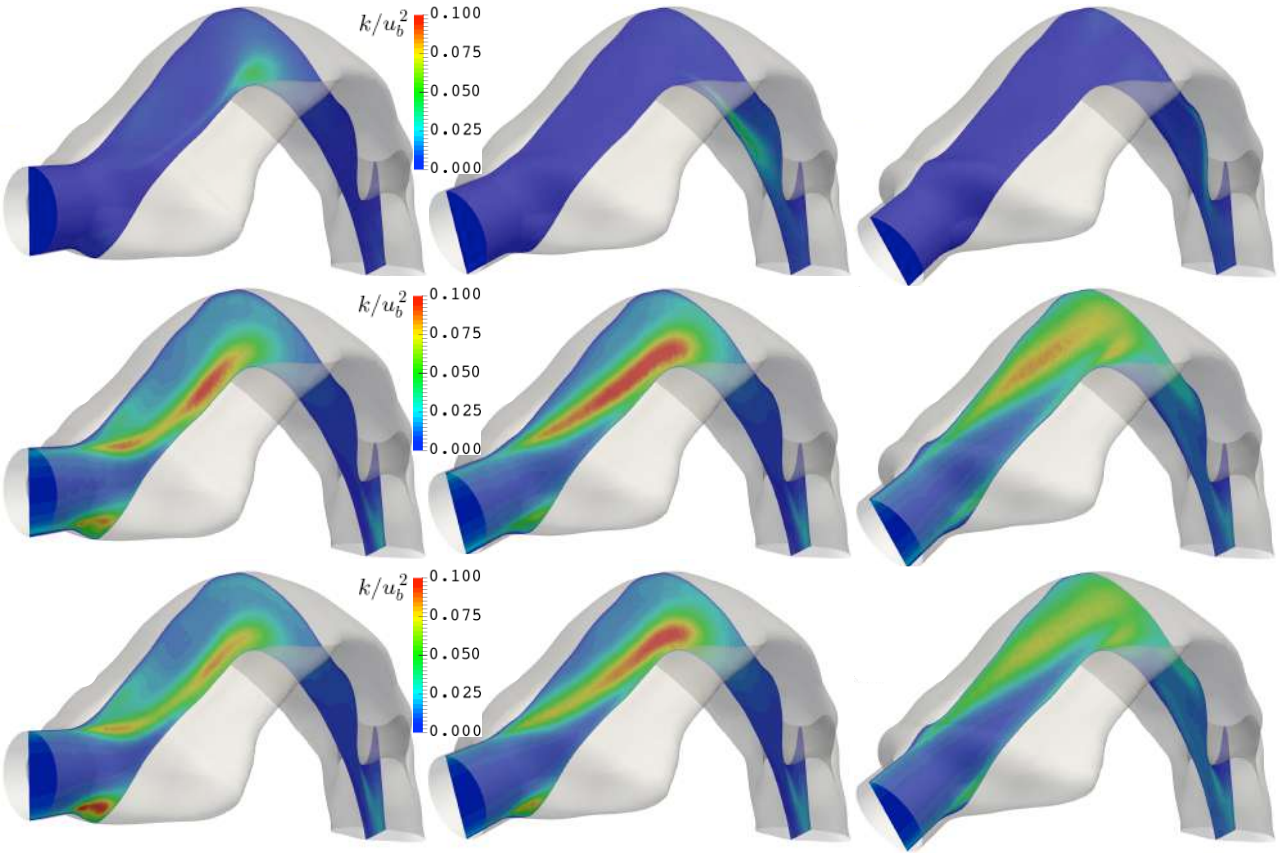

Figure 12: Same as in Figure (11), but for the normalised turbulent kinetic energy k/u_b^2

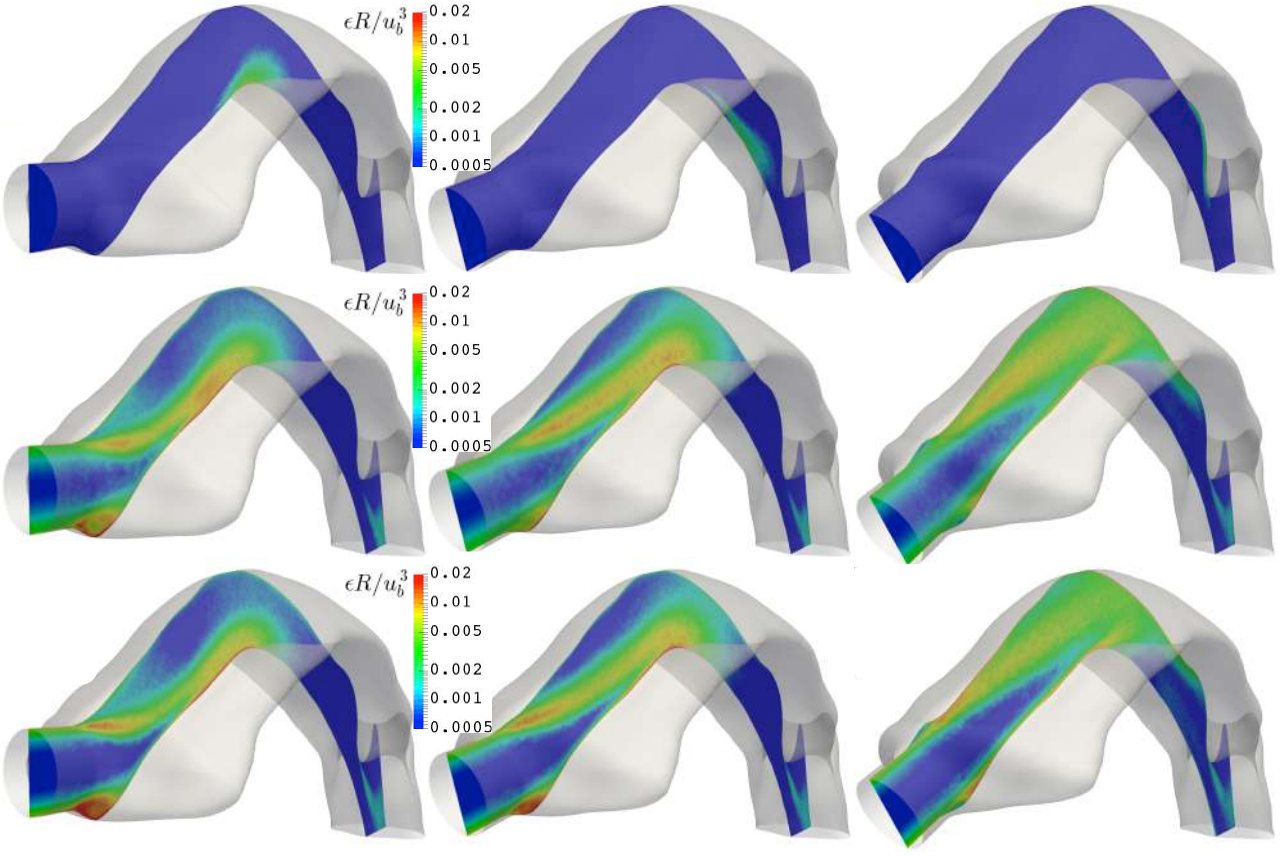

Figure 13: Same as in Figure (11), but for the normalised "dissipation" of turbulent kinetic energy $\epsilon R/u_b^3$ (where $\epsilon = (\nu+\nu_\tau)\omega'^2$, ν is the viscosity, ν_τ is the turbulent sub-grid scale viscosity, ω' is the fluctuating vorticity magnitude)

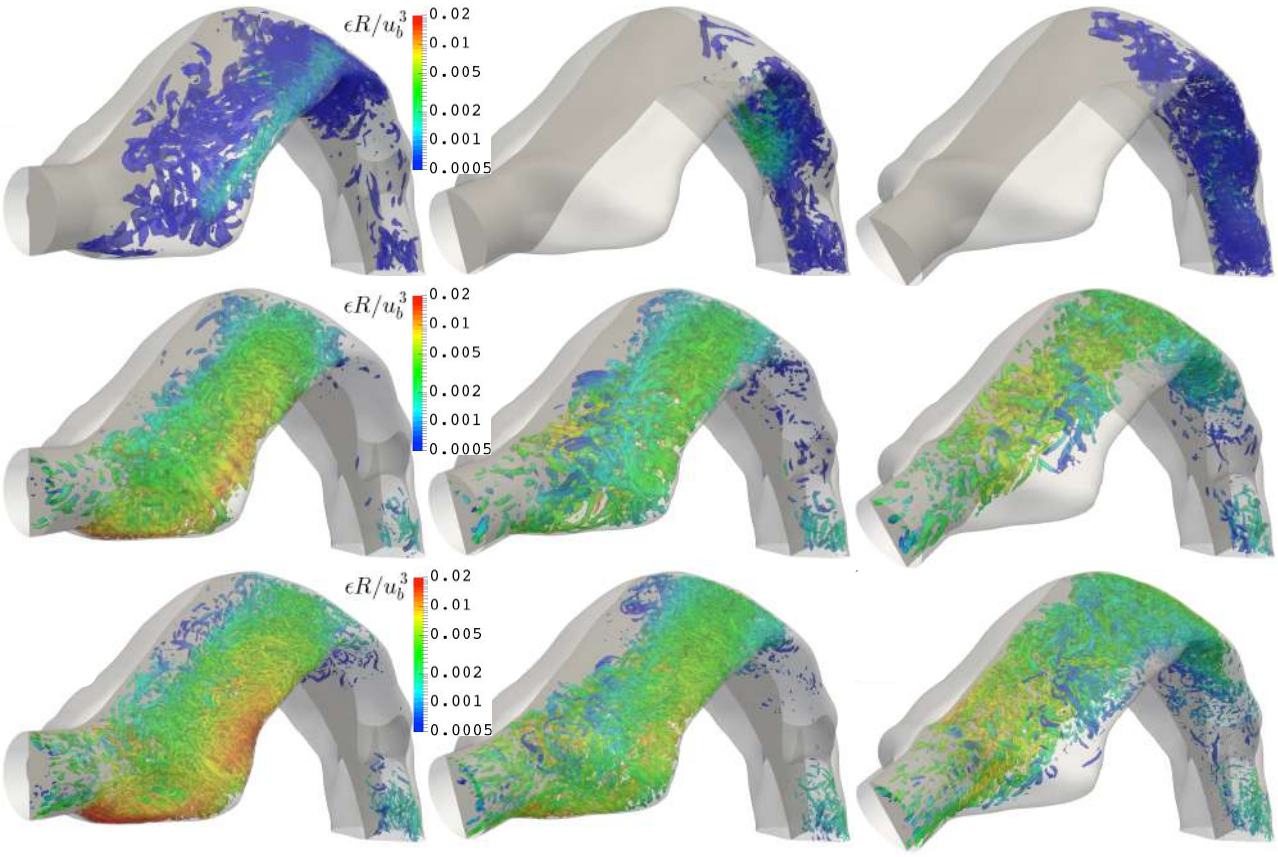

Figure 14: Same as in Figure (11), but here we extract the turbulent vortical structures identified by the $Q^{u'}$-criterion (based on the fluctuating velocity field). The colouring is based on the local normalised "dissipation" of turbulent kinetic energy $\epsilon R/u_b^3$

[24] D. W. McRobbie and S. E. Pritchard, "Studies of the human oropharyngeal airspaces using magnetic resonance imaging. III. The effects of device resistance with forced maneuver and tidal breathing on upper airway geometry," *Journal of aerosol medicine*, vol. 18, no. 3, pp. 325–336, 2005.

[25] P. K. P. Burnell, L. Asking, L. Borgström, S. C. Nichols, B. Olsson, D. Prime, and I. Shrubb, "Studies of the human oropharyngeal airspaces using magnetic resonance imaging IVâĂŤthe oropharyngeal retention effect for four inhalation delivery systems," *Journal of Aerosol Medicine*, vol. 20, no. 3, pp. 269–281, 2007.

[26] R. R. Delvadia, P. W. Longest, and P. R. Byron, "In vitro tests for aerosol deposition. I: Scaling a physical model of the upper airways to predict drug deposition variation in normal humans," *Journal of aerosol medicine and pulmonary drug delivery*, vol. 25, no. 1, pp. 32–40, 2012.

[27] R. Delvadia, M. Hindle, P. W. Longest, and P. R. Byron, "In vitro tests for aerosol deposition II: IVIVCs for different dry powder inhalers in normal adults," *Journal of aerosol medicine and pulmonary drug delivery*, vol. 26, no. 3, pp. 138–144, 2013.

[28] R. R. Delvadia, P. W. Longest, M. Hindle, and P. R. Byron, "In vitro tests for aerosol deposition. III: Effect of inhaler insertion angle on aerosol deposition," *Journal of aerosol medicine and pulmonary drug delivery*, vol. 26, no. 3, pp. 145–156, 2013.

[29] R. R. Delvadia, X. Wei, P. W. Longest, J. Venitz, and P. R. Byron, "In vitro tests for aerosol deposition. IV: Simulating variations in human breath profiles for realistic DPI testing," *Journal of aerosol medicine and pulmonary drug delivery*, vol. 29, no. 2, pp. 196–206, 2016.

[30] X. Wei, M. Hindle, R. R. Delvadia, and P. R. Byron, "In vitro tests for aerosol deposition. V: Using realistic testing to estimate variations in aerosol properties at the trachea," *Journal of aerosol medicine and pulmonary drug delivery*, vol. 30, no. 5, pp. 339–348, 2017.

[31] X. Wei, M. Hindle, A. Kaviratna, B. K. Huynh, R. R. Delvadia, D. Sandell, and P. R. Byron, "In vitro tests for aerosol deposition. VI: realistic testing with different mouth–throat models and in vitro-in vivo correlations for a dry powder inhaler, metered dose inhaler, and soft mist inhaler," *Journal of aerosol medicine and pulmonary drug delivery*, vol. 31, no. 6, pp. 358–371, 2018.

[32] F. S. Stylianou, J. Sznitman, and S. C. Kassinos, "Direct numerical simulation of particle laden flow in a human airway bifurcation model," *International Journal of Heat and Fluid Flow*, vol. 61, pp. 677–710, 2016.

[33] P. Koullapis, S. C. Kassinos, J. Muela, C. Perez-Segarra, J. Rigola, O. Lehmkuhl, Y. Cui, M. Sommerfeld, J. Elcner, M. Jicha, I. Saveljic, N. Filipovic, F. Lizal, and L. Nicolaou, "Regional aerosol deposition in the human airways: The SimInhale bench-

mark case and a critical assessment of in silico methods," *European Journal of Pharmaceutical Sciences*, vol. 113, pp. 77–94, 2018.

[34] F. S. Stylianou, R. Pecnik, and S. C. Kassinos, "Analyzing a turbulent pipe flow via the one-point structure tensors: Vorticity crawlers and streak shadows," *Computers & Fluids*, vol. 140, pp. 450–477, 2016.

[35] ICRP, "Human Respiratory Tract Model for Radiological Protection, Publication 66," *Annals of the ICRP*, vol. 24, pp. 1–482, 1994.

[36] B. Olsson and P. Bäckman, "Mimetikos Preludium^{TM}: A New Pharma-friendly Aerosol Drug Deposition Calculator," *Respiratory Drug Delivery*, vol. 1, pp. 103–112, 2018.

The Fate of Inhaled Hygroscopic Particles Inside the Human Airways

F.S. Stylianou[1], P.G. Koullapis[1], and S.C. Kassinos[1,2]

[1] *Computational Sciences Laboratory (UCY-CompSci), Nireas-International Water Research Centre, University of Cyprus*
[2] *Department of Mechanical & Manufacturing Engineering, University of Cyprus*

Abstract

In this study, we present results from our ongoing efforts on simulating the transport, growth, and deposition of inhaled hygroscopic particles inside the human airways. We perform Large Eddy Simulations (LES) of turbulent airflow and particle transport (including heat transfer, water vapour transfer, and aerosol hygroscopic growth effects) in a human airway geometry. We evaluate the delivery efficiency of various initially dry particle sizes, with different drug-excipient ratios, under typical inhalation flowrates. With appropriate selection of the initial size of the particles and the drug-excipient ratio, it is possible to achieve optimum drug delivery at targeted areas of the airways, by harnessing the innate high humidity environment of the lungs.

1 Introduction

The human mouth-throat plays a key role in the administration of inhaled medicines. It is an area of intense filtration, where a substantial fraction of the released drug dose is deposited via inertial impaction and thus never reaches the conducting and respiratory airways. Such high extrathoracic losses are associated with: increased side effects, reduced drug effectiveness, and increased medication cost. In addition, next generation inhaled medications (such as antibiotics, vaccines, and chemotherapy), require precise targeting and dosing within the airways to be clinically acceptable, effective, and safe. Undeniably, improving the delivery efficiency of inhaled medications is of utmost importance.

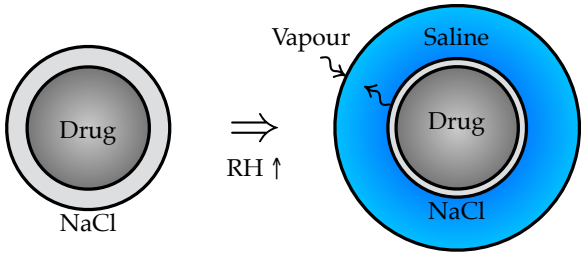

Figure 1: Initially dry particle and subsequent hygroscopic growth when conditions are favourable (naively when RH is high). Curvy arrows represent water vapour condensation and NaCl excipient dissolution

A naive approach to eliminate mouth-throat deposition is by reducing the size of inhaled drug particles below the typical Fine Particle Dose ($d = 1-5\mu m$). Unfortunately, this approach is also associated with poor deep lung retention. A more sophisticated approach dictates the need for controlled aerosol growth. In this direction, Longest and Hindle proposed the Excipient Enhanced Growth (EEG) method [1]. In this approach, initially submicrometer drug particles enhanced with hygroscopic excipients (to enable hygroscopic growth effects) are inhaled under the influence of the high humidity lung environment. A schematic of this process is shown in Figure (1). As the particles move from the extrathoracic to the intrathoracic lung region, their sizes increase into the micrometer range, becoming ideal for deep lung retention (e.g. Figure (2)). With appropriate selection of the initial size of the particles and the drug-excipient ratio, it is possible to achieve optimum drug delivery at targeted areas of the airways.

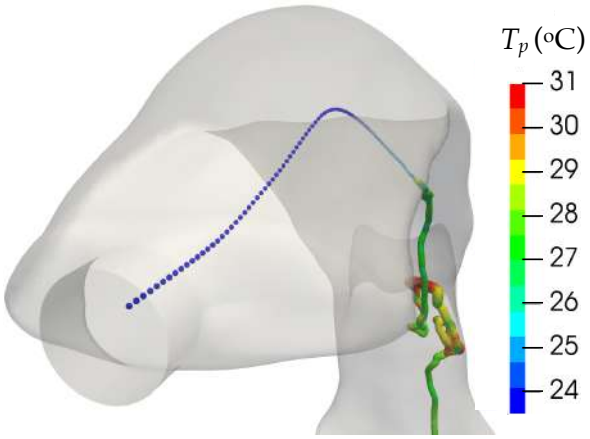

Figure 2: Example of particle trajectory in the mouth-throat region coloured by its temperature (T_p). The size of the particle is exaggerated for clarity, but the relative hygroscopic growth changes are retained

In this work, high-fidelity numerical simulations are used to determine the delivery efficiency of various particle sizes, with different drug-excipient ratios, under typical inhalation flowrates. The simulations can reveal with confidence which combinations of the accounted conditions are more effective on reducing the unwanted mouth-throat deposition.

2 Methods and Computational Details

Instead of employing the RANS modelling approach of Longest et al. [2, 3], the more accurate DNS/LES methods are used in this work. The fate of hygroscopic aerosols is sensitive to airflow fluctuations, and the use of DNS/LES is important for capturing the underlying turbulence physics. Furthermore, the evolution of the turbulent airflow and particles is solved at the same time

(i.e. not at a post-processing level), where the airflow affects directly the particle sizes and paths. To achieve this type of simulations we have combined the numerical methodologies of Stylianou et al. [4, 5] for airflow and particle transport, Wu et al. [6] for heat and water vapour transfer, and Longest et al. [7] for particle growth.

Partial differential equations for water vapour mass fraction Y_v and air mixture temperature T_f, velocity $\boldsymbol{u}_f$, and pressure P_f are solved numerically. The Boussinesq approximation is used to account for density variations on the airflow, caused by temperature and water vapour gradients. The airflow transport equations are solved at the grid nodes based on the finite volume method.

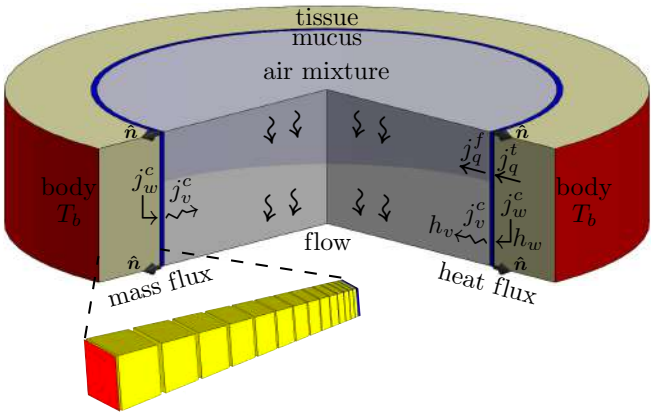

Figure 3: Schematic of airway cross section showing the mass and heat flux balance between air mixture and tissue. Tissue grid layers are visible. Mucus is modelled with zero thickness. Evaporated water is assumed to be continuously restored from mucus secreting goblet cells. Symbol definitions: Convective mass flux j^c, conduction heat flux j_q, enthalpy h, tissue t, fluid (air mixture) f, body b, water w, vapour v

Pennes' bioheat transfer equation is solved in the airway tissue, to provide realistic airway surface field temperature boundary conditions for the airflow. The bioheat equation is solved only in the wall normal direction (1D) as in Wu et al. [6], but we adopt curvilinear coordinates to account for local surface curvature effects. An initial coupled airflow-tissue simulation was performed at normal breathing, resulting in a non-uniform surface airway wall temperature field, which was set for subsequent drug administration airflow simulations. This simplification relies on the two orders of magnitude difference between the thermal diffusivity of air mixture and tissue (i.e. temperature temporal changes of tissue are slower compare to air). In our initial simulation we have adopted an airway tissue thickness of $L_t = 2.5$mm with external surface temperature at body core conditions $T_b = 37$°C. The effect of water evaporation from the airway surface liquid is also taken into account, as shown in Figure (3). The internal airway surface remains always wet with fixed relative humidity at $RH_w = 99.5\%$. Figure (4) shows the computed airway temperature and air mixture velocity at the airway wall as a result of water evaporation from mucus lining fluid.

For the purposes of this study, the usage of an anatomically correct airway geometry is essential. To generate one, we combine a mouth-throat model (extracted from a head-neck MRI scan) with a tracheobronchial tree model (extracted from a chest CT scan). The medical images are from two related subjects (son & father) and thus an overlapping approach of the spinal columns is employed for the fusion of the two models. At the region of lips an inhaler mouthpiece is approximated, leading to a tube airway inlet with radius $R_{in} = 4$mm. At this location room conditions ($T_{in} = 23.5$°C, $RH_{in} = 55\%$) are specified. Steady inhalation conditions are adopted for three flowrates ($Q_{in} = 15/30/60$ L/min) with bulk Reynolds numbers $Re_{in} \approx 2454/4908/9816$. For the low/intermediate/high flowrates, laminar/turbulent/turbulent inlet conditions are imposed using parabolic/recycling/recycling boundary conditions. At the bronchial outlets, the convective outlet condition is prescribed with the lobar ventilation distributed as: RUL-15%, RML-8%, RLL-30%, LUL-18%, and LLL-29% (consistent with [8]).

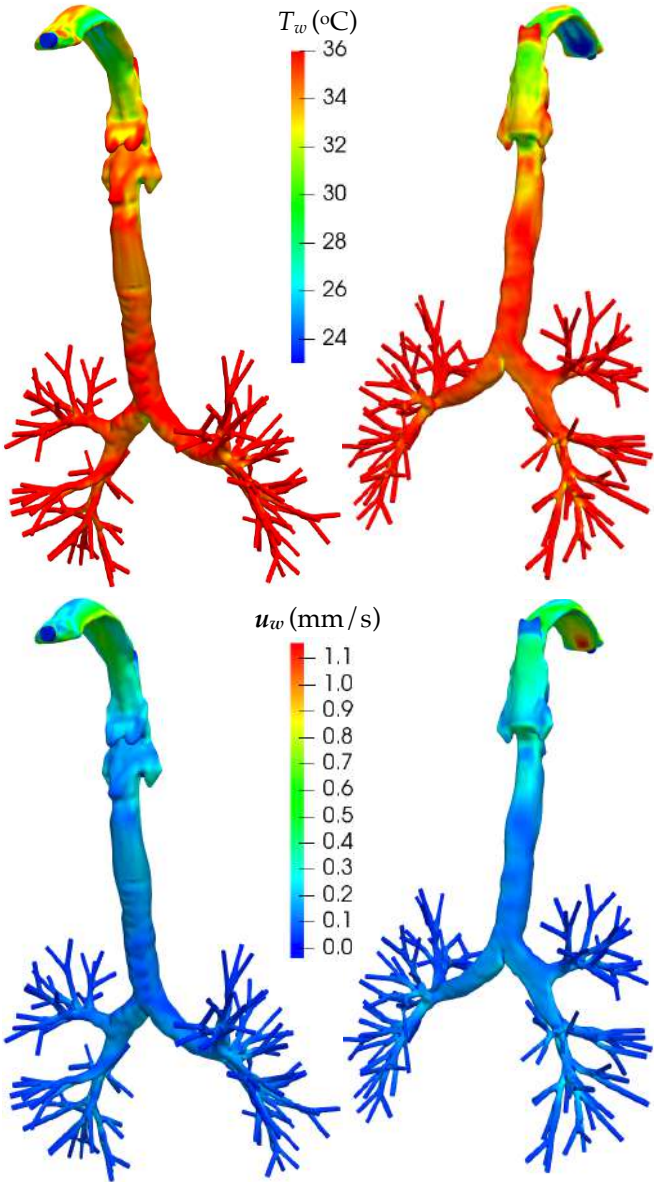

Figure 4: Temperature T_w (top) and air mixture normal velocity u_w (bottom) at the airway wall. Two airway viewpoints are shown for each field (front and back). Upper airway cooling and water evaporation from mucus are evident

To simulate the low/intermediate/high flowrates we have used high quality unstructured grids with 13.5/26.5/45.5 million elements and 5/6/7 near wall prismatic layers; the first layer height being at

25/12.5/6.25μm. Local grid refinement is used in areas of expected intense phenomena. Grid resolutions in the oral cavity are visible in Figure (5). The DNS/LES/LES method was employed to simulate the low/intermediate/high flowrates, using a time step of 10/10/5μs. The Dynamic Smagorinsky model was used with the LES method. For all flowrates, 1.5 million time steps were simulated.

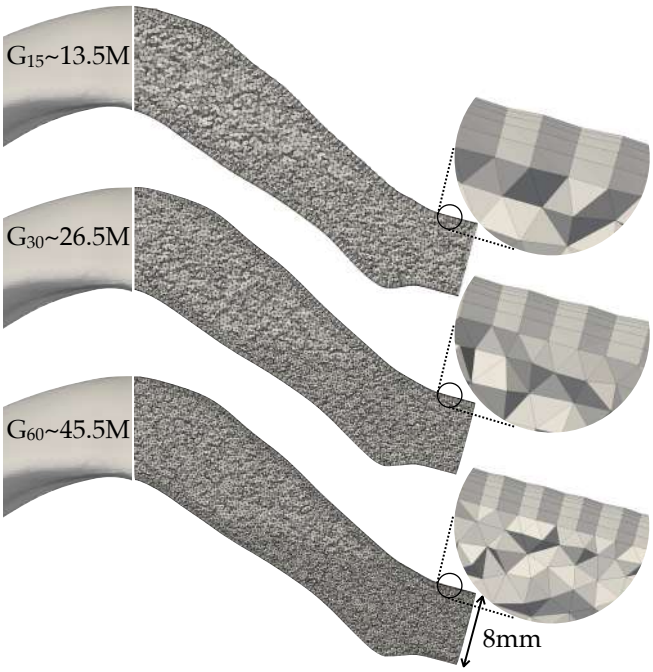

Figure 5: Grid resolutions in the oral cavity for the three meshes used in this study. The low/intermediate/high flowrate is simulated with $G_{15}/G_{30}/G_{60}$ grid

Coupled ordinary differential equations for the diameter d_p, temperature T_p, velocity $\boldsymbol{u}_p$, and position $\boldsymbol{x}_p$ of all injected particles are solved numerically. Due to the wide spectrum of particle sizes simulated and their possible size change, we had to ensure that the numerical schemes used were robust at all times. Furthermore, to allow the usage of relatively large particle time steps (i.e. in the order of airflow time steps, $dt_p \lesssim dt_f$), implicit numerical schemes had to be adopted. For our simulations the Lagrangian particle equations are solved using an implicit TR-BDF2 variant method [9], which is second order accurate, A-stable, and L-stable. When the Brownian force is important the Midpoint discretisation can lead to oscillating particle velocities (see Figure (6)) and possibly unstable trajectories for particle sizes in the nano range $d_p < 10nm$. In addition, an Explicit Segregated solution approach for the droplet diameter and temperature was not stable for submicron sizes $d_p \ll 0.5\mu m$. As can be seen from Figure (7) the temperature of the particle becomes unstable once the RH conditions are favourable for particle size changes (in this case when $RH > 76\%$). On the other hand the second order Backward Difference discretisation with an intermediate Trapezoidal sub-step (TR-BDF2) produced stable trajectories. The Newton-Raphson approach was used to solve the Implicit Coupled discrete system of equations, which was found ideal for obtaining numerically stable particle size and temperature changes under all conditions of interest.

Particles are released at the mouthpiece inlet, acquiring the airflow properties. They are initialised as dry,

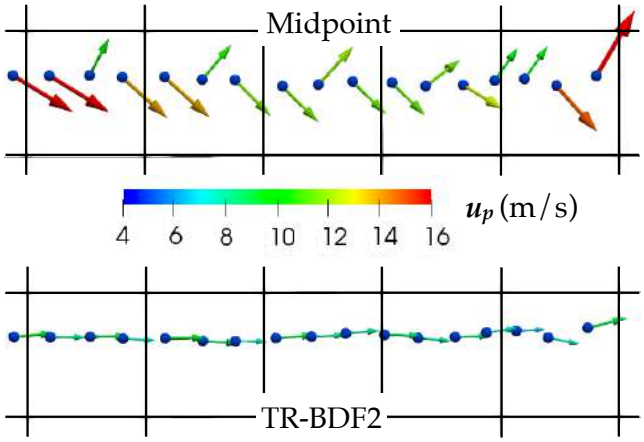

Figure 6: Examples of unstable (top) and stable (bottom) particle velocities when the Brownian force is important. The unstable results are from the Midpoint discretisation, while the stable results are based on the TR-BDF2 discretisation. Under midpoint scheme the computed particle velocity vector oscillates. Note that when the particle crosses a grid face there is a hidden intermediate sub-step

but water vapour condensation on the particles is induced by the hygroscopic property of their excipient, which directly affects their size. In our simulations we have used five different blends of Budesonide-NaCl as our drug-excipient composites. For each particle size and for each different blend, 125000 particles are released uniformly during the first half of each simulation. During the remaining half of the simulations the fate of all particles is determined. An evaporation/condensation model was used, which employs rapid mixing conditions within the particle such that its temperature and concentration vary only temporally. In light of the large particle-to-air density ratio $(\rho_p/\rho_f) \approx 10^3$, only the important forces acting on the aerosols have been considered (Drag, Gravity-Buoyancy, Shear-Lift, and Brownian). In the following section we report results under one-way coupling between airflow and particles, while simulations with two-way coupling are ongoing.

3 Results

Here we present results from our simulations on low, intermediate, and high inhalation flowrates. Figure (8) illustrates the instantaneous airflow velocity, temperature, and relative humidity at the two main cross sections of the airway. In the subfigures of the leftmost column, we can identify the impingement of the inhaled airflow on the tongue, as well as the relatively high velocities in the mouth-throat region. These effects along with the complex and curved shape of this area are associated with high deposition fractions for the larger particles (shown later). As expected, the turbulent airflow persists further down the trachea with increasing inhalation flowrate. The subfigures of the remaining columns highlight the warming and humidification processes of the inhaled airstream. Both processes continue deeper into the airways with increasing inhalation flowrate. As the airflow moves to the more distal airway generations (not shown here) it slows down, becomes fully saturated, and reaches body core temperature.

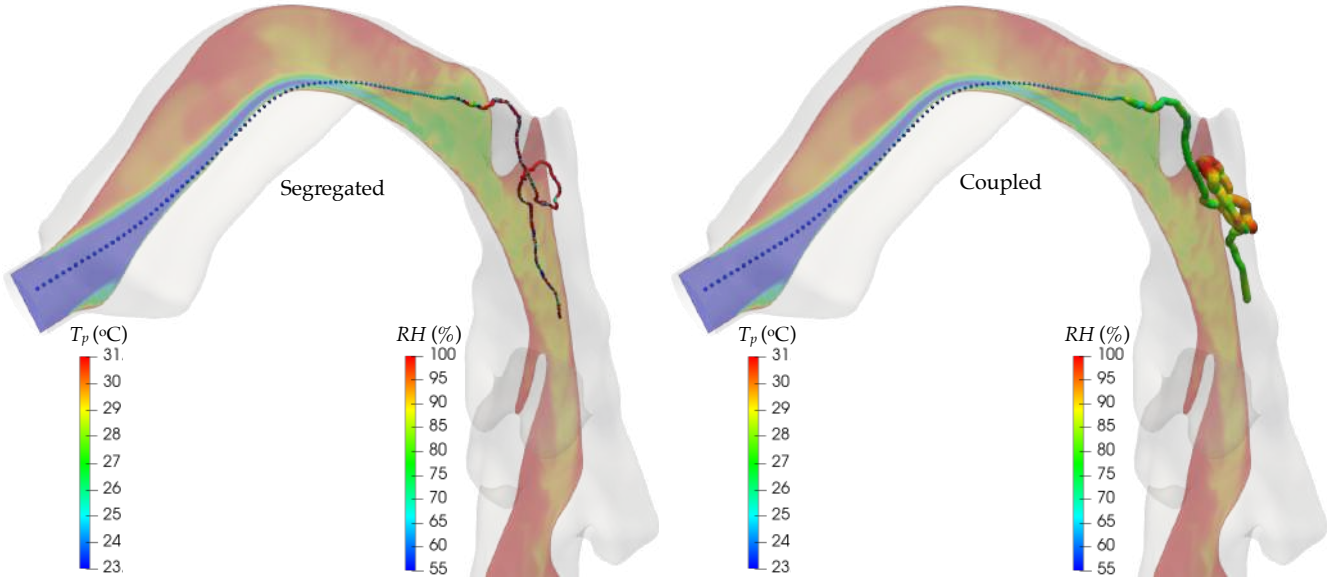

Figure 7: Examples of unstable (left) and stable (right) droplet diameter and temperature changes. The unstable results are from an Explicit Segregated solution approach, while the stable results are based on an Implicit Coupled solution approach involving Newton-Raphson method with Backtracking

Moving on to the particulate phase, Figure (9), Figure (10), and Figure (11) display results for five particle composites that differ in their drug-excipient ratio (by mass). The top/middle/bottom subfigures are based on the low/intermediate/high inhalation flowrate. We focus our subsequent discussion on the high flowrate results, while the analogy to the low and intermediate flowrates can be inferred.

Figure (9) shows the average size of the particles that escape the bronchial outlets (and thus are available for deep lung deposition) as a function of their initial dry size. The error bars are based on the standard deviation formula. Clearly, particle composites with higher excipient ratio end up larger in size. What one needs to keep in mind here is the following key idea: particles must start small to avoid filtering in the mouth-throat and subsequently grow to foster deep lung retention. For example, to achieve a final size of 4μm (ideal for deep lung deposition), particles with 50%-50% drug-excipient composite can be initiated at 1.8μm dry size, in contrast to the pure drug case in which particles must be initiated at the same size.

We proceed to Figure (10) revealing the aerosol deposition fraction as a function of the initial dry size of the inhaled particles. Plainly, for same initial particle sizes, composites with larger excipient ratios lead to higher deposition fractions, in accordance with the higher growth factors and increased particle inertia. However, continuing our discussion from Figure (9), pure drug particles initiated at 4μm have 65% deposition fraction in the simulated airways, leaving only 35% available for deep lung deposition. Contrariwise, 50%-50% drug-excipient particle composites initiated at 1.8μm have only 14% deposition fraction in the simulated airways, leaving 86% available for deep lung deposition. Clearly the drug-excipient composites can outperform the pure drug particles in deep lung administration. Of course, more smaller drug-excipient particles are needed to deliver the same dose as the larger pure drug particles. However, the total drug dose used for the composite particles will be less since only 14% is lost in the large conducting airways.

Figure (11) shows the mean final size of the particles that deposit on the simulated airways as a function of their initial dry size. The error bars are again based on the standard deviation formula. Continuing the previous discussion, the 50%-50% drug-excipient particle composites initiated at 1.8μm have a mean final diameter of 3.0μm at the instance on deposition. Pure drug particles at the same size have a much higher deposition fraction, which again implies the effectiveness of composite particles.

To complete our discussion, we shortly compare the results of the three flowrates. The composite particles in the low flowrate simulation, end up with larger diameters as they exit the bronchial outlets. This is due to the longer residence times in the upper airways and to the more optimum airflow conditions in the tracheobronchial tree. For the same particle sizes, the deposition fractions are much higher in the high flowrate due to the increased inertia of the particles, which results to direct impaction on the airway walls. The results for the intermediate flowrate lie somewhere in-between the low and high inhalation flowrate curves.

Finally, deposition sites of selected particle sizes are revealed in Figure (12). The selected sizes are based on the discussion of Figure (10). For the pure drug particles the main deposition site is in the mouth-throat region. It worths mentioning that the deposition in the oral cavity differs for the low inhalation flowrate. This is due to the different inlet conditions between the simulated flowrates, i.e. laminar vs turbulent. For the relatively large composite particles, deposition can be seen in the mouth-throat region but is low. On the other hand, for the relatively small composite particles we can barely see any deposition in this region. For both particle sizes the main deposition sites are expected to be in the distal airway generations that are not simulated.

4 Conclusions

This project contributes to the research and development in the field of pulmonary drug delivery, aiming to the improvement of delivery efficiency of inhaled medicines. Here we have shown that hygroscopic excipients can be

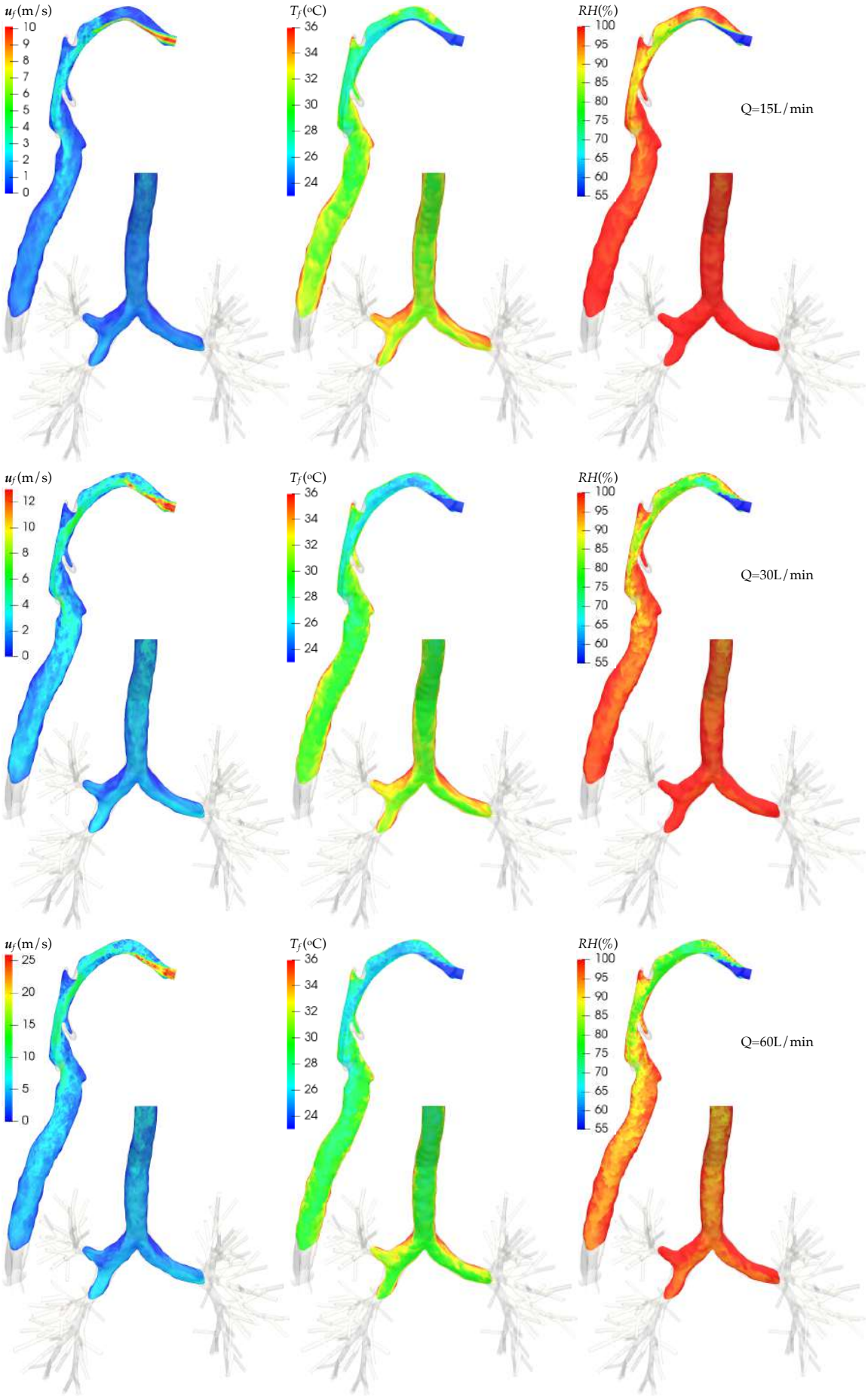

Figure 8: Instantaneous airflow velocity, temperature, and relative humidity at main cross sections of the airway. Top/Middle/Bottom row figures for low/intermediate/high inhalation flowrate

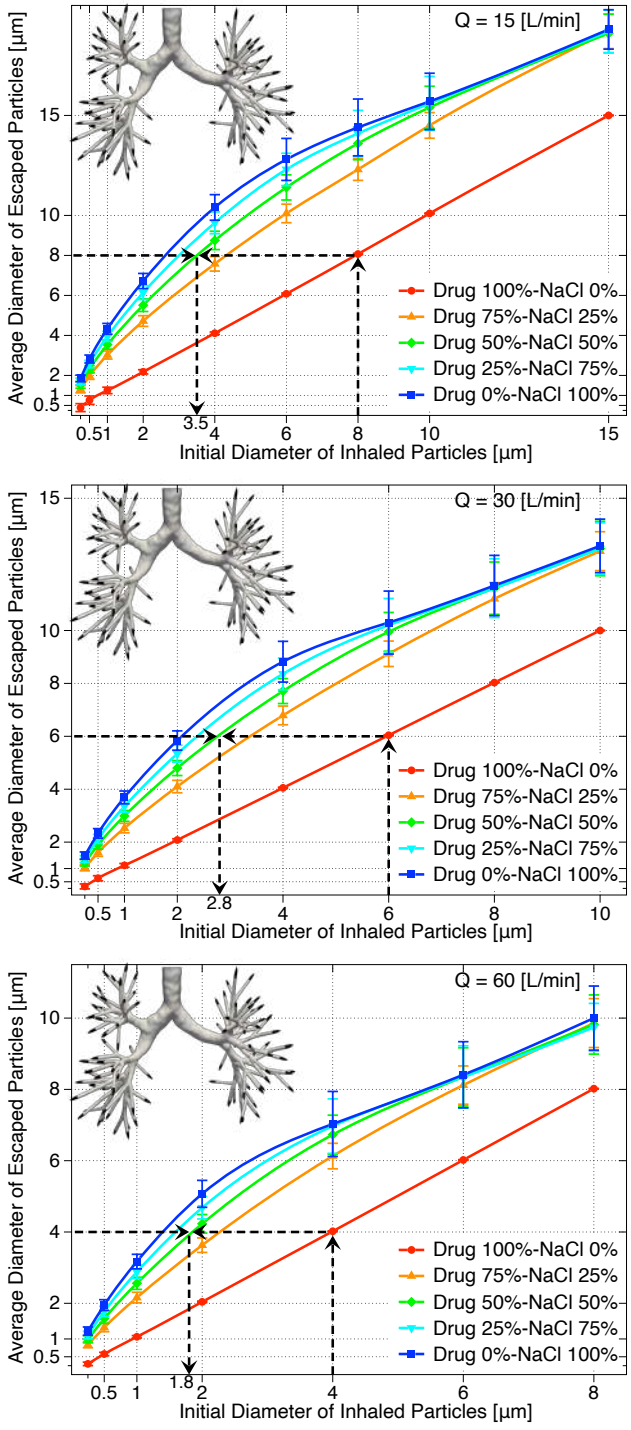

Figure 9: Mean size of particles escaping from the bronchial outlets, as a function of their initial dry size. Results for five drug-excipient composites. Top/Middle/Bottom figures for low/intermediate/high inhalation flowrate

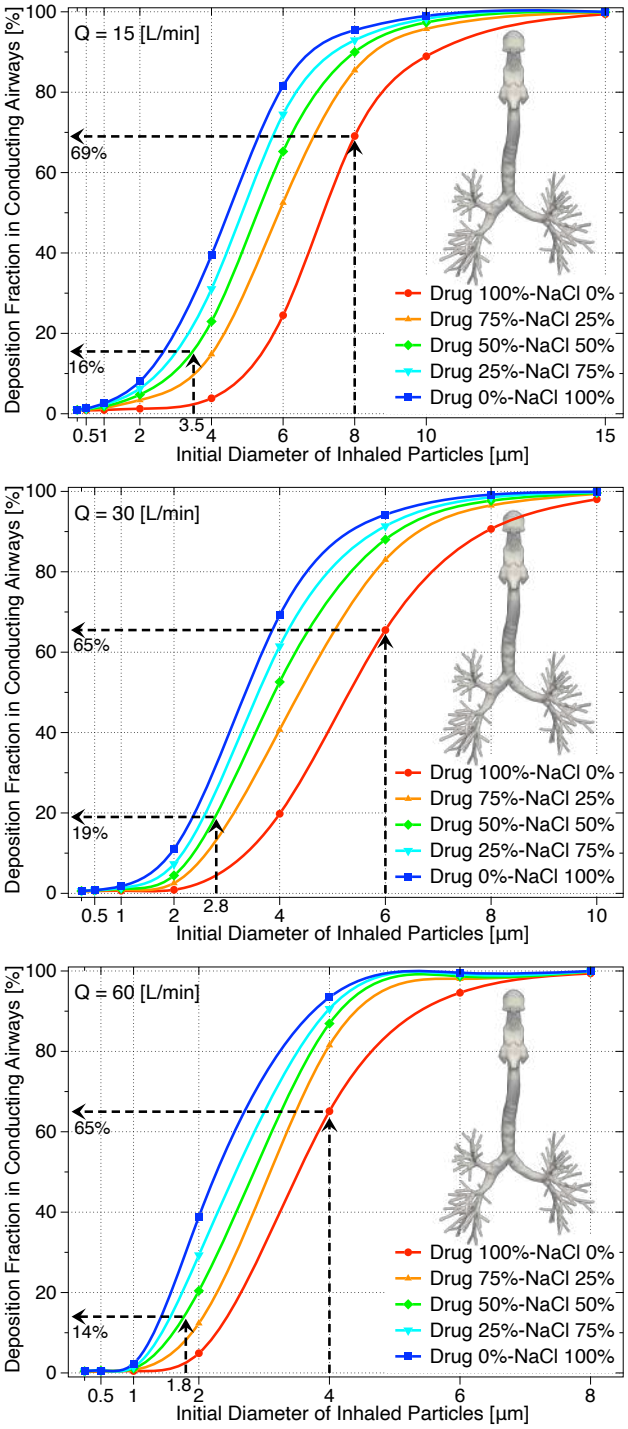

Figure 10: Deposition fraction as a function of the initial particle size. Results for five drug-excipient composites. Top/Middle/Bottom figures for low/intermediate/high inhalation flowrate

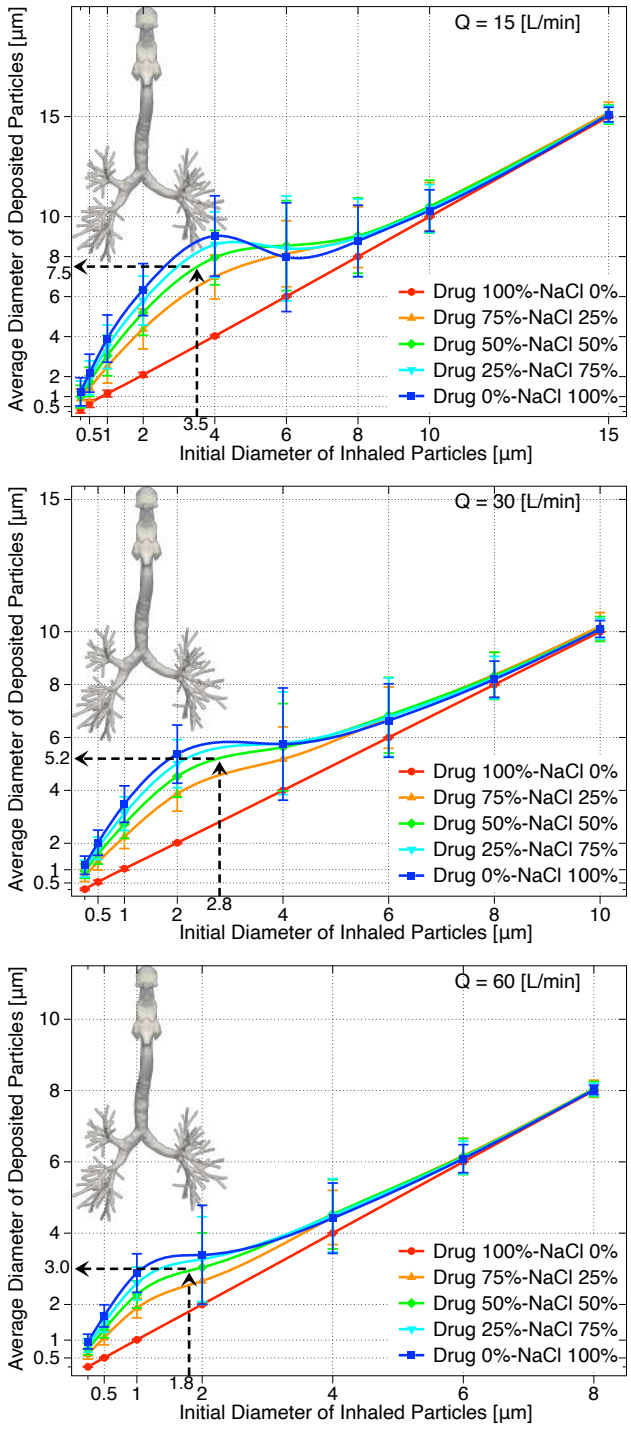

Figure 11: Mean size of particles deposited on the airway wall, as a function of their initial dry size. Results for five drug-excipient composites. Top/Middle/Bottom figures for low/intermediate/high inhalation flowrate

used to increase the effectiveness of drugs in accordance with findings from previous studies [2]. This can be achieved by inhaling initially submicron drug-excipient composites associated with negligible losses in the conducting airways. The results suggest that one should be able to optimise the combination of initial particle size and hygroscopic excipient content to achieve improved diseased airway selectivity. Furthermore, the current methodology can be used for the study of pathogen and environmental particle exposure, sensitive to humidity conditions.

References

[1] P. W. Longest and M. Hindle, "Excipient enhanced growth (EEG) of nanoparticle aerosols to enable improved pulmonary targeting and retention," *Provisional Patent Application*, 2009.

[2] P. W. Longest, G. Tian, X. Li, Y.-J. Son, and M. Hindle, "Performance of combination drug and hygroscopic excipient submicrometer particles from a soft-mist inhaler in a characteristic model of the airways," *Annals of biomedical engineering*, vol. 40, no. 12, pp. 2596–2610, 2012.

[3] P. W. Longest and M. Hindle, "Condensational growth of combination drug-excipient submicrometer particles for targeted high efficiency pulmonary delivery: comparison of CFD predictions with experimental results," *Pharmaceutical research*, vol. 29, no. 3, pp. 707–721, 2012.

[4] F. S. Stylianou, J. Sznitman, and S. C. Kassinos, "Direct numerical simulation of particle laden flow in a human airway bifurcation model," *International Journal of Heat and Fluid Flow*, vol. 61, pp. 677–710, 2016.

[5] F. S. Stylianou, S. I. Angeli, S. C. Kassinos, and M. Svensson, "The effect of flow rate, head position, and inhaler orientation on the airflow and particle deposition in an MRI-based mouth-throat geometry," in *Tenth International Symposium on Turbulence and Shear Flow Phenomena*, Begel House Inc., 2017.

[6] D. Wu, M. H. Tawhai, E. A. Hoffman, and C.-L. Lin, "A numerical study of heat and water vapor transfer in MDCT-based human airway models," *Annals of biomedical engineering*, vol. 42, no. 10, pp. 2117–2131, 2014.

[7] P. W. Longest and M. Hindle, "Numerical model to characterize the size increase of combination drug and hygroscopic excipient nanoparticle aerosols," *Aerosol Science and Technology*, vol. 45, no. 7, pp. 884–899, 2011.

[8] G. Tian, P. W. Longest, G. Su, R. L. Walenga, and M. Hindle, "Development of a stochastic individual path (sip) model for predicting the tracheobronchial deposition of pharmaceutical aerosols: Effects of transient inhalation and sampling the airways," *Journal of Aerosol Science*, vol. 42, no. 11, pp. 781–799, 2011.

[9] R. E. Bank, W. M. Coughran, W. Fichtner, E. H. Grosse, D. J. Rose, and R. K. Smith, "Transient simulation of silicon devices and circuits," *IEEE Transactions on Computer-Aided Design of Integrated Circuits and Systems*, vol. 4, no. 4, pp. 436–451, 1985.

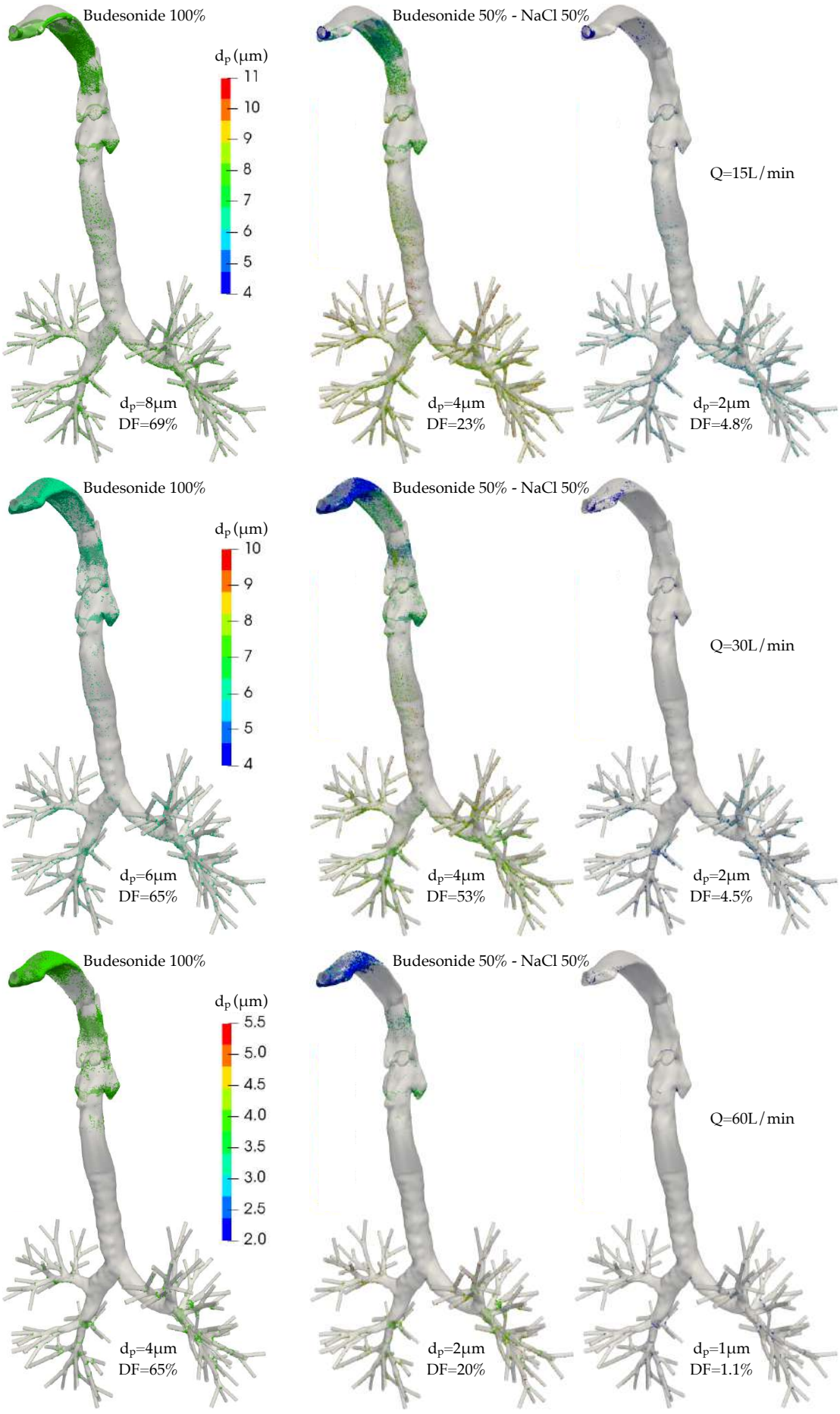

Figure 12: Deposition sites coloured by the final particle diameter at the time of deposition. Top/Middle/Bottom row figures for low/intermediate/high inhalation flowrate. First column for pure Budesonide particles, second and third columns for composite particles. The initial particle diameters and the deposition fractions are noted

Experimental and Computational Modelling of Aerosol Transport Using the BUT Benchmark Human Lung Model

F. Lizal, J. Elcner, M. Belka, J. Jedelsky, and M. Jicha

CBrno University of Technology, Faculty of Mechanical Engineering, Energy Institute, Technicka 2896/2, Brno 616 60, the Czech Republic

Abstract

The aerosol team at the Brno University of Technology (BUT) has continuously developed a realistic human lung model and has used it for aerosol transport studies since 2006.

The model was originally based on the digital reference model of [1] and contained airways from the throat down to the 7th generation of branching. It was gradually extended on the upper part with the mouth and nasal cavity. Also, its simplified versions were designed for specific research applications (Y-shaped model, semirealistic model). It was fabricated in two forms, as a transparent model for optical flow measurements and segmented for deposition testing. Originally it was ventilated using a single-cylinder breathing simulator that was later updated to a 5-piston breath generator which enables prescription of the individual course of breath for each lung lobe.

The paper summarises up to date results acquired with different versions of the BUT model and gives examples of the outcomes acquired by several teams throughout Europe, including the COST Siminhale collaborators. Selected flow and deposition results were published in the Ercoftac database.

1 Introduction

Millions of particles enter the human airways with every single breath even in environments considered to be clean. The particles may be exhaled, or deposited in various sites of airways. Their effect on human health depends on chemical composition, size, shape, density, porosity, individual geometry of airways, breathing pattern and other factors. Obviously, some particles can be more harmful than others, some may even be beneficial to our health.

The ability to predict deposition sites of inhaled particles has been desired since several decades ago for regulatory, toxicological or pharmaceutical purposes. Various applications require different precision of such calculations. For example, hygienic and occupational regulations usually rely on rather universal predictions provided e.g. by the model of the International Commission on Radiological Protection (ICRP, [2]). However, recent orientation at patient-tailored medicine [3] requires ever more detailed spatial resolution and accuracy.

It is without question that combined CFPD (computational fluid and particle dynamics) calculations and PBPK/TK (physiologically based pharmacokinetic/toxicokinetic) models will help to more efficient and cheaper prevention and treatment of various diseases [4]. However, to satisfy the best-practice standards, it is necessary to validate the calculations by experimental results [5]. The creation of a database of reliable experimental results is a long-time task. This article presents the most important milestones and results of such an effort to provide reliable experimental data and support the effort to establish best-practise guidelines for modelling of deposition of particles in human airways.

Some of the presented models and results have been already utilized by Ercoftac and recommended as a benchmark for biofluid modelling [6]. CFPD calculations performed by several teams on the identical replica of airways was documented in [7]. The set of both experimental and digital models is being constantly updated for over a decade, however, care is taken to preserve the basic geometry and allow comparison with previous generations of the model.

2 Materials and Methods

The *in vitro* and *in silico* research of aerosol transport in the human airways requires simulation of the airway geometry with sufficient fidelity, setting appropriate boundary conditions and using up to date experimental or computational methods. These aspects are addressed in brief in this section with links to literature where the reader can find more detailed information.

2.1 Model Geometries

The research team was established by prof. Miroslav Jicha at BUT in 2006 to study the transport of aerosols in human airways. The team was based on existing multiphase flow know-how but their work started from zero with no model and instrumentation available. The group first acquired a three-dimensional computed tomography (CT) scan of an adult Caucasian male from the St. Anna University Hospital in Brno, the Czech Republic. That scan included realistic geometries of the airways with the epiglottis and glottis. The quality down to the bronchial tree was reduced due to motion during the scanning process. That geometry was combined with a digital reference model of [1]. Schmidt's geometry contained parts from the trachea to the 17^{th} bronchial generation. It was produced by a high-resolution CT of an excised lung of an adult male free of pathological alterations. The bronchial tree was truncated at 3^{rd} to 4^{th} or at 7^{th} to 8^{th} bronchi generation to allow for physical realisation and resulted in BUT2008-3gen or BUT2008-7gen model respectively (see Figure (1)). The differential branches of the two versions are shown in red in Figure (1). For the applications of the BUT2008-7gen model see ([8],[9]).

The next step was to develop a model containing the oral cavity. An upper part of the Lovelace Respiratory

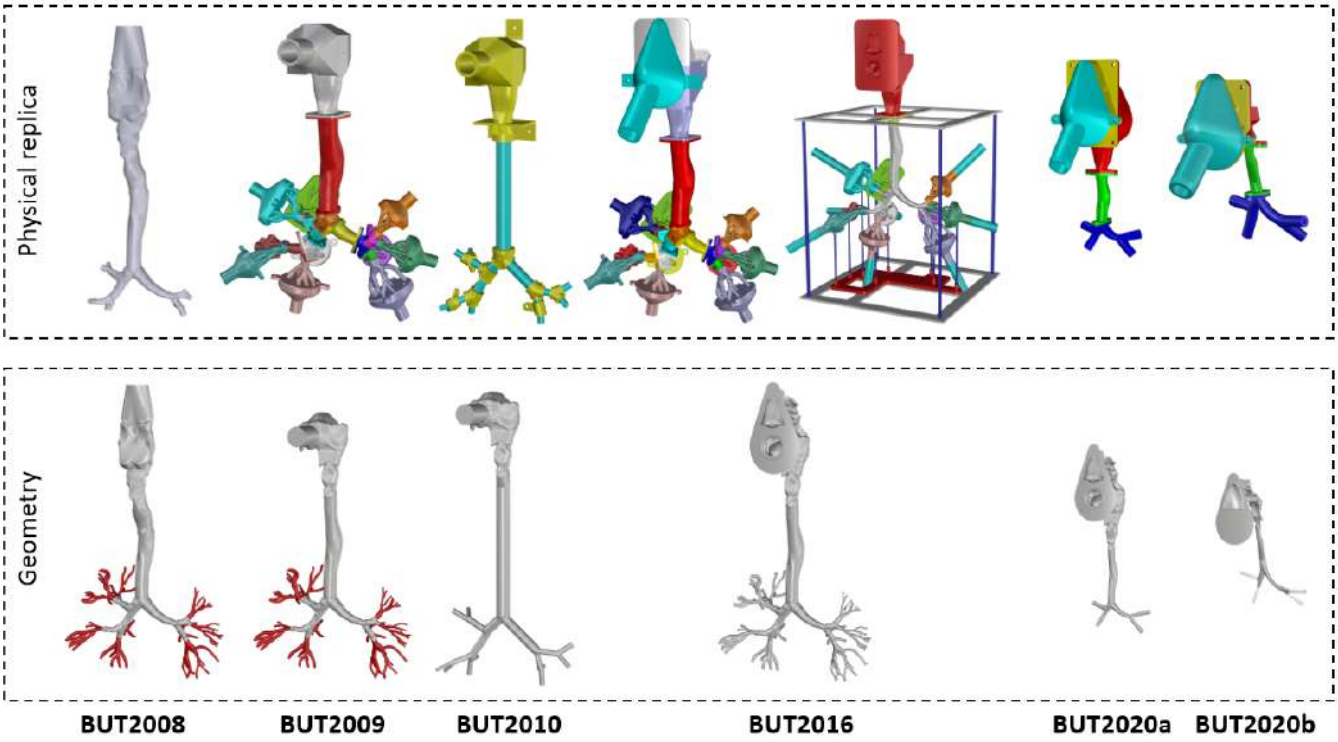

Figure 1: Overview of the lung geometries and corresponding physical replicas (3D render)

Research Institute 'A model' [10] was used to extend the previous model into a BUT2009 model. The resulting physically realistic geometry of the respiratory tract consisted of the oral cavity, larynx and tracheobronchial (TB) tree down to several generations of branching.

The simplified geometry of that model was derived by replacing the realistic airway shapes with cylindrical tubes to form a so-called semi-realistic model (BUT2010). A simple Y-shaped model that simulated the first bifurcation was used for specific research applications [11].

The models were fabricated in two forms: as an optically transparent replica for the application of optical measurement methods and as a segmented replica for particle deposition studies. All these models, their geometry (lengths, diameters and branching angles of the TB tree) and fabrication methods are reported in [12].

New aerosol transport studies required a more detailed and complete model. The existing geometry was therefore extended with a nasal cavity, which was connected to the oral cavity of the BUT2009 model. The nasal cavity geometry was acquired from the University of California Davis [13] as a computed tomography scan of the nasal cavity of a healthy 25-year old male. This connection was done following the available literature [14] and consulted with an experienced otorhinolaryngologist. To ensure the realistic velocity field at the geometry inlet, the exterior of the model was shaped in a face-like manner. The BUT2016 model facilitated the comparison of airflow and deposition during nasal, oral and combined breathing and it is detailed in [15].

The BUT2016 model was rescaled to mimic the lungs of a 5-years old child as BUT2020a. Based on the reviewed literature we concluded that the fast development of human airways in early childhood slows down at the age of five. Then the airways gain basically the identical shape as the airways of adults [16].

This perspective opened the possibility to scale down the original BUT replica of adult airways. The question that had to be solved was what scaling factor shall be used. It must be emphasized, that the human body, including airways, differs significantly from individual to individual. The differences are conditioned by genetic predispositions, nutrition during pregnancy and childhood, underwent diseases and other factors. All these elements result in large variations of dimensions among people [17]. The sizes of the mouth and nose cavities in our original model are smaller than average ([18], [19]). Scaling aimed to represent the same individual as the original BUT replica, at the age of five. As was already mentioned, the original BUT replica was created from several datasets under the careful supervision of an experienced otorhinolaryngologist.

The literature survey ([20], [21], [22], [23], [24], [25], [26], [27], [16], [28]) demonstrated that although many teams performed or reported detailed measurements of dimensions of human airways during development from early childhood to adulthood, it is difficult to combine the provided results because definitions of the measured distances and dimensions are not standardized and different groups established their specific methodologies.

Nonetheless, eventually, two parameters were selected for scaling of the BUT replica. The length of the trachea, as reported in [23] and [29], and length of the nose (i.e. length of the nasal cavity to the end of the septum). Following the above-mentioned studies, the length of the trachea (specifically the distance from the glottis to the carina of the first bifurcation) was scaled down from the original 136 mm to 73 mm, which corresponds to a five years old child. Instead of the seven generations of airway branching which were present in the original replica, only two generations were prepared for the five years old child, because of the small dimensions of airways (the diameter of the smallest airway in the second generation is 3 mm) and 3D printing restrictions.

It has been documented that intersubject variability of the dimensions of the trachea is smaller compared to upper airways [30]. It is well known that the ratio of

the size of the head to the size of the body is larger for kids compared to adults. It was not possible to use the identical scaling factor used for the trachea also for the nasal and oral cavity because their dimensions were too small. Apparently, the growth of the trachea and upper airways happen at a different pace. Hence, the upper airways were scaled according to a curve of the growth of the nasal cavity with age which has been reported in [25]. The same growth factor has been applied to the BUT original geometry. The pharynx has been adjusted manually to connect the upper airways and trachea to maximally preserve the fidelity of the topology.

The last member of the collection of models is a replica of the airways of a 10-months old child (the BUT2020b, see Figure (1)). The geometry comes from a high-resolution computed tomography scan performed at the Brno university hospital. The airway geometry was extracted from individual images by segmentation performed in an in-house code by Jakub Laznovsky (CEITEC, Brno, the Czech Republic). The identified borderlines were then interpolated and converted to a 3D geometry. That geometry of airways was checked, discussed with the otorhinolaryngologist and finally polished in software Rhinoceros (McNeel Europe SL, Barcelona, Spain). The same software was used for the design of the actual physical replica shaped around the finished âĂIJinnerâĂİ airway geometry, including the shaping of the facial part performed in a similar way as for previous replicas (see Figure (1) atop).

All the models of airways described above exist in a form of physical replica and also in a form of digital geometry suitable for computational simulations.

After 15 years the model development is still an ongoing work. Human airways are a complex biomechanical system and the up to date models can be highly improved even from the mechanical point of view.

2.2 Boundary conditions

2.2.1 Experimental realisation

The experimental equipment used to study the airâĂŞparticle flow consists of a flow source, a particle generator, an airway model and an appropriate measurement method. The studies are performed using steady inspiration or expiration, or, more realistically under oscillatory flow conditions.

The steady flow through the replica is induced by a vacuum pump connected to the terminal branches of the replica. The flow distribution through the individual branches is accomplished by adding rotameters between the replica and the vacuum pump, see [8].

Originally, a single-cylinder breathing simulator was used to produce the oscillatory flow ([31], [32]). It provided a sinusoidal piston motion with appropriate frequency and amplitude representing inspiratory/expiratory phases of the breathing cycle. It was later updated to a 5-piston breath generator which enables prescription of the individual course of breath for each lung lobe [33]. This allowed to set up different time-dependent velocity profiles at each lobe outlet and simulate different breathing conditions of healthy and asthmatic individuals that are manifested not only in terms of different inhaled volumes and breathing frequency but also in the different flow distribution among the five lung lobes.

Spherical monodisperse aerosol particles were usually produced by Condensation Monodispersed Aerosol Generator (model TSI 3475, TSI Inc. Shoreview, MN, US). The particles can be generated in the range from 1 to 8 μm from di-2-ethyl-hexyl sebacate (DEHS) vapours condensed on small particles of sodium chloride. Also, monodisperse glycerol aerosol and multicomponent aerosol produced by the condensation methods were used [34].

Glass fibres were used in several studies. The methodology for their production, classification and introduction into the model was detailed in [8]. Superparamagnetic microrods were used in [11].

Spray-dried chitosan and mannitol particles tagged with fluorescein sodium salt were used to simulate drug carriers for inhalation therapy in [33]. The particles were injected into the airways by a small-scale powder disperser (TSI SSPD 3433).

2.2.2 Numerical realisation

The boundary conditions replicate the experimental research, where models are made of rigid material and represent a particular section of the respiratory tract that is inserted into the air duct of the experimental stand. The model wall is treated with the standard wall boundary condition, with fixed tangential velocity and no-slip shear stress specification. The inlet of the model, located on the mouth nozzle is prescribed with a pressure outlet boundary condition with zero pressure resistance. To respect the realistic behaviour of the flow, the flow is initiated by a velocity boundary condition at the outlets located on the terminal part of the tracheobronchial tree. The outlets are circular in cross-section and the shape of the velocity profile is then treated with a function corresponding to the character of the flow (laminar/turbulent), according to the selected breathing regime. In terms of the velocity prescription, it is necessary to distinguish the investigated modes of lung behaviour. In the case of stationary inspiration, a constant velocity value was prescribed, in the normal direction of the selected boundary [15]. In the case where the flow was investigated during part/whole respiratory cycle, the selected flow velocity was a function of time and the characteristics of the actual breathing regime were investigated ([35], [36]). If the deposition study was considered, a matrix of points located in the region of the mouth nozzle on the oral cavity of the model was created. This matrix has allowed the injection of particles fully dispersed in inhaled air for the purposes of the study performed by Euler - Lagrangian approach [15].

2.3 Methods

Methods established in experimental fluid mechanics for flow and deposition studies were applied here, and in some cases, these were improved to better suit the purpose.

2.3.1 Experimental results

Several flow-measurement methods were applied to the optically transparent lung model versions. Phase Doppler anemometry (PDA) served for size and velocity measurements of aerosol particles suspended in airflow and validation of corresponding numerical simulations ([31], [15]). The measurements provided time-resolved velocity data for estimation of the power spectral density (PSD) of velocity fluctuations [32].

Particle Image Velocimetry (PIV) measurements were made using a refractive index-matched, transparent model [40]. The aim was to provide experimental data for Large Eddy Simulations (LES) on the SimInhale

Table 1: Overview of model versions and the related work

Model version / modification	Research type*	Boundary conditions **	Method used	Outcomes***	Citation
BUT2008	E	S, C, P	PDA	F	[32]
	E, S	C, Si	PDA, SST k-ω low-Re Number RANS	F	[31]
BUT2009	E	S, P	PET	D	[9]
	E	S, P	GS-MS	D	[34]
	E, S	S, P	PET, several LES and RANS models	F, D	[7]
	E	S, F	Microscopy with fibre counting	D	[8]
	E, S	S, P	GC-MS, RANS with lagrangian sub-grid model, zero-gradient extrapolation model	D	[37]
	S	S, P	LES, dynamic version of the Smagorinsky-Lilly subgrid scale model	F, D	[38]
	S	S	k-ω SST model with low-Re correction	D	[39]
	E, S	S	PIV, LES Smagorindsky-Lilly subgrid scale model	F	[40]
	E, S	S, P	PIV, several RANS models (standard k-ϵ, RNG k-ϵ, standard k-ω SST), Reynolds stress model, LES Smagorindsky-Lilly subgrid scale model	F, D	[41]
BUT2016	E, S	CR	SST k-ω turbulence model with low-Re correction	F, D	[33]
	E, S	S	LDA, PET, LES with WALE viscosity subgrid scale model	F, D	[15]

*experiment (E), simulation (S)
**Flow regime: steady (S), cyclic (C), sinusoidal (Si), realistic (R), with spherical particles (P), with fibres (F)
***Character of the outcomes: flow field (F), particle deposition (D)
[1]PDA Phase Doppler anemometry, [2]RANS Reynolds-averaged Navier-Stokes, [3]PET Positron emission tomography, [4]GC-MS Gas chromatography-mass spectrometry, [5]LES Large Eddy simulation, [6]LDA Laser Doppler Anemometry, [7]WALE Wall-Adapting Local Eddy-viscosity

benchmark case. The obtained experimental data are a part of the publicly accessible ERCOFTAC database.

The deposition of inhaled spherical aerosol particles was investigated by positron emission tomography (PET) ([38], [15]) using a segmented replica of the BUT2009-7gen model and method developed in [9]. Compared deposition of monodisperse glycerol and multicomponent aerosols were provided using gas chromatography-mass spectrometry (GC-MS) in [34].

Regional deposition of uniform diameter glass fibres was investigated on the same model [8] using a novel automatic image processing method [42].

All the above described experimental methods were reviewed in detail in [5].

2.3.2 Computational methods

With the development of computing hardware, the complexity of the models used for numerical studies increased. The first numerical simulations performed on BUT models were carried out on constrained geometry with a lower number of control volumes, which allowed the flow analysis using the RANS approach under steady-state conditions [7]. The most suitable model of turbulence from the available range of models was the MenterÂťs SST k-ω model, used in all numerical studies based on the RANS approach performed on BUT. For a more accurate description of the flow behaviour in the near-wall region, the low-wall y+ approach was chosen to simulate the boundary layer. The deposition study using the RANS approach then included a Lagrangian multiphase model with a turbulent dispersion model to account for the effect of turbulence on particle movement. However, the RANS approach is not sufficiently accurate for deposition studies due to its isotropic turbulence behaviour assumption and for this reason, it was necessary to shift the calculations towards LES where the WALE (Wall-Adapting Local Eddy-viscosity) sub-grid scale model was incorporated under non-stationary conditions. The methods suitable for transitional and turbulent flow in constricted airways such as glottal opening or airway obstruction were investigated in [35]. Several

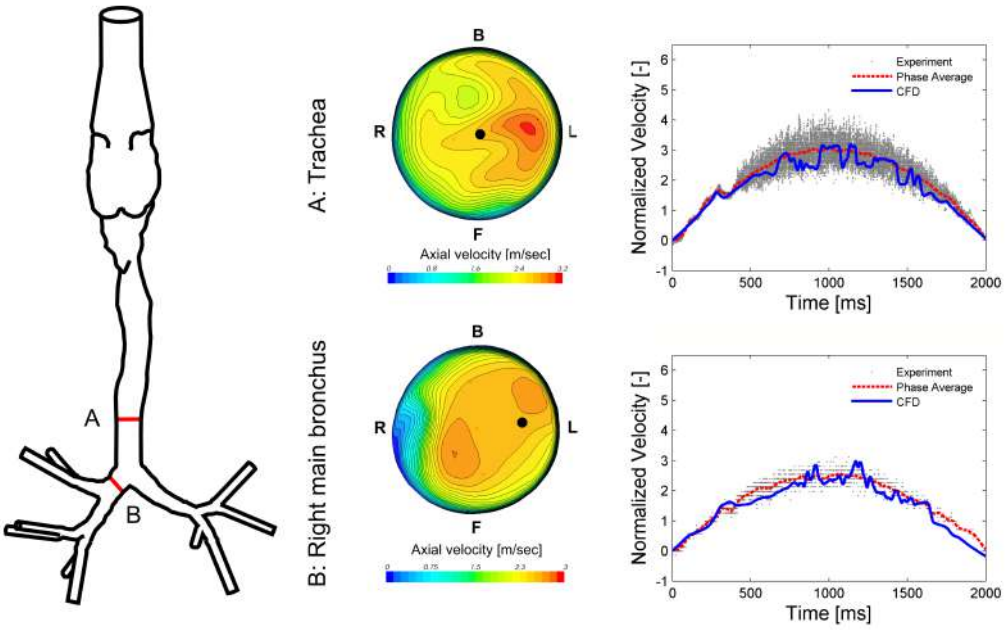

Figure 2: Results of experimentally measured and computationally simulated velocity fields in the trachea and right main bronchus

teams gathered within the SimInhale project performed a comparative study [7] on the BUT2009-7gen model on a wide range of turbulence modelling approaches (LES - WALE, LES - Smagorisky-Lilly, RANS - SST k-ω, RANS - k-ϵ) and a large range of computational grid densities (1.3 - 50 million of cells). In all cases, deposition was modelled by the Euler - Lagrange approach. Studies differed by using different time integration schemes and different numbers of particles injected into the domain. The results from this study performed by Koullapis were further used in a paper [40] and [41], where the results of the numerical simulation were compared with the PIV method and several RANS approaches. In 2018 Frederix et al. performed a size-dependent aerosol deposition study [37] where he adopted a compressible Eulerian description of multi-species aerosol and described its state in terms of the mixture density, velocity and temperature for the different mass fractions of vapour and liquid phases. This study was also performed on the BUT2009-7gen model.

3 Results and discussion

3.1 Review of published results

An overview of the journal articles which published both experimental and computational results acquired using all BUT airway models is given in Table (1). The table describes the type of replica used, the research approach (experimental or computational simulations), boundary conditions, the type of the applied method and the type of outcome (velocity field or deposition).

The physical version of the first replica of airways, the BUT2008, was used for measurements of airflow using PDA. The identical digital geometry was then used for calculations and both approaches were compared in [31]. The most extensive application was recorded for the BUT2009, which was also used within the COST ACTION project MP1404 Siminhale by several groups and became a âĂIJbenchmarkâĂİ for the simulations of airflow and deposition of inhaled particles [7]. The same model is listed as one of the test cases in the ERCOFTAC knowledge base [6]. Apart from the data on the deposition of spherical particles, also results on the deposition of fibres are available. Publications from the year 2020 reported results from the replica with the nasal cavity (BUT2016). Besides the publications in Table (1), preliminary results were frequently presented and discussed during international conferences focused on fluid mechanics or aerosol transport.

3.2 Selected results

For the sake of conciseness, only selected results can be presented within this paper. One paper focused primarily on the investigation of the flow field [31], and one paper on deposition [15] have been selected.

In the former paper, the original BUT2008 model has been used for the investigation of the effect of oscillatory inhalation flow. The flow field has been modelled by SST k-ω low-Reynolds Number RANS and experimental validation was performed by PDA. Illustrative results can be seen in Figure (2). The results documented that RANS calculations were able to predict the temporal development of the flow, although especially the separation zone in the right main bronchus meant a challenge. Also, while RANS approach captures the flowfield with reasonable accuracy, RANS deposition predictions are more sensitive to model tuning and parameter selection than in LES. The transition from a laminar to a turbulent regime was predicted accurately in almost all locations. Temporal development of turbulent kinetic energy (TKE) has been observed from the pharynx to the third generation of branching. TKE rose abruptly after the glottis and along the airways, while each branching induced another local increase in TKE. As regards the temporal behaviour, the TKE was essentially zero before the peak of inspiration, demonstrating a laminar character of the flow. The highest TKE developed after peak inspiration, despite the decreasing Reynolds number.

The paper confirmed that RANS calculations can provide sufficiently precise results as regards the flow field.

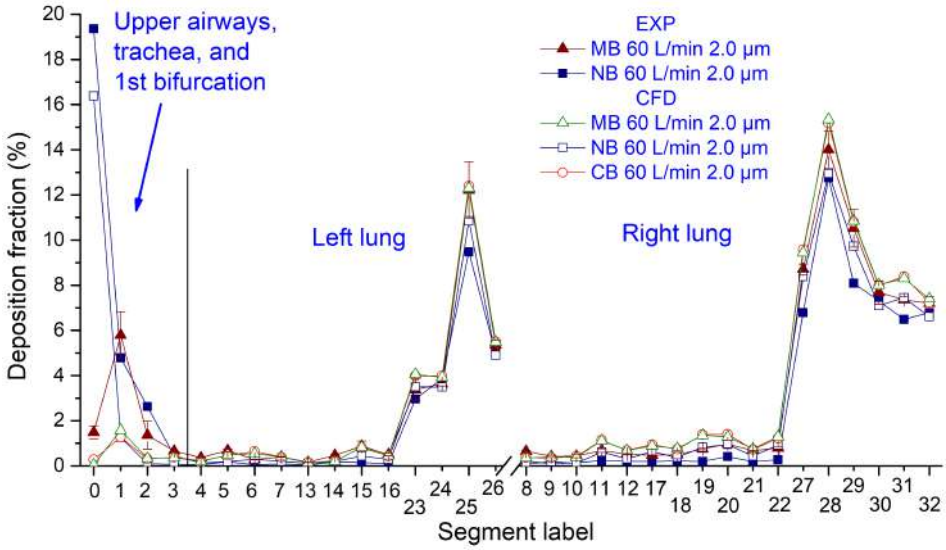

Figure 3: Comparison of deposition fraction in specific segments of the BUT2009 airway replica measured experimentally and calculated by CFD for a flow rate of 60 L/min, 2μm particles, and three inhalation regimes (MB-mouth breathing, NB-nose breathing, CB-combined breathing).

This information is important for the successful application of computational fluid dynamics (CFD) calculations in patient-tailored medicine, the speed of the calculation is essential.

The second paper [15] selected for this text focused on the comparison of the effect of mouth, nose or combined breathing on the flow and deposition patterns in the tracheobronchial tree. Apart from measurements and calculations of velocity, it brought also regional deposition measured by positron emission tomography.

The results showed, that apart from the high filtration efficiency of the nose, there is no further difference in the regional distribution of inhaled particles among the nose and mouth breathers (see Figure (3)). On the contrary to the common expectations, the carina of the first bifurcation was not a significant deposition hotspot. Nonetheless, deposition hotspots were identified in the second bifurcations in both lungs and also in the third bifurcations in the left lung.

4 Conclusions

The continuous development of the replicas of airways at BUT is ongoing since 2006. Over time, also many other international teams performed computational calculations and experimental measurements. Due to the long-lasting international effort, it is possible to predict the overall and to a certain extent also regional deposition with relatively good precision. Nonetheless, the correct setup of calculations and appropriate setting of the boundary conditions is not a matter of course. This paper presented and cited results that document what data are available and how were they acquired. The digital geometries and the related computational meshes described here are available to any research group for non-profit purposes upon request by the authors of this article. The original airway geometry without the nasal cavity can be downloaded from the Ercoftac database [38].

Despite the laudable progress in both experimental and especially computational methods, there are still limits that need to be pushed. The fundamental one is the absence of the complete digital geometry containing airways from the nasal and oral cavity down to the alveoli. On the other hand, calculations on such a complex and exhaustive geometry would be impossible to the full extent (all possible paths) due to the limited power of current computers. Also, setting the truly physiological boundary conditions remains a challenge due to reasons on both sides âĂŞ experimental acquisition of such data and limited computational power.

Although the future of patient-tailored simulations seems bright, several obstacles complicate the process. The image processing and airway segmentation need to be accelerated to fully utilize the potential in clinical practice. Also, the calculations must be sufficiently precise and yet fast. One can hardly expect acceptance of longer calculation times than overnight.

Nevertheless, as soon as these challenges are overcome, reductions in the cost of treatment (due to the minimization of doses) and dampening of side effects (thanks to precise targeting) can be envisioned. The imminent goals are 1) improvement of resolution of the deposition calculations (to be able to predict deposition hot-spots on micrometre scale); 2) more precise calculations of non-spherical particles (porous and fibrous); and 3) incorporation of physiologically realistic features of airways (wall motion and surface roughness effects, mucociliary clearance, hygroscopic growth, electrostatic effects, and their simultaneous influence). Progress should come in the area of gender differences and aerosolâĂŞlung interactions during the development of lungs from early childhood to adulthood.

Acknowledgment

This work was supported by the Czech Science Foundation project GA 20-27653S.

References

[1] A. Schmidt, S. Zidowitz, A. Kriete, T. Denhard, S. Krass, and H. O. Peitgen, "A digital reference model of the human bronchial tree," *Computerized Medical Imaging and Graphics*, vol. 28, no. 4, pp. 203–211, 2004.

[2] M. R. Bailey, "The new icrp model for the respiratory-tract," *Radiation Protection Dosimetry*, vol. 53, no. 1-4, pp. 107–114, 1994.

[3] L. Housman, "Innovative tests for patient-tailored treatments: demonstrating value in the age of personalized medicine," *Personalized Medicine*, vol. 8, no. 2, pp. 183–189, 2011.

[4] Y. Feng, J. N. Zhao, H. Hayati, T. Sperry, and H. Yi, "Tutorial: Understanding the transport, deposition, and translocation of particles in human respiratory systems using computational fluid-particle dynamics and physiologically based toxicokinetic models," *Journal of Aerosol Science*, vol. 151, 2021.

[5] F. Lizal, J. Jedelsky, K. Morgan, K. Bauer, J. Llop, U. Cossio, S. Kassinos, S. Verbanck, J. Ruiz-Cabello, A. Santos, E. Koch, and C. Schnabel, "Experimental methods for flow and aerosol measurements in human airways and their replicas," *European Journal of Pharmaceutical Sciences*, vol. 113, pp. 95–131, 2018.

[6] P. Koullapis, F. Lizal, J. Jedelsky, L. Nicolaou, K. Bauer, O. Sgrott, M. Jicha, M. Sommerfeld, and S. Kassinos, "Aerosol deposition in the human upper airways," vol. 2020, no. 03/06, 2019.

[7] P. Koullapis, S. C. Kassinos, J. Muela, C. Perez-Segarra, J. Rigola, O. Lehmkuhl, Y. Cui, M. Sommerfeld, J. Elcner, M. Jicha, I. Saveljic, N. Filipovic, F. Lizal, and L. Nicolaou, "Regional aerosol deposition in the human airways: The siminhale benchmark case and a critical assessment of in silico methods," *European Journal of Pharmaceutical Sciences*, vol. 113, pp. 77–94, 2018.

[8] M. Belka, F. Lizal, J. Jedelsky, J. Elcner, P. K. Hopke, and M. Jicha, "Deposition of glass fibers in a physically realistic replica of the human respiratory tract," *Journal of Aerosol Science*, vol. 117, pp. 149–163, 2018.

[9] F. Lizal, M. Belka, J. Adam, J. Jedelsky, and M. Jicha, "A method for in vitro regional aerosol deposition measurement in a model of the human tracheobronchial tree by the positron emission tomography," *Proceedings of the Institution of Mechanical Engineers Part H-Journal of Engineering in Medicine*, vol. 229, no. 10, pp. 750–757, 2015.

[10] Y. Zhou and Y. S. Cheng, "Particle deposition in a cast of human tracheobronchial airways," *Aerosol Science and Technology*, vol. 39, no. 6, pp. 492–500, 2005.

[11] M. Nikolaou, K. Avraam, A. Kolokithas-Ntoukas, A. Bakandritsos, F. Lizal, O. Misik, M. Maly, J. Jedelsky, I. Savva, F. Balanean, and T. Krasia-Christoforou, "Superparamagnetic electrospun microrods for magnetically-guided pulmonary drug delivery with magnetic heating," *Materials Science & Engineering C-Materials for Biological Applications*, vol. 126, 2021.

[12] F. Lizal, J. Elcner, P. K. Hopke, J. Jedelsky, and M. Jicha, "Development of a realistic human airway model," *Proceedings of the Institution of Mechanical Engineers Part H-Journal of Engineering in Medicine*, vol. 226, no. H3, pp. 197–207, 2012.

[13] R. Sarangapani and A. S. Wexler, "Modeling particle deposition in extrathoracic airways," *Aerosol Science and Technology*, vol. 32, no. 1, pp. 72–89, 2000.

[14] R. Putz and R. Pabst, *Atlas of Human Anatomy Sobotta*. Praha: Grada, translation of 22nd edition, 1st czech edition ed., 2007.

[15] F. Lizal, J. Elcner, J. Jedelsky, M. Maly, M. Jicha, A. Farkas, M. Belka, Z. Rehak, J. Adam, A. Brinek, J. Laznovsky, T. Zikmund, and J. Kaiser, "The effect of oral and nasal breathing on the deposition of inhaled particles in upper and tracheobronchial airways," *Journal of Aerosol Science*, vol. 150, 2020.

[16] J. X. Xi, X. H. Si, Y. Zhou, J. Kim, and A. Berlinski, "Growth of nasal and laryngeal airways in children: Implications in breathing and inhaled aerosol dynamics," *Respiratory Care*, vol. 59, no. 2, pp. 263–273, 2014.

[17] M. Hussain, W.-H. Renate, and H. Werner, "Effect of intersubject variability of extrathoracic morphometry, lung airways dimensions and respiratory parameters on particle deposition," *Journal of Thoracic Disease*, vol. 3, no. 3, pp. 156–170, 2011.

[18] K. H. Cheng, Y. S. Cheng, H. C. Yeh, and D. L. Swift, "Measurements of airway dimensions and calculation of mass transfer characteristics of the human oral passage," *Journal of Biomechanical Engineering-Transactions of the Asme*, vol. 119, no. 4, pp. 476–482, 1997.

[19] Y. Liu, M. R. Johnson, E. A. Matida, S. Kherani, and J. Marsan, "Creation of a standardized geometry of the human nasal cavity," *Journal of Applied Physiology*, vol. 106, no. 3, pp. 784–795, 2009.

[20] I. Amirav, A. A. T. Borojeni, A. Halamish, M. T. Newhouse, and L. Golshahi, "Nasal versus oral aerosol delivery to the "lungs" in infants and toddlers," *Pediatric Pulmonology*, vol. 50, no. 3, pp. 276–283, 2015.

[21] N. B. Carrigy, C. A. Ruzycki, L. Golshahi, and W. H. Finlay, "Pediatric in vitro and in silico models of deposition via oral and nasal inhalation," *Journal of Aerosol Medicine and Pulmonary Drug Delivery*, vol. 27, no. 3, pp. 149–169, 2014.

[22] P. G. Dalal, D. Murray, A. H. Messner, A. Feng, J. McAllister, and D. Molter, "Pediatric laryngeal dimensions: An age-based analysis," *Anesthesia and Analgesia*, vol. 108, no. 5, pp. 1475–1479, 2009.

[23] M. H. Dave, M. Kemper, A. R. Schmidt, C. P. Both, and M. Weiss, "Pediatric airway dimensions-a summary and presentation of existing data," *Pediatric Anesthesia*, vol. 29, no. 8, pp. 782–789, 2019.

[24] L. Golshahi, M. L. Noga, and W. H. Finlay, "Deposition of inhaled micrometer-sized particles in oropharyngeal airway replicas of children at constant flow rates," *Journal of Aerosol Science*, vol. 49, pp. 21–31, 2012.

[25] L. Golshahi, M. L. Noga, R. B. Thompson, and W. H. Finlay, "In vitro deposition measurement of inhaled micrometer-sized particles in extrathoracic airways of children and adolescents during nose breathing," *Journal of Aerosol Science*, vol. 42, no. 7, pp. 474–488, 2011.

[26] C. A. Ruzycki, L. Golshahi, R. Vehring, and W. H. Finlay, "Comparison of in vitro deposition of pharmaceutical aerosols in an idealized child throat with in vivo deposition in the upper respiratory tract of children," *Pharmaceutical Research*, vol. 31, no. 6, pp. 1525–1535, 2014.

[27] J. X. Xi, X. H. Si, J. W. Kim, and A. Berlinski, "Simulation of airflow and aerosol deposition in the nasal cavity of a 5-year-old child," *Journal of Aerosol Science*, vol. 42, no. 3, pp. 156–173, 2011.

[28] Y. Zhou, M. D. Guo, J. X. Xi, H. Irshad, and Y. S. Cheng, "Nasal deposition in infants and children," *Journal of Aerosol Medicine and Pulmonary Drug Delivery*, vol. 27, no. 2, pp. 110–116, 2014.

[29] N. T. Griscom and M. E. B. Wohl, "Dimensions of the growing trachea related to age and gender," *American Journal of Roentgenology*, vol. 146, no. 2, pp. 233–237, 1986.

[30] Y. Feng, J. N. Zhao, C. Kleinstreuer, Q. S. Wang, J. Wang, D. H. Wu, and J. Lin, "An in silico inter-subject variability study of extra-thoracic morphology effects on inhaled particle transport and deposition," *Journal of Aerosol Science*, vol. 123, pp. 185–207, 2018.

[31] J. Elcner, F. Lizal, J. Jedelsky, M. Jicha, and M. Chovancova, "Numerical investigation of inspiratory airflow in a realistic model of the human tracheobronchial airways and a comparison with experimental results," *Biomechanics and Modeling in Mechanobiology*, vol. 15, no. 2, pp. 447–469, 2016.

[32] J. Jedelsky, F. Lizal, and M. Jicha, "Characteristics of turbulent particle transport in human airways under steady and cyclic flows," *International Journal of Heat and Fluid Flow*, vol. 35, pp. 84–92, 2012.

[33] A. Farkas, F. Lizal, J. Jedelsky, J. Elcner, J. Karas, M. Belka, O. Misik, and M. Jicha, "The role of the combined use of experimental and computational methods in revealing the differences between the micron-size particle deposition patterns in healthy and asthmatic subjects," *Journal of Aerosol Science*, vol. 147, p. 105582, 2020.

[34] M. Nordlund, M. Belka, A. K. Kuczaj, F. Lizal, J. Jedelsky, J. Elcner, M. Jicha, Y. Sauser, S. Le Bouhellec, S. Cosandey, S. Majeed, G. Vuillaume, M. C. Peitsch, and J. Hoeng, "Multicomponent aerosol particle deposition in a realistic cast of the human upper respiratory tract," *Inhal Toxicol*, vol. 29, no. 3, pp. 113–125, 2017.

[35] J. Elcner, F. Lizal, J. Jedelsky, J. Tuhovcak, and M. Jicha, "Laminar-turbulent transition in a constricted tube: Comparison of reynolds-averaged navier-stokes turbulence models and large eddy simulation with experiments," *Advances in Mechanical Engineering*, vol. 11, no. 5, p. 1687814019852261, 2019.

[36] A. Farkas, F. Lizal, J. Jedelsky, J. Elcner, A. Horvath, and M. Jicha, "Simulation of airway deposition of an aerosol drug in copd patients," *Pharmaceutics*, vol. 11, no. 4, 2019.

[37] E. M. A. Frederix, A. K. Kuczaj, M. Nordlund, M. Belka, F. Lizal, J. Jedelský, J. Elcner, M. Jicha, and B. J. Geurts, "Simulation of size-dependent aerosol deposition in a realistic model of the upper human airways," *Journal of Aerosol Science*, vol. 115, no. Supplement C, pp. 29–45, 2018.

[38] P. G. Koullapis, L. Nicolaou, and S. C. Kassinos, "In silico assessment of mouth-throat effects on regional deposition in the upper tracheobronchial airways," *Journal of Aerosol Science*, vol. 117, pp. 164–188, 2018.

[39] A. Farkas, F. Lizal, J. Elcner, J. Jedelsky, and M. Jicha, "Numerical simulation of fibre deposition in oral and large bronchial airways in comparison with experiments," *Journal of Aerosol Science*, vol. 136, pp. 1–14, 2019.

[40] T. Janke, P. Koullapis, S. C. Kassinos, and K. Bauer, "Piv measurements of the siminhale benchmark case," *European Journal of Pharmaceutical Sciences*, vol. 133, pp. 183–189, 2019.

[41] M. Sommerfeld, O. L. Sgrott, M. A. Taborda, P. Koullapis, K. Bauer, and S. Kassinos, "Analysis of flow field and turbulence predictions in a lung model applying rans and implications for particle deposition," *European Journal of Pharmaceutical Sciences*, vol. 166, 2021.

[42] M. Belka, F. Lizal, J. Jedelsky, P. Starha, H. Druckmullerova, P. K. Hopke, and M. Jicha, "Application of image analysis method to detection and counting of glass fibers from filter samples," *Aerosol Science and Technology*, vol. 50, no. 4, pp. 353–362, 2016.

Variations of Flow Patterns in the Upper Bronchial Tree During the Breathing Cycle

K. Bauer[1], R. Schwarze[1] and T. Janke[2]

[1] *Institute of Mechanics and Fluid Dynamics, TU Bergakademie Freiberg, Germany*
[2] *LaVision GmbH, Goettingen, Germany*

Abstract

Velocity distributions in the human bronchial tree strongly influence particle transport and deposition behavior. Nevertheless, there is still a lack of systematic analysis of the oscillatory flow characteristics in the human airways. Thus, a realistic model of the human bronchial tree featuring the mouth throat region as well the bifurcating branches down to the 7th generation has been made from transparent silicone. By refractive index matching the oscillating flow inside the model geometry is visualized using Particle Image Velocimetry (PIV). Breathing parameters are varied from very low breathing activity up to breathing under heavy exercise. The results show that lower breathing velocities only lead to quantitative differences between flow patterns during inspiration and expiration. In contrast, at high breathing rates a remarkable qualitative change of the velocity profiles is observed during the expiration phase while the inspiration phase remains largely unaffected by Reynolds number variations.

1 Introduction

Fundamental knowledge about flow characteristics in the human airways is crucial for the application of appropriate mechanical ventilation strategies as well as for efficient drug delivery within the lungs. Despite an increasing number of sophisticated flow investigations in the human bronchial tree, numerically as well as experimentally, systematic investigations aimed at understanding the flow physics in bifurcating airways, especially for higher Re, are rare and open questions remain.

Banko et al.[1] investigated the three-dimensional, constant inspiratory flow at a realistic model of the upper bronchial tree for a typical breathing rate by means of Magnetic Resonance Velocimetry (MRV). At least for their patient specific model, at which steady inhalation was applied, information about regional flow distortion and secondary flow strength could be given. The measurement technique of MRV was also carried out for investigating the inspiratory flow at a planar double bifurcation model for a large range of Reynolds numbers of Re = 100 - 5000 [2]. They could show that the secondary vortex intensity increases up to Re = 2000 and then decreases for larger Re. In 2018, Jalal et al. [3] extended their double bifurcation study by an oscillating flow at Re = 2000 and varying Womersley number Wo. At least for their parameter range they found stronger secondary flows for higher Wo during inhalation and weaker secondary flow during exhalation. A comparison of patient specific, realistic models with idealized, symmetric airways revealed that the lateral dispersion in realistic models exceeds those found in the idealized models [4]. The authors furthermore found that differences between inhalation and exhalation are much larger than previously observed in idealized models. It could be shown that secondary flows in realistic airways are stronger during exhalation as compared to inhalation. This hence leads to weaker axial dispersion during exhalation. Moreover, secondary flows in realistic airways propagate deep in the bronchial tree [4].

An increase of the Womersley number by applying High Frequency Oscillatory Ventilation (HFOV) causes significant regions of flow reversal during the inhalation-exhalation [5, 4]. A mass transport mechanism which has been frequently associated with HFOV is steady streaming by which asymmetric velocity patterns in opposite flow direction cause a net mass transport [6, 7]. However, newer studies have shown that their contribution to mass transport though not negligible is by far not dominating compared to advective flow [8, 4]. Bauer et al.[8] have moreover shown that the strength of steady streaming is only influenced by the Reynolds number and not by the Womersley number. However, it should also be noted that for this study, the tidal volume has been varied to increase the Reynolds number while the frequency was kept constant. Thus, in a subsequent study, the Reynolds number has been kept constant by likewise increasing the tidal volume and reducing the frequency [9]. It was shown that net convective transport scales linearly with the applied tidal volume - at constant Re. Recently, Jacob et al. [10] carried out DNS (direct numerical simulation) studies at a single bifurcation model and found that recirculating flux, which they relate to steady streaming, accounts for 3-5% of the peak flux (maximum flow rate). Their Reynolds number variations moreover revealed conditional turbulent bursts when the flow velocity exceeds a certain value. These turbulent events occur downstream the bifurcation. That means during inhalation, this conditional turbulence was observed in the daughter branches whereas it was observed in the mother branch during the exhalation. However, it has to be noted that the events only occur for a very large Reynolds number of $Re = 9600$ in the mother branch. Typically, such large Reynolds number are not achieved during natural breathing, only during very heavy exercise breathing.

In any case, considering aerosol transport and deposition in the human lungs, numerical studies emphasize the importance of correct treatment of turbulence modelling and thus the high influence of the Reynolds number on particle transport and deposition [11, 12, 13]. Nevertheless, the detailed changes of flow patterns in realistic lung model during Reynolds number variations have to the best of our knowledge not been reported, yet. While steady flow conditions have been presented in Janke et al. [12], we will show the influence of increasing Reynolds number during the complete flow cycle on velocity distribution patterns for realistic, oscillatory flow conditions. Therefore, we employ PIV measurements at a realistic,

patient specific upper bronchial tree model (the SimInhale Benchmark Case) model for varying oscillating inflow conditions. In particular, we will show low, normal and exercise breathing conditions and compare our results to the findings of steady inhalation measurements.

1.1 Methods

The airway geometry represents the SimInhale Benchmark case [12, 11] which includes the upper airways with mouth/throat passage and bifurcates down to the 7th generation. The geometry is included in Figure (1) a) and b). For more information on model specifications see Lizal et al. [14]. This geometry has been 3D printed

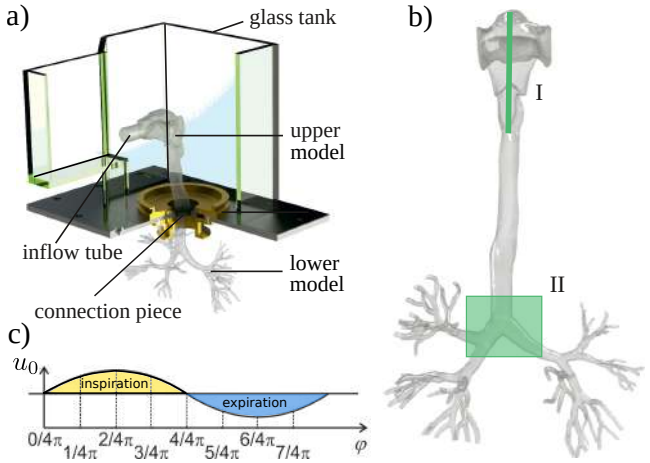

Figure 1: Lung geometry and velocity profiles at selected phase angles for low (Re = 1100) and normal breathing (Re = 4400) conditions.

from ABS (Acrylonitrile Butadiene Styrene). In a subsequent step an addition-curing transparent silicone rubber (ELASTOSIL®RT 601 A/B) was poured around the lung model. After curing of the silicone, the model core has been dissolved in acetone and a transparent silicone block with the hollow lung geometry inside was received. Due to the large dimensions of the model geometry, the silicone model consists of two silicone blocks; one which features the upper airways and a second part featuring the bronchial tree. Both parts are seamlessly connected in order to ensure smooth walls without unphysiologic steps.

The lung model was placed in a glass tank which is filled with a mixture of water and glycerin (mass ratio 42:58) in order to match the refractive index of the silicone. The upper part of the glass tank which shows the position of the lung model is presented in Figure (1) a). The mouth inlet and distal outlets of the model are open to the surrounding liquid. A linear motor generates an oscillatory motion of the liquid through the model which mimics the appropriate breathing patterns. Flow similarity with breathing in air is maintained by considering Reynolds and Womersley similarity. The Reynolds number is based here on the tidal volume V and the breathing frequency f and represents peak flow conditions with

$$Re = \frac{4\ V\ f}{D\ \nu}. \tag{1}$$

The characteristic length is the diameter of the trachea with $D = 16.3mm$. The kinematic viscosity of the water-glycerin mixture is $\nu = 8.4 \cdot 10^{-6}\ m^2/s$, the density is $\rho = 1150\ kg/m^3$. The Womersley number is defined as

$$Wo = \frac{D}{2}\sqrt{\frac{2\ \pi\ f}{\nu}}. \tag{2}$$

The unsteady flow was measured phase averaged by planar PIV measurements. Therefore, the flow is seeded with neutrally buoyant tracer particles (Polyamid, Vestosint, $d = 50\ \mu m$, $\rho = 1150\ kg/m^3$). The measurement planes were defined by a Nd:YAG Laser (Minilite) in the symmetry plane of the upper airways (I) as well as the center of the main bifurcation (II). The selected planes are shown in Figure (1) b). A total of 688 double images for each phase position were recorded by a PCO.1600 CCD camera. A minimum number of 8 phase position was used for all flow variations as shown in Figure (1) c). For the most relevant normal breathing condition with Re = 2200, 64 phase positions, equally distributed within the breathing cycle, were employed.

The recorded images were cross correlated by the software DaVis 8.4 from LaVision. The final window size was 16 × 16 px including 50 % overlap which corresponds to a spatial resolution of 0.5 × 0.5 mm^2. Three different measurement settings were employed here with constant tidal volume of 500 ml while the breathing frequency was varied, thus leading to a change in both, Re and Wo. Here, a low breathing situation (Re = 1100, Wo = 1.9), normal breathing (Re = 2200, Wo = 2.7) and breathing under exercise conditions (Re = 4400, Wo = 3.8) are compared.

2 Results and discussion

Velocity patterns

We begin with the analysis of the mean velocity patterns in the main bifurcation. Figure (2) presents the color coded distribution of the normalized velocity magnitude summarized for all Reynolds numbers and 8 phase angles during the breathing cycle. Note that we refer here only to a change in Re since Janke et al. [15] have shown that a change in Wo in the same range as applied here has only neglectable influence on the flow. We start with the

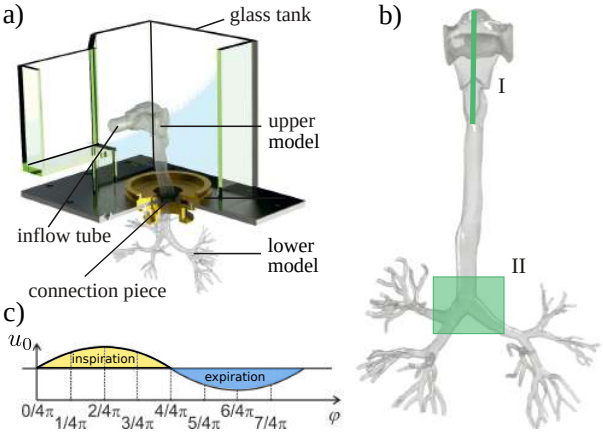

Figure 2: Normalized mean velocity magnitude for Re = 1100 - 4400 for 8 selected phase angles during the breathing cycle. Angles from $\varphi = 1/4\pi - 3/4\pi$ mark the inspiration phase, $4/4\pi$ the transition from inspiration to expiration, $\varphi = 5/4\pi - 7/4\pi$ denotes the expiration, $8/4\pi$ transition from expiration to inspiration

accelerating inspiration ($\varphi = 1/4\pi$). Increasing Re from laminar to fully the turbulent range only causes mild attenuation of the velocity profile skewness induced by turbulent fluctuations. Nevertheless, as reported by Jalal et al. [2] for a simplified double bifurcation model, this turbulent diffusion already causes decreased secondary flow intensity. In a later study from 2020, Jalal et al. [4] stated for a patient specific model that secondary

intensity does, in contrast to their previous study, increase within the first 2 generations by increasing Re. Thus, we assume here that secondary intensity does obviously not cause this homogenization. At peak inspiration ($\varphi = 2/4\pi$), flow patterns are even more similar for all Reynolds numbers and are also in very good agreement with steady flow patterns [12]. A similar trend can be observed for the deceleration phase ($\varphi = 3/4\pi$). The strongly skewed velocity profile and characteristic separation region in the left main branch exhibit even the same extension throughout the inspiration phase and for all different Reynolds numbers. Hence, the inspirational phase is obviously not influenced by increasing Reynolds numbers. This is in agreement with Jalal et al. [4] who stated that the distortion of velocity profiles is not different for low and high Reynolds number, i.e. the mean topology is not affected by the transition to turbulence.

During the transitional phases ($\varphi = 4/4\pi$ as well as $8/4\pi$) counter current flow as well as recirculations are enhanced, actually due to increased Womersley number as already described in Bauer et al. [9]. However, due to the generally low velocities during these phases, they do not contribute to axial dispersion but rather to radial cross exchange which is then increased as Womersley and thus Reynolds number increase.

Considering the expirational phases reveals a completely different behavior. Already in the accelerating expiration phase ($\varphi = 5/4\pi$) the flow velocity in the right main bronchus resembles a rather blunt shape for Re = 4400 while for lower Re it is subject to higher distortions with clear zones of high and low velocity. In the left main branch a separation region develops again for lower Re in the laminar range. For the turbulent case (Re = 4400) the separation region does not occur anymore. Although Jalal et al. [4] reported that radial dispersion is enhanced during exhalation, the homogenisation at Re = 4400 cannot be explained by this enhancement since it does not occur for lower Re. Thus, turbulent fluctuations are again assumed to cause this less distorted velocity profile. At peak expiration ($\varphi = 6/4\pi$), the separation zone in the left main branch is already strongly reduced for Re = 2200 and completely vanishes for Re = 4400. Free shear zones in the branch centers do not occur anymore for the fully turbulent case. This proofs the strong Reynolds dependency of the velocity patterns. It can hence be assumed that as a certain threshold has been exceeded, a qualitative change occurs in the velocity distribution. But, remarkably only during expiration. This qualitative pattern change was also identified by Janke et al. [15] who could visualize flow path lines by Particle Tracking Velocimetry (PTV) in a generic 3D lung model. By variation of Re from 250 - 2000, a displacement of helical flow structures during the expiration phase could be observed as the Reynolds number exceeded a certain value. Yet, the mechanisms which trigger this new formation remain still unclear. The deceleration phase during expiration ($\varphi = 7/4\pi$) resembles again the patterns from the acceleration phase for Re = 1100. For larger Re, the large separation zone in the left main branch is already reduced compared to the acceleration. Hence, the destabilizing deceleration already causes a change of the velocity profile and hence vortical structures. Consequently, as the flow during inspiration remains widely unaffected by the Reynolds number variation, particle transport and deposition will not change during this part of the breathing cycle. This is in agreement with Amili et al. [16] who have also shown that particle distribution does not change proportional to the flow rate. Particle distribution rather depends on their initial position in the airways and does not need to be symmetric even when the flow is symmetric. However, it has to be noted here that they considered only steady inhalation at a symmetric planar bifurcation model. Thus, statements about oscillatory transport, especially during expiration could not be made.

For more detailed analysis of the velocity variation within one breathing cycle, the velocities for the most relevant Reynolds number of Re = 2200, representing normal breathing, have been measured at 64 phase angles. We present the phase averaged velocity magnitude at a cross section of the left main branch. The corresponding profile line is marked in Figure (2).

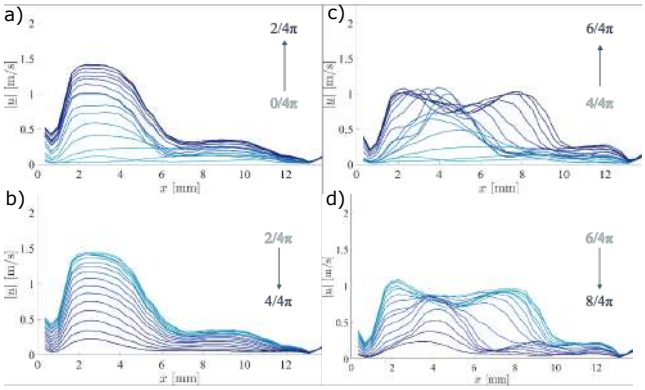

Figure 3: Phase averaged velocity profiles measured at 64 phase angle for Re = 2200. For the sake of the clarity, profiles are separated in four groups of phases: a) beginning inspiration to peak inspiration, b) peak inspiration to end of inspiration, c) beginning expiration to peak expiration, d) peak expiration to end of expiration.

During inspiration (Figure (3) a), b)), the velocity profiles only change in amplitude in the high speed region near the outer branch bend (inner bifurcation wall) and resemble an almost symmetric shape in time between acceleration and deceleration phase. A completely different distribution occurs, as expected, during expiration. At the beginning expiration (Figure (3) c), $\varphi > 4/4\pi$), the velocity profile is still flat and starts to increase in the branch center. With increasing expiration velocity, the velocity maximum is gradually shifted towards the outer bend radius ($x = 0$) due to increasing centrifugal forces. Towards peak exhalation, a second local maximum develops closer to the inner bend radius. The second maximum is assumed to be caused by additionally emerging vortex structures which do not occur for lower Reynolds numbers. During the decelerating expiration (Figure (3) d)) velocity patterns change in reverse order. First, the second peak near the inner branch radius decreases. Then, the maximum at the outer branch bend radius is shifted inwards. Nevertheless, the patterns of acceleration are never matched again.

To summarize and conclude the findings for the velocity patterns, we have shown that expiratory flow patterns vary strongly when the Reynolds number is increased. Hence, it can be deduced that the transport of aerosols out of the airways is subject to strong variations based on Reynolds number variations, too.

Fluctuations

We furthermore consider variations of the turbulent kinetic energy (tke) for increasing Reynolds number and during the breathing cycle. Since the planar PIV measurements only provide two components of the velocity

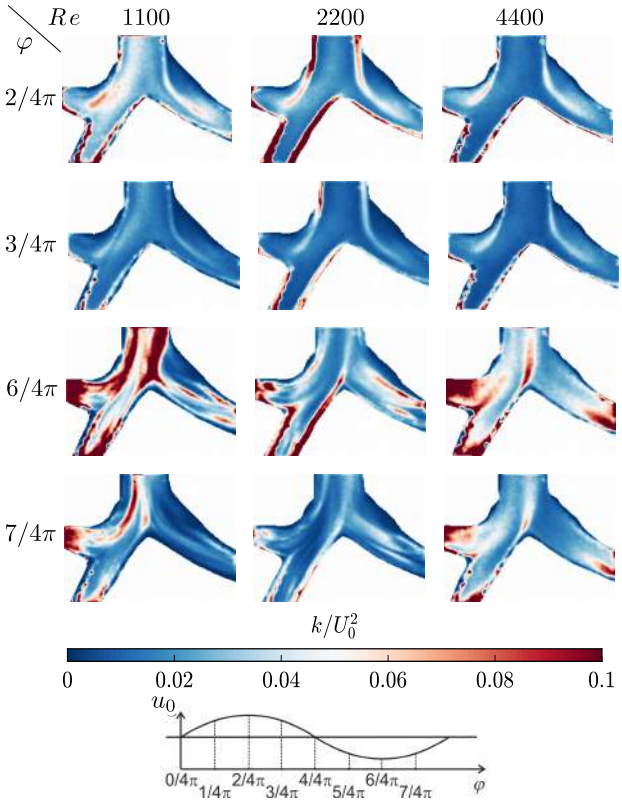

Figure 4: Turbulent kinetic energy k normalized with the bulk velocity U_0^2 for low, transitional and turbulent Reynolds numbers at distinctive phase angles.

vector, the total turbulent kinetic energy is here estimated by

$$k = 3/4 \cdot (\overline{u\prime u\prime} + \overline{v\prime v\prime}), \tag{3}$$

under the assumption of local isotropy, where the unresolved third component contributes with $1/2 \cdot (\overline{u\prime u\prime} + \overline{v\prime v\prime})$ to the total value [17].

Figure (4) gives an overview of the normalized tke k/u_0^2 for all Reynolds numbers and the most characteristic phase angles of peak inspiration ($\varphi = 2/4\pi$) and expiration ($\varphi = 6/4\pi$) as well as both deceleration phases ($\varphi = 3/4\pi$ and $\varphi = 7/4\pi$). It should be noted that for Re = 1100, actually no turbulent conditions can be expected and hence no tke. Nevertheless, already for this Reynolds number strong fluctuating components can be observed. By normalizing the tke, their contribution to the mean flow can be well approximated. It is apparent, that for the peak flow rates at Re = 1100 this normalized tke even exceeds the values for higher Reynolds numbers, especially in the trachea at peak expiration. In general, the relative tke is highest in regions of higher shear gradients, causing instabilities. Moreover, the tke reaches higher values in the expiration phases than during inspiration. Although decelerating flows are typically characterized by higher instabilities and earlier transition to turbulence, this does obviously not apply for the decelerating inspiration ($\varphi = 3/4\pi$), which shows the lowest tke and similar values for all Reynolds numbers.

In addition to the tke, we consider the averaged velocities and their standards deviations again at the profile line in the left main branch (compare Figure (2)). To better present the variations during the cycle, the already phase average velocity magnitudes along this profile line are averaged again in space. We furthermore added the mean standard deviation across the profile line represented by error bars. Both values are summarized in Figure (5) for the complete cycle and all investigated Reynolds numbers. Note that all values are positive as a velocity magnitude is presented. For Re = 1000, as well as for Re = 4400 only 8 phase angles have been measured and for Re = 2200 we can present the development for 64 phase angles. At Re = 1100 inspiration and expiration

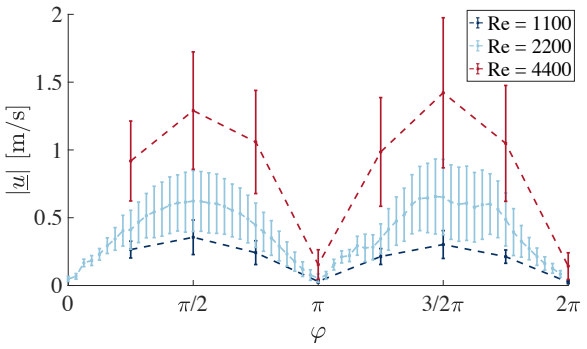

Figure 5: Velocity magnitudes, averaged along the given profile line in the left main branch, for 8 phases angles at Re = 1100 and Re = 4400 and 64 phase angles at Re = 2200 (dashed lines), error bars denoting the standard deviations, which are based on the fluctuations, are added for each phase angle.

resemble a similar and symmetric sinusoidal behavior. Standard deviations scale with the velocities and reach already for the low Reynolds number about 50% of the mean velocities. At Re = 2200 the inspiration resembles again a smooth sinusoidal velocity variation during the complete half cycle. Standard deviations suggest an almost linear increase and decrease reaching again about 50% of the corresponding mean velocities. During expiration the mean velocity curve is not as smooth anymore as during inspiration. Standard deviations still scale linearly with the mean velocities but slightly exceed the value from inspirations. For the largest Reynolds number of Re = 4400 the trend is continuing. The expiration is again subject to stronger standard deviations, i.e. also fluctuations. The lower resolution in time thus does not allow to evaluate the curve of the mean velocity in more detail. Hence, such curvy shape as shown for Re = 2200 cannot be resolved for Re = 4400.

3 Conclusions

Oscillatory flow patterns have been compared here for three different breathing scenarios - low, normal and heavy exercise breathing. In contrast to many previous studies that considered only inhalation, a strong variation of flow patterns during expiration has been observed here. During inspiration, velocity patterns remain qualitatively similar, with velocity magnitudes that are scaled as the flow accelerates to peak flow and back, a behavior that remains true even at higher Reynolds numbers. However, a completely different behavior is observed during expiration where flow reorganization already emerges at transitional numbers and becomes further pronounced at higher Reynolds numbers. A comparison to a previous, different 3D model has proven a similar behavior. Thus, this effect can assumed to be universal for different lung geometries and will have a strong impact on flow distribution and thus particle transport during expiration. As particle deposition is typically only investigated for steady inhalation, including the expiration should move more into focus. Nevertheless, further 3D measurements are required to investigate the spatial development of helical structures, especially with regards to the secondary Dean structures in order to deduce transport pathways in more detail.

Acknowledgments

The authors gratefully acknowledge financial support of this project by the Deutsche Forschungsgemeinschaft DFG (grant No. BA 4995-2/3). We furthermore thank Dr. František Lizal, Brno Institute of Technology, for providing the lung geometry within the framework of SimInhale COST Action MP1404.

References

[1] A. J. Banko, F. Coletti, D. Schiavazzi, C. J. Elkins, and J. K. Eaton, "Three-dimensional inspiratory flow in the upper and central human airways," *Experiments in Fluids*, vol. 56, no. 6, pp. 1–12, 2015.

[2] S. Jalal, A. Nemes, T. V. de Moortele, S. Schmitter, and F. Coletti, "Three-dimensional inspiratory flow in a double bifurcation airway model," *Experiments in Fluids*, vol. 57:148, p. 11pp., 2016.

[3] S. Jalal, T. V. de Moortele, A. Nemes, O. Amili, and F. Coletti, "Three-dimensional steady and oscillatory flow in a double bifurcation airway model," *Physical Review E*, vol. 103101, pp. 1–23, 2018.

[4] S. Jalal, T. Van De Moortele, O. Amili, and F. Coletti, "Steady and oscillatory flow in the human bronchial tree," *Physical Review Fluids*, vol. 5, no. 6, 2020.

[5] K. Adler and C. Brücker, "Dynamic flow in a realistic model of the upper human lung airways," *Experiments in Fluids*, vol. 43, no. 2-3, pp. 411–423, 2007.

[6] F. R. Haselton and P. W. Scherer, "Flow Visualization Of Steady Streaming In Oscillatory Flow Through A Bifurcating Tube.," *Journal of Fluid Mechanics*, vol. 123, pp. 315–333, 1982.

[7] J. M. Drazen, R. D. Kamm, and A. S. Slutsky, "High-frequency ventilation," *Physiological Reviews*, vol. 64, no. 2, pp. 505–543, 1984.

[8] K. Bauer and C. Brücker, "The Influence of Airway Tree Geometry and Ventilation Frequency on Airflow Distribution," *Journal of Biomechanical Engineering*, vol. 137, no. August, pp. 1–10, 2015.

[9] K. Bauer, E. Nof, and J. Sznitman, "Revisiting high-frequency oscillatory ventilation in vitro and in silico in neonatal conductive airway," *Clinical Biomechanics*, 2019.

[10] C. Jacob, D. G. Tingay, and J. S. Leontini, "The impact of steady streaming and conditional turbulence on gas transport during high-frequency ventilation," *Theoretical and Computational Fluid Dynamics*, vol. 35, no. 2, pp. 265–291, 2021.

[11] P. Koullapis, S. C. Kassinos, J. Muela, C. Perez-Segarra, J. Rigola, O. Lehmkuhl, Y. Cui, M. Sommerfeld, J. Elcner, M. Jicha, I. Saveljic, N. Filipovic, F. Lizal, and L. Nicolaou, "Regional aerosol deposition in the human airways: The SimInhale benchmark case and a critical assessment of in silico methods," *European Journal of Pharmaceutical Sciences*, vol. 113, no. June 2017, pp. 77–94, 2018.

[12] T. Janke, P. Koullapis, S. C. Kassinos, and K. Bauer, "PIV measurements of the SimInhale benchmark case," *European Journal of Pharmaceutical Sciences*, vol. 133, no. February, pp. 183–189, 2019.

[13] M. Sommerfeld, O. L. Sgrott, M. A. Taborda, P. Koullapis, K. Bauer, and S. Kassinos, "Analysis of flow field and turbulence predictions in a lung model applying RANS and implications for particle deposition," *European Journal of Pharmaceutical Sciences*, vol. 166, no. March, p. 105959, 2021.

[14] F. Lizal, J. Elcner, P. K. Hopke, J. Jedelsky, and M. Jicha, "Development of a realistic human airway model," *Proceedings of the Institution of Mechanical Engineers, Part H: Journal of Engineering in Medicine*, vol. 226, no. 3, pp. 197–207, 2012.

[15] T. Janke, R. Schwarze, and K. Bauer, "Measuring three-dimensional flow structures in the conductive airways using 3D-PTV," *Experiments in Fluids*, vol. 58, no. 10, 2017.

[16] O. Amili, J. Golzarian, and F. Coletti, "In Vitro Study of Particle Transport in Successively Bifurcating Vessels," *Annals of Biomedical Engineering*, vol. 47, no. 11, pp. 2271–2283, 2019.

[17] J. Sheng, H. Meng, and R. Fox, "A large eddy PIV method for turbulence dissipation rate estimation," *Chemical Engineering Science*, vol. 55, pp. 4423–4434, 2000.

Turbulence

Introduction to Theory and Applications of Turbulent Flows

Frans T.M. Nieuwstadt, Bendiks J. Boersma, Jerry Westerweel

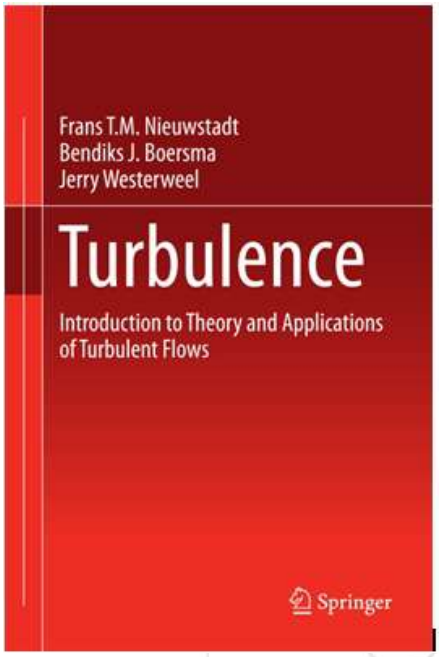

- **Winner of the 2017 Most Promising New Textbook Award from the Textbook & Academic Authors Association**
- Proven to be an excellent course-text over many years
- Combines theory with practical applications
- Avoids lengthy mathematical descriptions

This book provides a general introduction to the topic of turbulent flows. Apart from classical topics in turbulence, attention is also paid to modern topics. After studying this work, the reader will have the basic knowledge to follow current topics on turbulence in scientific literature. The theory is illustrated with a number of examples of applications, such as closure models, numerical simulations and turbulent diffusion, and experimental findings. The work also contains a number of illustrative exercises

DLES

Ercoftac Workshop
Direct & Large Eddy Simulation

DLES13 – Direct and Large Eddy Simulation

The Bi-Annual Workshop Series

26-29 October 2022

The bi-annual Workshop series on Direct and Large Eddy Simulation (DLES) which started in 1994 **focuses on modern techniques to simulate turbulent flows based on the partial or full resolution of the instantaneous turbulent flow structure**. With the growing capacities of modern computers, this approach has been gaining more and more interest over the years and will undoubtedly be further enhanced and applied. Techniques of hybrid modelling based on a combination of LES and RANS approaches also fall into this category and are covered as well.

The goal of the workshop is to establish a state-of-the-art of DNS, LES and related techniques for the computation and modelling of turbulent and transitional flows.

This gathering of specialists in the field will be a unique opportunity for discussions about recent advances in the prediction, understanding and control of turbulent flows in academic and industrial applications.

Visit: `https://dles.ercoftac.org/dles/`

ANIMATE - Advanced Numerical Modelling and Experimental Research on Turbulent and Transitional Flows with Applications to Chemical, Power, Automotive and Aeroengine Industries October 2019 - September 2021

A. Boguslawski, R. Gnatowska, W. Elsner, A. Tyliszczak, D. Asendrych
Department of Thermal Machinery, Częstochowa University of Technology

The Department of Thermal Machinery, Częstochowa University of Technology initiated in 2019 year an international co-operation within the ANIMATE project. The project is funded by THE POLISH NATIONAL AGENCY FOR ACADEMIC EXCHANGE - NAWA within an International Academic Partnerships Programme. The objective of the Programme is to develop durable solutions in the area of scientific, implementation and teaching process cooperation, pursued within the framework of international academic partnerships. The results of the project should provide a foundation for the development of a long-lasting cooperation of Universities or Research Centers forming a Partnership. Projects implemented under the Programme shall be in line with a long-term development policy of an Applicant and Partners. Turbulent and transitional flows in laboratory and industrial cases have been in a focus of research at Częstochowa University of Technology for more than 50 years. The main goal of the ANIMATE project is to strengthen an international cooperation with partners with whom the project coordinator cooperated already within European or bilateral projects. It is expected that partners' knowledge and experience in the field of turbulent flows will influence the level and scope of the research at Częstochowa University of Technology. The project is aimed also at an intensification of knowledge transfer to industrial partners and preparation of the research project of common academic-industrial institutions in a variety of industrial branches. The partners deliver complementary competences covering advanced modelling of turbulent flows, boundary layers, reactive and multiphase flows, high performance computing and experimental techniques. The goals of the project will be attained through an exchange of academic staff and PhD students concentrated around common research tasks with the use of computer codes, computer resources and experimental facilities of all the research groups involved in the project.

The cooperation is foreseen within the following tasks:

- Task no. 1 - Modelling and High Performance computing for turbulent reactive flows
- Task no. 2 - Development of new methods for multiphase flows investigations
- Task no. 3 Experimental and numerical studies of near wall flows

Six outstanding academic partners accepted the invitation to this project:

1. Institut National des Sciences Appliques de Rouen Normandie, rance, (Prof. Luc Vervish)
2. Centre Europen de Recherche et de Formation Avance en Calcul Scientifique-CERFACS), France, (Prof. Laurent Gicquel),
3. University of Twente (UT), The Netherlands, (Prof. Bernard Geurts),
4. University of Coimbra (UC), Portugal, (Prof. Maria G. Rasteiro, Prof. Pedro Faia)
5. Royal Institute of Technology (KTH), Sweden, (Prof. Philipp Schlatter)
6. Institute of Thermomechanics, Academy of Science of Czech Republic (IT AS CR), (Prof. Vaclav Uruba).

THIS PROJECT IS CO-FINANCED BY THE POLISH NATIONAL AGENCY FOR ACADEMIC EXCHANGE

ERCOFTAC Workshops and Summer Schools

ERCOFTAC Workshops, Conferences – 2021/22

Title	Location	Date	Coordinators	Organiser
13th International ERCOFTAC Symposium on Engineering Turbulence Modelling and Measurements	Rhodes, Greece	15-17/09/2021	Geurts, B.; Braza, M. Hickel, S.; Salvetti, M. V. Tomboulides, A	ERCOFTAC
Reconstruction methods for complex flows and porous media	Sheffield, UK	6/09/2021	Yi Li	SIG 42, 14
Topical Problems of Fluid Mechanics 2022	Prague, Czech Republic	16-18/02/2022	Bodnár, T.; Galusinski, C. Šimurda, D.	PC Czech Republic
17th UK Heat Transfer Conference (UKHTC-2021)	Manchester, UK	3-5/04/2022	Launder, B.; Wilson, D. Akhtar, N.	
TAI 1 - Turbulence And Interface 1	Lyon, France	18-20/05/2022	Gorokhovski, M.	PC Henri Bénard, SIG35
Environmental Fluid Mechanics: Turbulence and Fluid Mixing	Lille, France	23-24/05/2022	Nowakowski, A. F.	SIG 42, SIG 14, SIG 35
16thSPHERIC International Workshop	Piazza Roma, Italy	6-9/06/2022	Bilotta, G.	SIG 40
Progress in Flow Instability, Transition and Control	Cadiz, Spain	15-17/06/2022	De Pando, M. F; Schmid, P. Hanifi, A.	SIG 33
Modelling Fluid Flow – CMFF'22	Budapest, Hungary	30/08/2022-2/09/2022	Kristof, G.	PC Alpe Danube Adria
2nd International Workshop On Flow-Induced Blood Damage in Rotating Systems (BDW2022)	Rostock, Germany	1-2/09/2022	Wurm, F.-H. Torner, B.	SIG 37
European Drag Reduction and Flow Control Meeting – EDRFCM 2022	Paris, France	6-9/09/2022	Mortazavi, I Kwing-So, Ch.	ERCOFTAC, EU-CTFF
XXV Fluid Mechanics Conference (KKMP2022)	Rzeszów, Poland	7-9/09/2022	Kucaba-Piętal, A.	PC Poland
4th International Seminar on Non-Ideal Compressible Fluid Dynamics	London, UK	?/2022	White, M.	SIG 49
DLES13 - Direct and Large Eddy Simulation	Udine, Italy	26-29/10/2022		ERCOFTAC

ERCOFTAC Summer Schools, Courses – 2021/22

Title	Location	Date	Coordinators	Organiser
2nd International School on Hemophysics	Montpellier, France	5-9/10/2021	Nicoud, F. Abkarian, M. Mendez, S.	SIG 37
Course on Combustion towards Carbon-Neutral Combustion Systems	Eindhoven, The Netherlands	31/01/2022-4/02/2022	Bastiaans, R.J.M. Van Oijen, J. A	SIG 28

Flow, Turbulence and Combustion Journal

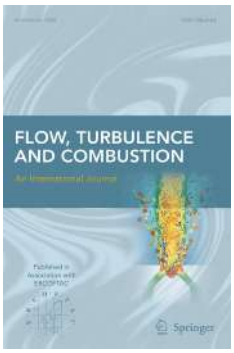

Recent Table Of Contents Of Flow Turbulence And Combustion

An International Journal Published By Springer
In Association With ERCOFTAC

Editor-In-Chief: M. A. Leschziner, A. M. Kempf
Editors: A. Dreizler, K. Fukagata, E. Gutmark, A. M. Kempf, S. Menon, W. Rodi, M. V. Salvetti, R. Sandberg, T. Schuller and B. van Wachem

Volume 107, Number 3, September 2021

High-speed turbulent gas jets: an LES investigation of Mach and Reynolds number effects on the velocity decay and spreading rate
F. Bonelli, A. Viggiano, V. Magi

Numerical Analysis of Side-loads Reduction in a Sub-scale Dual-bell Rocket Nozzle
M. Cimini, E. Martelli, M. Bernardini

Evolution of Turbulent Swirling Flow in a Small-Scale Cyclone with Increasing Flow Rate: A LES Study
D. Misiulia, G. Lidén, S. Antonyuk

An Optimization and Parametric Study of a Schlieren Motion Estimation Method
Q. Wang, X.H. Mei, Y. Wu, C.Y. Zhao

Flow Separation Control of Nacelle in Crosswind by Microsecond Pulsed Surface Dielectric Barrier Discharge Plasma Actuator
Y. Jia, H. Liang, Q. He, Z. Su, G. Song

Dimensionless Parameters to Identify Transition from Stratifi ed to Non-stratifi ed Flow Pattern in LiquidLiquid Horizontal Pipe Flow
S.A. Ahmed, B. John

Nonlinear Dynamics of a Swirl-Stabilized Combustor under Acoustic Excitations: Influence of the Excited Combustor Natural Mode Oscillations
Z. Rao, R. Li, B. Zhang, B. Wang, D. Zhao, M. Shahsavari

Large Eddy Simulation of an Ethanol Spray Flame with Secondary Droplet Breakup
S. Gallot-Lavallée, W.P. Jones, A.J. Marquis

Numerical Modeling of Flame Shedding and Extinction behind a Falling Thermoplastic Drip
C. Xiong, X. Huang

Analysis of Global and Local Hydrodynamic Instabilities on a High-Speed Jet Diffusion Flame via Time-Resolved 3D Measurements
R. Dong, Q. Lei, Y. Chi, E. Song, W. Fan

Unsteady Effects on NO x Measurements in Pulse Detonation Combustion
N. Hanraths, M.D. Bohon, C.O. Paschereit, N. Djordjevic

Further articles can be found at `www.springerlink.com`

Abstracted/Indexed in Science Citation Index, Science Citation Index Expanded (SciSearch), Journal Citation Reports/Science Edition, SCOPUS, INSPEC, Chemical Abstracts Service (CAS), Google Scholar, EBSCO, CSA, ProQuest, Academic OneFile, ASFA, Current Abstracts, Current Contents/Engineering, Computing and Technology, Earthquake Engineering Abstracts, EI Encompass, Ei Page One, EI-Compendex, EnCompassLit, Engineered Materials Abstracts, Gale, OCLC, PASCAL, SCImago, STMA-Z, Summon by Serial Solutions, VINITI - Russian Academy of Science.

Instructions for Authors for Flow Turbulence Combust are available at `http://www.springer.com/10494`.

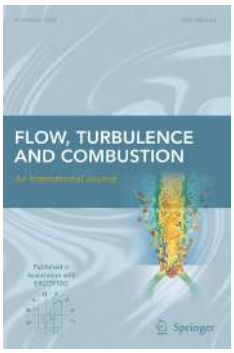

Recent Table Of Contents Of Flow Turbulence And Combustion
An International Journal Published By Springer
In Association With ERCOFTAC
Editor-In-Chief: M. A. Leschziner, A. M. Kempf
Editors: A. Dreizler, K. Fukagata, E. Gutmark, A. M. Kempf, S. Menon, W. Rodi, M. V. Salvetti, R. Sandberg, T. Schuller and B. van Wachem

Volume 107, Number 4, November 2021

Adapted Linear Forcing for Inlet Turbulent Fluctuations Generation and Application to a Conical Vortex Flow
R. Perrin

Large-Eddy Simulation of Bypass Transition on a Zero-Pressure-Gradient Flat Plate Using the Spectral-Element Dynamic Model
G. Lodato, N. Tonicello, B. Pinto

The Turbulent Flow over the BARC Rectangular Cylinder: A DNS Study
A. Chiarini, M. Quadrio

A Numerical Study of the Global Instability in Counter-Current Homogeneous Density Incompressible Round Jets
K. Wawrzak, A. Boguslawski, A. Tyliszczak

Energy Partitioning Control in the PITM Hybrid RANS/LES Method for the Simulation of Turbulent Flows
B. Chaouat, R. Schiestel

Study on the Spray Characteristics and Oscillation Mechanism of a Feedback-Free Internal Impinging Nozzle
Z. Wu, W. Zhao, Z. Hu, W. Xie, Y. Wang, L. Li

A Strategy to Couple Thickened Flame Model and Adaptive Mesh Refi nement for the LES of Turbulent Premixed Combustion
C. Mehl, S. Liu, O. Colin

The Utilisation of Reduced Kinetics by Local Self-Similarity Tabulation Approach in 3D Turbulent Reactive Flow Simulation with LES and TPDF
S. Guryuva, H. Bedir

Correction: The Utilisation of Reduced Kinetics by Local Self-Similarity Tabulation Approach in 3D Turbulent Reactive Flow Simulation with LES and TPDF
S. Guryuva, H. Bedir

Investigation of Oscillatory States Involving Acoustic Mode Shifts in a Turbulent Syngas Combustion using Non-stationary Time-series Analysis
N.A. Baraiya, V. Ramanan, N. Baladandayuthapani, C.S. Vegad, S.R. Chakravarthy

Flow, Turbulence and Combustion Journal

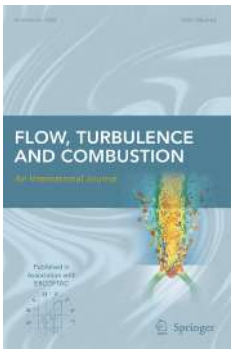

Recent Table Of Contents Of Flow Turbulence And Combustion

An International Journal Published By Springer
In Association With ERCOFTAC

Editor-In-Chief: M. A. Leschziner, A. M. Kempf
Editors: A. Dreizler, K. Fukagata, E. Gutmark, A. M. Kempf, S. Menon, W. Rodi, M. V. Salvetti, R. Sandberg, T. Schuller and B. van Wachem

Volume 108, Number 1, January 2022

Development and Validation of a New Formulation of Hybrid Temporal Large Eddy Simulation
V. Duffal, B. de Laage de Meux, R. Manceau

Wall-Resolved Large Eddy Simulations of the Transient Turbulent Fluid Mixing in a Closed System Replicating a Pressurized Thermal Shock
P.-E. Angeli

Analysis of High-order Explicit LES Dynamic Modeling Applied to Airfoil Flows
N. Tonicello, G. Lodato, L. Vervisch

Dissipation Scalings in the Turbulent Boundary Layer at Moderate Reθ
M. Obligado, C. Brun, J.H. Silvestrini, E.B.C. Schettini

On the Flow and Passive Noise Control of an Open Cavity at Re = 5000
R. Martin, M. Soria, I. Rodriguez, O. Lehmkuhl

A Priori Evaluation of the Laminar Flamelet Decomposition Model for Turbulent Premixed Flames using DNS Data
A.H. Mahdipour, M.M. Salehi

Effects of Body Forces on the Statistics of Flame Surface Density and Its Evolution in Statistically Planar Turbulent Premixed Flames
A.R. Varma, U. Ahmed, N. Chakraborty

Turbulence-Driven Blowout Instabilities of Premixed Bluff-Body Flames
A.J. Morales, T. Genova Jr., J. Reyes, I. Boxx, K.A. Ahmed

Effects of Stratifi cation and Preheat on Turbulent Flame Characteristics and Stabilization
K. Soufl as, P. Koutmos

Effect of Fuel Stratifi cation on OH and CH_2O PLIF Multiplication of Turbulent Hydrogen-Enriched Flames
S. Mohammadnejad, L. Saca, R. Heydarlaki, Q. An, P. Vena, S. Yun, P. Versailles, G. Bourque, S. Kheirkhah

Analysis of a Quasi-Two-Dimensional Flamelet Model on a Three-Feed Non-premixed Oxy-Combustion Burner
P. Yu, H. Watanabe, H. Pitsch, I. Yuri, H. Nishida, T. Kitagawa

Further articles can be found at `www.springerlink.com`

Abstracted/Indexed in Science Citation Index, Science Citation Index Expanded (SciSearch), Journal Citation Reports/Science Edition, SCOPUS, INSPEC, Chemical Abstracts Service (CAS), Google Scholar, EBSCO, CSA, ProQuest, Academic OneFile, ASFA, Current Abstracts, Current Contents/Engineering, Computing and Technology, Earthquake Engineering Abstracts, EI Encompass, Ei Page One, EI-Compendex, EnCompassLit, Engineered Materials Abstracts, Gale, OCLC, PASCAL, SCImago, STMA-Z, Summon by Serial Solutions, VINITI - Russian Academy of Science.

Instructions for Authors for Flow Turbulence Combust are available at `http://www.springer.com/10494`.

1. Large Eddy Simulation
Salvetti, M.V.
University of Pisa, Italy.
Tel: +39 050 221 7262
mv.salvetti@ing.unipi.it

4. Turbulence in Compressible Flows
Sesterhenn, J.
TU Berlin
Joern.Sesterhenn@TU-Berlin.de

5. Environmental Fluid Mechanics
Bomers, A.
University of Twente
a.bomers@utwente.nl
Cianferra, M.
University of Trieste
marta.cianferra@dia.units.it

10. Transition Modelling
Dick, E.
University of Ghent, Belgium
Tel: +32 926 433 01
erik.dick@ugent.be

12. Dispersed Turbulent Two Phase Flows
Sommerfeld, M.
University of Magdeburg, Germany
Tel: +49 345 552 3680
martin.sommerfeld@ovgu.de

14. Stably Stratified and Rotating Flows
Bodnar, T.
Czech Technical University in Prague,
Tel: +420 224 35 75 48
Tomas.Bodnar@fs.cvut.cz

15. Turbulence Modelling
Jakirlic, S.
Darmstadt University of Technology, Germany
Tel: +49 615 116 3554
s.jakirlic@sla.tu-darmstadt.de

20. Drag Reduction and Flow Control
Choi, K-S.
University of Nottingham, England
Tel: +44 115 951 3792
kwing-so.choi@nottingham.ac.uk

28. Reactive Flows
Roekaerts, D.
Delft University of Technology,
The Netherlands.
Tel: +31 152 782 470
D.J.E.M.Roekaerts@tudelft.nl

32. Particle Image Velocimetry
Scarano, F., Sciacchitano, A.
Delft University of Technology,
The Netherlands.
F.Scarano@tudelft.nl
A.Sciacchitano@tudelft.nl

33. Transition Mechanisms, Prediction and Control
Hanifi, A.
FOI, Sweden
Tel: +46 855 503 197
ardeshir.hanifi@foi.se

34. Design Optimisation
Giannakoglou, K.
NTUA, Greece
Tel: +30 210 772 1636
kgianna@central.ntua.gr

35. Multipoint Turbulence Structure and Modelling
Cambon, C.
ECL Ecully, France.
Tel: +33 472 186 161
claude.cambon@ec-lyon.fr

36. Swirling Flows
Braza, M.
IMFT, France
Tel: +33 (0) 561 285 839
braza@imft.fr

37. Bio-Fluid Mechanics
Nicoud, F.
Université de Montpellier, France
franck.nicoud@umontpellier.fr

39. Aeroacoustics
Bailly, C.
Ecole Centrale de Lyon, France
Tel: +33 472 186 014
christophe.bailly@ec-lyon.fr

40. Smoothed Particle Hydrodynamics
Vacondio, R.
University of Parma, Italy
enato.vacondio@unipr.it

41. Fluid Structure Interaction
Braza, M.
IMFT, France
Tel: +33 (0) 561 285 839
marianna.braza@imft.fr
Longatte, E.
EDF R&D, France

42. Synthetic Models in Turbulence
Nowakowski, A.
University of Sheffield, England
Tel: +44 114 222 7812
a.f.nowakowski@sheffield.ac.uk

43. Fibre Suspension Flows
Lundell, F.
The Royal Institute of Technology, Sweden
Tel: +46 87 906 875
fredrik@mech.kth.se

44. Multiscale-generated Turbulent Flows
Fortuné, V.
Universite de Poitiers, France

45. Uncertainty Quantification in Industrial Analysis and Design
Lucor, D.
d'Alembert Institute, France
Tel: +33 (0) 144 275 472
didier.lucor@upmc.fr

46. Oil, Gas and Petroleum
Sommerfeld, M.
Otto von Guericke-Universität Germany
martin.sommerfeld@ovgu.de
Khanna, S.
BP Global, USA

47. 3D Wakes
Morrison, J.F.
Imperial College, London
Tel: +44 (0) 20 7594 5067
j.morrison@imperial.ac.uk
Cadot, O.
ENSTA Paris Tech,
Université Paris-Saclay
Tel: +33 (0) 16 931 9756
cadot@ensta.fr

48. Respiratory Aerosols
Kassinos, S.
University of Cyprus
kassinos@ucy.ac.cy
Sznitman, J.
Biofluids Laboratory, Israel
sznitman@bm.technion.ac.il

49. Non-Ideal Comp. Fluid Dynamics
Guardone, A.
Politecnico di Milano, Italy
alberto.guardone@polimi.it
Pini, M.
Delft University of Technology,
The Netherlands
M.Pini@tudelft.nl

50. GeoAstro
Marino, R.
CNRS/École Centrale de Lyon, France
raffaele.marino@ec-lyon.fr

51. High-Pressure & Compressible Combustion
di Mare, F.
University Bochum, Germany
Francesca.dimare@rub.de

ERCOFTAC Pilot Centres

Alpe - Danube - Adria
Steiner, H.
Inst. Strömungslehre and
Wärmeübertragung
TU Graz, Austria
kristof@ara.bme.hu

Belgium
Hillewaert, K.
Bâtiment Eole,
6041 Gosselies,
Belgium.
Tel: +32 71 910 942
Fax: +32 495 385 030
koen.hillewaert@cenaero.be

Brasil
Rodriguez, O.
Department of Mechanical Engineering,
Sao Carlos School of Mechanical
Engineering,
Universidade de Sao Paulo,
Brasil.
oscarmhr@sc.usp.br

Czech Republic
Bodnar, T.
Institute of Thermomechanics AS CR,
5 Dolejskova,
CZ-18200 Praha 8,
Czech Republic.
Tel: +420 224 357 548
Fax: +420 224 920 677
bodnar@marian.fsik.cvut.cz

Iberia
Onate, E.
Universitat Politenica de Catalunya,
Valero, E.
Universidad Politécnica de Madrid,
Spain.
onate@cimne.upc.edu
eusebio.valero@upm.es

France South
Braza, M.
IMF Toulouse,
CNRS UMR - 5502,
Allée du Prof. Camille Soula 1,
F-31400 Toulouse Cedex, France.
Tel: +33 534 322 839
Fax: +33 534 322 992
Braza@imft.fr

France West
Hadjadj, A.
Tel: +33 232 959 794
hadjadj@coria.fr
CORIA, France
Lucor, D.
Tel: +33 (0)169 157 226
didier.lucor@limsi.fr
LIMSI-CNRS, France

Germany North
Sommerfeld, M.
University of Magdeburg,
Germany
Tel: +49 345 552 3680
martin.sommerfeld@ovgu.de

Germany South
Becker, S.
Universität Erlangen, IPAT
Cauerstr. 4
91058 Erlangen
Germany
Tel: +49 9131 85 29451
Fax: +49 9131 85 29449
sb@ipat.uni-erlangen.de

Greece
G. Skevis.
Centre for Research & Technology Hellas
(CERTH)Heroon Polytechniou 9
Greece
gskevis@certh.gr

Italy
Rispoli, F.
Tel: +39 064 458 5233
franco.rispoli@uniroma1.it
Borello, D
Tel: +39 064 458 5263
domenico.borello@uniroma1.it
Sapienza University of Rome,
Via Eudossiana, 18
00184 Roma, Italy

Netherlands
Van Heijst, G.J.
J.M. Burgerscentrum,
National Research School for Fluid
Mechanics, Mekelweg 2,
NL-2628 CD Delft, Netherlands.
Tel: +31 15 278 1176
Fax: +31 15 278 2979
g.j.f.vanheijst@tudelft.nl

Nordic
Wallin, S.
KTH, Dept. of Mechanics,
SE-100 44 Stockholm,
Sweden
Tel: +46 733 303 453
stefanw@mech.kth.se

Poland
Szumbarski J.
Warsaw University of Technology,
Inst. of Aero. & App. Mechanics,
ul. Nowowiejska 24,
PL-00665 Warsaw, Poland.
Tel: +48 22 234 7444
Fax: +48 22 622 0901
jasz@meil.pw.edu.pl

France - Henri Bénard
Gorokhovski, M.
École Centrale de Lyon &
LMFA UMR CNRS 5509,
France.
mikhael.gorokhovski@ec-lyon.fr

United Kingdom
Juniper, M.
Department of Engineering,
Trumpington Street,
Cambridge, CB2 1PZ
United Kingdom.
Tel: +44 (0) 1223 332 585
mpj1001@cam.ac.uk

ISSN: 2518-0991

Best Practice Guidelines for Computational Fluid Dynamics of Dispersed Multi-Phase Flows

Editors

Martin Sommerfeld, Berend van Wachem
&
René Oliemans

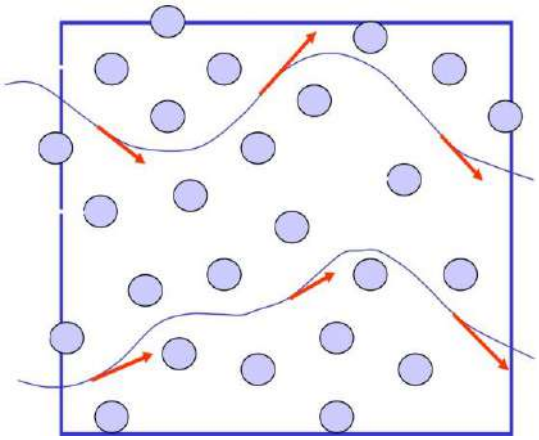

The simultaneous presence of several different phases in external or internal flows such as gas, liquid and solid is found in daily life, environment and numerous industrial processes. These types of flows are termed multiphase flows, which may exist in different forms depending on the phase distribution. Examples are gas-liquid transportation, crude oil recovery, circulating fluidized beds, sediment transport in rivers, pollutant transport in the atmosphere, cloud formation, fuel injection in engines, bubble column reactors and spray driers for food processing, to name only a few. As a result of the interaction between the different phases such flows are rather complicated and very difficult to describe theoretically. For the design and optimisation of such multiphase systems a detailed understanding of the interfacial transport phenomena is essential. For single-phase flows Computational Fluid Dynamics (CFD) has already a long history and it is nowadays standard in the development of air-planes and cars using different commercially available CFD-tools.

Due to the complex physics involved in multiphase flow the application of CFD in this area is rather young. These guidelines give a survey of the different methods being used for the numerical calculation of turbulent dispersed multiphase flows. The Best Practice Guideline (BPG) on Computational Dispersed Multiphase Flows is a follow-up of the previous ERCOFTAC BPG for Industrial CFD and should be used in combination with it. The potential users are researchers and engineers involved in projects requiring CFD of (wall-bounded) turbulent dispersed multiphase flows with bubbles, drops or particles.

Table of Contents

1. Introduction
2. Fundamentals
3. Forces acting on particles, droplets and bubbles
4. Computational multiphase fluid dynamics of dispersed flows
5. Specific phenomena and modelling approaches
6. Sources of errors
7. Industrial examples for multiphase flows
8. Checklist of '*Best Practice Advice*'
9. Suggestions for future developments

Copies of the Best Practice Guidelines can be acquired electronically from the ERCOFTAC website:

www.ercoftac.org

Or from:

ERCOFTAC (CADO)
PO Box 1212
Bushey, WD23 9HT
United Kingdom

Tel: +44 208 117 6170
Email: admin@cado-ercoftac.org

The price per copy (not including postage) is:

ERCOFTAC members	
First copy	*Free*
Subsequent copies	75 Euros
Students	75 Euros
Non-ERCOFTAC academics	140 Euros
Non-ERCOFTAC industrial	230 Euros
EU/Non EU postage fee	10/17 Euros